

**An-Najah National University  
Faculty of Graduate Studies**

**Influences of a Uniform External Magnetic Field on the  
Magnetic Properties of the Dipolar Anti-ferromagnetic  
Heisenberg System**

**By**

**Thaer " Mohammed Said" Mustafa Abu-Labdeh**

**Supervised by**

**Dr. Abdel-Rahman Mustafa Abu-Labdeh**

*This Thesis is Submitted in Partial Fulfillment of the Requirements for  
the Degree of Master of Science in Physics, Faculty of Graduate Studies,  
at AN-Najah National University, Nablus, Palestine.*

**2009**

**Influences of a Uniform External Magnetic Field on the Magnetic Properties of the Dipolar Anti-ferromagnetic Heisenberg System**

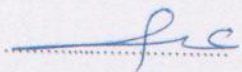
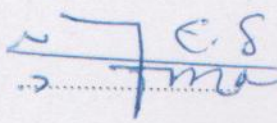
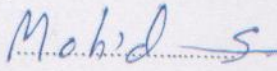
*To My family*

by  
**Thaer " Mohammed Said" Mustafa Abu-Labdeh**

*This Thesis was defended successfully on 10 / 9 / 2009 and approved by*

**Committee Members**

**Signature**

- |  |                     |  |
|--|---------------------|--|
| 1. Dr. Abdel-Rahman M. A. Labdeh<br>Assistant Professor of Physics | (Supervisor)        |  |
| 2. Prof. Dr. Imad A. Barghouthi<br>Professor of Physics            | (External Examiner) |  |
| 3. Dr. Mohammed S. Abu Jafar<br>Associate Professor of Physics     | (Internal Examiner) |  |

## **Dedication**

*To My family*

## Acknowledgements

I would like to express my gratitude and deepest appreciation to Dr. Abdel-Rahman Mustafa Abu-Labdeh for his guidance, encouragement and great efforts. I'd like to appreciate the efforts of the committee members represented by Prof. Dr. Imad A. Barghouthi (*Al-Quds University*) as an external examiner and Dr. Mohammed S. Abu-Jafar (*Dean of Graduate Studies, An-Najah National University*) as an internal examiner.

Also, I would like to thank the people at the Physics Department at An-Najah National University, who stand behind the Master's Program in physics. Special thanks to my friends Raead, Hany, Kamal and all my classmates in the program.

I gratefully acknowledge access to Computational Resources through Western Canada Research Grid (*WestGrid*) at university of Calgary and Shared Hierarchical Academic Research Computing Network (SHARCNET) at university of Western Ontario.

## إقرار

أنا الموقع أدناه مقدم الرسالة التي تحمل العنوان:

### **Influences of a Uniform External Magnetic Field on the Magnetic Properties of the Dipolar Anti-ferromagnetic Heisenberg System**

أقر بأن ما اشتملت عليه هذه الرسالة، إنما هي نتاج جهدي الخاص، باستثناء ما تمت الإشارة إليه حيثما ورد، وأن هذه الرسالة ككل، أو أي جزء منها لم يقدم من قبل لنيل أية درجة علمية أو بحث علمي أو بحثي لدى أية مؤسسة تعليمية أو بحثية أخرى.

### **Declaration**

The work provided in this thesis, unless otherwise referenced, is the researchers own work, and has not been submitted elsewhere for any other degree or qualification.

**Student's name:**

اسم الطالب:

**Signature:**

التوقيع:

**Date:**

التاريخ:

## Table of Contents

<b>Subject</b>	<b>page</b>
Dedication	<b>iii</b>
Acknowledgements	<b>iv</b>
Declaration	<b>v</b>
Table of Contents	<b>vi</b>
List of Tables	<b>vii</b>
List of Figures	<b>viii</b>
Abstract	<b>xiii</b>
1 Introduction	<b>1</b>
2 The Model in General Terms	<b>11</b>
3 Monte Carlo Simulations and Computational Details	<b>19</b>
3.1 Introduction	<b>20</b>
3.2 Importance Sampling, Detailed Balance	<b>21</b>
3.3 Metropolis Algorithm	<b>23</b>
3.4 Computational Aspects	<b>25</b>
4 Results and Discussion	<b>27</b>
4.1 Introduction	<b>28</b>
4.2 Finite Temperature Properties	<b>28</b>
4.3 The Magnetic Phase Diagram	<b>67</b>
5 Conclusions	<b>73</b>
References	<b>76</b>

**List of Tables**

<b>Tables</b>	<b>page</b>
<b>Table 4.1:</b> The locations of the transition points between planar antiferromagnetic phase and the perpendicular antiferromagnetic phase at $T/g = 2.5$ for $h/g = 10, 20$ and $27$ .	<b>33</b>
<b>Table 4.2:</b> The locations of the transition points between planar antiferromagnetic phase and the paramagnetic phase at $\kappa/g = -10$ for $h/g = 10, 20$ and $27$ .	<b>43</b>
<b>Table 4.3:</b> The locations of the transition points between perpendicular antiferromagnetic phase and the paramagnetic phase at $\kappa/g = 2$ for $h/g = 10, 20$ and $27$ .	<b>56</b>

## List of Figures

Figures	page
<b>Figure 4.1:</b> A plot of the total average energy $\langle E/g \rangle$ per spin as a function of increasing and decreasing the relative magnetic surface anisotropy parameter $\kappa/g$ at $T/g = 2.5$ for (a) $h/g = 10$ , (b) $h/g = 20$ and (c) $h/g = 27$	30
<b>Figure 4.2:</b> A plot of the total average energy $\langle E/g \rangle$ per spin as a function of the relative magnetic surface anisotropy parameter $\kappa/g$ at $T/g = 2.5$ with $h/g = 10, 20$ and $27$	31
<b>Figure 4.3:</b> The snapshots of spin configurations at $\kappa/g = -8 < \kappa_N/g$ with $T/g = 2.5$ for (a) $h/g = 10$ (b) $h/g = 20$ and (c) $h/g = 27$ .	32
<b>Figure 4.4:</b> The snapshots of spin configurations at $\kappa/g = 2 > \kappa_N/g$ with $T/g = 2.5$ for a) $h/g = 10$ (b) $h/g = 20$ and (c) $h/g = 27$ , where the symbol $\times$ shows spin down while symbol $\bullet$ shows spin up.	33
<b>Figure 4.5:</b> A plot of the average dipolar energy $\langle E_{dd}/g \rangle$ per spin as a function of increasing and decreasing the surface anisotropy $\kappa/g$ at $T/g = 2.5$ for (a) $h/g = 10$ , (b) $h/g = 20$ and (c) $h/g = 27$ .	35
<b>Figure 4.6:</b> A plot of the average anisotropy energy $\langle E_{\kappa}/g \rangle$ per spin as a function of increasing and decreasing the surface anisotropy $\kappa/g$ at $T/g = 2.5$ for (a) $h/g = 10$ , (b) $h/g = 20$ and (c) $h/g = 27$ .	36
<b>Figure 4.7:</b> A plot of the average exchange energy $\langle E_{ex}/g \rangle$ per spin as a function of increasing and decreasing the surface anisotropy $\kappa/g$ at $T/g = 2.5$ for (a) $h/g = 10$ , (b) $h/g = 20$ and (c) $h/g = 27$	37
<b>Figure 4.8:</b> A plot of the average Zeeman energy $\langle E_h/g \rangle$ per spin as a function of increasing and decreasing the surface anisotropy $\kappa/g$ at $T/g = 2.5$ for (a) $h/g = 10$ , (b) $h/g = 20$ and (c) $h/g = 27$ .	38
<b>Figure 4.9:</b> A plot of the average dipolar energy $\langle E_{dd}/g \rangle$ per spin as a function of the surface anisotropy $\kappa/g$ at $T/g = 2.5$ with $h/g = 10, 20$ and $27$ .	39

<b>Figures</b>	<b>page</b>
<b>Figure 4.10:</b> A plot of the average anisotropy energy $\langle E_{\kappa}/g \rangle$ per spin as a function of the surface anisotropy $\kappa/g$ at $T/g = 2.5$ with $h/g = 10, 20$ and $27$ .	<b>39</b>
<b>Figure 4.11:</b> A plot of the average exchange energy $\langle E_{ex}/g \rangle$ per spin as a function of the surface anisotropy $\kappa/g$ at $T/g = 2.5$ with $h/g = 10, 20$ and $27$ .	<b>40</b>
<b>Figure 4.12:</b> A plot of the average Zemann energy $\langle E_h/g \rangle$ per spin as a function of the surface anisotropy $\kappa/g$ at $T/g = 2.5$ with $h/g = 10, 20$ and $27$ .	<b>40</b>
<b>Figure 4.13:</b> A plot of the total average energy $\langle E/g \rangle$ per spin as a function of increasing and decreasing $T/g$ at $k/g = -10$ for (a) $h/g = 10$ , (b) $h/g = 20$ and (c) $h/g = 27$ .	<b>42</b>
<b>Figure 4.14:</b> A plot of the total average energy $\langle E/g \rangle$ per spin as a function of $T/g$ at $k/g = -10$ with $h/g = 10, 20$ and $27$ .	<b>43</b>
<b>Figure 4.15:</b> A plot of the average dipolar energy $\langle E_{dd}/g \rangle$ per spin as a function of heating and cooling the system at $k/g = -10$ for (a) $h/g = 10$ , (b) $h/g = 20$ and (c) $h/g = 27$ .	<b>45</b>
<b>Figure 4.16:</b> A plot of the average dipolar energy $\langle E_{dd}/g \rangle$ per spin for heating and cooling the system at $k/g = -10$ (a) $h/g = 10$ , (b) $h/g = 20$ and (c) $h/g = 27$ .	<b>46</b>
<b>Figure 4.17:</b> A plot of the average exchange energy $\langle E_{ex}/g \rangle$ per spin for heating and cooling the system at $k/g = -10$ (a) $h/g = 10$ , (b) $h/g = 20$ and (c) $h/g = 27$ .	<b>47</b>
<b>Figure 4.18:</b> A plot of the average Zemann energy $\langle E_h/g \rangle$ per spin for heating and cooling the system at $k/g = -10$ (a) $h/g = 10$ , (b) $h/g = 20$ and (c) $h/g = 27$ .	<b>48</b>
<b>Figure 4.19:</b> A plot of the average dipolar energy $\langle E_{dd}/g \rangle$ per spin as a function of temperature $T/g$ at $k/g = -10$ for $h/g = 10, 20$ and $27$ .	<b>49</b>
<b>Figure 4.20:</b> A plot of the average anisotropy energy $\langle E_{\kappa}/g \rangle$ per spin as a function of temperature $T/g$ at $k/g = -10$ with $h/g = 10, 20$ and $27$ .	<b>49</b>

<b>Figures</b>	<b>page</b>
<b>Figure 4.21:</b> A plot of the average exchange energy $\langle E_{\text{ex}}/g \rangle$ per spin as a function of temperature $T/g$ at $k/g = -10$ with $h/g = 10, 20$ and $27$ .	<b>50</b>
<b>Figure 4.22:</b> A plot of the average Zemann energy $\langle E_h/g \rangle$ per spin as a function of temperature $T/g$ at $k/g = -10$ with $h/g = 10, 20$ and $27$ .	<b>50</b>
<b>Figure 4.23:</b> The specific heat $C_H$ per spin as a function of temperature $T/g$ at $k/g = -10$ for (a) $h/g = 10$ , (b) $h/g = 20$ and (c) $h/g = 27$ .	<b>52</b>
<b>Figure 4.24:</b> The specific heat $C_H$ as a function of temperature $T/g$ at $k/g = -10$ with $h/g = 10, 20$ and $27$ .	<b>53</b>
<b>Figure 4.25:</b> A plot of the total average energy $\langle E/g \rangle$ per spin as a function of $T/g$ at $k/g = 2$ for (a) $h/g = 10$ , (b) $h/g = 20$ and (c) $h/g = 27$ .	<b>55</b>
<b>Figure 4.26:</b> A plot of the total average energy $\langle E/g \rangle$ per spin as a function of $T/g$ at $k/g = 2$ with $h/g = 10, 20$ and $27$ .	<b>56</b>
<b>Figure 4.27:</b> A plot of the average dipolar energy $\langle E_{\text{dd}}/g \rangle$ per spin as a function of heating and cooling the system at $k/g = 2$ for (a) $h/g = 10$ , (b) $h/g = 20$ and (c) $h/g = 27$ .	<b>58</b>
<b>Figure 4.28:</b> A plot of the average anisotropy energy $\langle E_{\kappa}/g \rangle$ per spin as a function of heating and cooling the system at $k/g = 2$ for (a) $h/g = 10$ , (b) $h/g = 20$ and (c) $h/g = 27$ .	<b>59</b>
<b>Figure 4.29:</b> A plot of the average exchange energy $\langle E_{\text{ex}}/g \rangle$ per spin as a function of heating and cooling the system at $k/g = 2$ for (a) $h/g = 10$ , (b) $h/g = 20$ and (c) $h/g = 27$ .	<b>60</b>
<b>Figure 4.30:</b> A plot of the average Zemann energy $\langle E_h/g \rangle$ per spin as a function of heating and cooling the system at $k/g = 2$ for (a) $h/g = 10$ , (b) $h/g = 20$ and (c) $h/g = 27$ .	<b>61</b>
<b>Figure 4.31:</b> A plot of the average dipolar energy $\langle E_{\text{dd}}/g \rangle$ per spin as a function of $T/g$ at $k/g = 2$ for $h/g = 10, 20$ and $27$ .	<b>62</b>
<b>Figure 4.32:</b> A plot of the average anisotropy energy $\langle E_{\kappa}/g \rangle$ per spin as a function of $T/g$ at $k/g = 2$ for $h/g = 10, 20$ and $27$ .	<b>62</b>
<b>Figure 4.33:</b> A plot of the average exchange energy $\langle E_{\text{ex}}/g \rangle$ per spin as a function of $T/g$ at $k/g = 2$ for $h/g = 10, 20$ and $27$ .	<b>63</b>

<b>Figures</b>	<b>page</b>
<b>Figure 4.34:</b> A plot of the average Zeeman energy $\langle E_{h/g} \rangle$ per spin as a function of $T/g$ at $k/g = 2$ for $h/g = 10, 20$ and $27$ .	<b>63</b>
<b>Figure 4.35:</b> The specific heat $C_H$ per spin as a function of heating and cooling the system at $k/g=2$ for (a) $h/g= 10$ , (b) $h/g= 20$ and (c) $h/g= 27$ .	<b>65</b>
<b>Figure 4.36:</b> The specific heat $C_H$ per spin for heating and cooling the system at $k/g=2$ with $h/g = 10, 20$ and $27$ .	<b>66</b>
<b>Figure 4.37:</b> The magnetic phase diagram as a function of both $k/g$ and $T/g$ for $h/g=10$ . Region I is the planar antiferromagnetic phase, Region II is the perpendicular antiferromagnetic phase, and Region III is the paramagnetic (or disordered) phase. The two solid lines highlight the two lines of second order transition from the two antiferromagnetic order states to the paramagnetic phase. The dashed line highlights the line of first ordered transition between the planar and the perpendicular phases.	<b>69</b>
<b>Figure 4.38:</b> The magnetic phase diagram as a function of both $k/g$ and $T/g$ for $h/g=20$ . Region I is the planar antiferromagnetic phase, Region II is the perpendicular antiferromagnetic phase, and Region III is the paramagnetic (or disordered) phase. The two solid lines highlight the two lines of second order transition from the two antiferromagnetic order states to the paramagnetic phase. The dashed line highlights the line of first ordered transition between the planar and the perpendicular phases.	<b>70</b>
<b>Figure 4.39:</b> The magnetic phase diagram as a function of both $k/g$ and $T/g$ for $h/g=27$ . Region I is the planar antiferromagnetic phase, Region II is the perpendicular antiferromagnetic phase, and Region III is the paramagnetic (or disordered) phase. The two solid lines highlight the two lines of second order transition from the two antiferromagnetic order states to the paramagnetic phase. The dashed line highlights the line of first ordered transition between the planar and the perpendicular phases.	<b>71</b>

<b>Figure</b>	<b>page</b>
<b>Figure 4.40:</b> The magnetic phase diagram as a function of both $k/g$ and $T/g$ for $h/g = 10$ , $h/g = 20$ and $h/g = 27$ . Region I is the planar antiferromagnetic phase, Region II is the perpendicular antiferromagnetic phase, and Region III is the paramagnetic phase.	<b>72</b>

# **Influences of a Uniform External Magnetic Field on the Magnetic Properties of the Dipolar Anti-ferromagnetic Heisenberg System:**

**By**

**Thaer " Mohammed Said" Mustafa Abu-Labdeh**

**Supervised by**

**Dr. Abdel-Rahman Mustafa Abu-Labdeh**

## **Abstract**

The effects of a uniform external parallel magnetic field, with strength  $h$ , on the magnetic properties of the Heisenberg system on a square lattice of size  $32 \times 32$  have been investigated using Monte Carlo (MC) method. The model consists of three dimensional classical spin vectors in which the spins interact through the dipolar interaction, the magnetic surface anisotropy, the antiferromagnetic exchange interaction and a uniform external magnetic field along x-axis of the square lattice. The relative exchange parameter  $J/g$ , where  $g$  is the strength parameter of the dipolar parameter and  $J$  is the strength parameter of the exchange interaction, is fixed at the value  $-10$  (i.e.,  $J/g = -10$ ). From a series of MC simulations, the magnetic phase diagrams for this system have been determined as a function of both the relative magnetic surface anisotropy parameter  $\kappa/g$ , where  $\kappa$  is the strength parameter of the magnetic surface anisotropy, and temperature  $T/g$  for three selected values  $h/g$  (i.e.,  $h/g = 10, 20$  and  $27$ ). At low temperatures and for  $k/g \geq -4$  the phase diagrams show perpendicular antiferromagnetic phase; while for  $k/g \leq -4$  the equilibrium

phase is planer antiferromagnetic phase. The MC results also show that the phase boundary separating the two ordered phases appears to be first order with very small latent heat. Moreover, the MC results indicate that the phase boundary separating the two ordered states from the paramagnetic phase is second order. While the sequence of phases observed for deferent values of  $h$  is similar, at very low temperature the results show that the line of the first order transitions between the two ordered phases shifts towards the negative values of  $\kappa/g$ , with decreasing in its slope as the external field is increased. In addition, the MC results show that, both the perpendicular and planer phases are shrink as the applied field is increased.

# **Chapter 1**

## **Introduction**

## Chapter 1

### Introduction

Every electron, on account of its spin, is a small magnet. In most materials, the countless electrons have randomly oriented spins, leaving no magnetic effect on average. However, in a bar magnet many of the electron spins are aligned in the same direction, so they act cooperatively, producing a net magnetic field. In addition to the electron's intrinsic magnetic field, there is sometimes an additional magnetic field that results from the electron's orbital motion about the nucleus. Ordinarily, the orbital motion of the electrons is in such way that there is no average field from the material. In certain conditions, however, the motion can line up so as to produce a measurable total field. The overall magnetic behavior of a material can vary widely, depending on the structure of the material, and particularly on its electron configuration. Several forms of magnetic behavior have been observed in different materials, including : diamagnetism, paramagnetism, ferromagnetism, ferrimagnetic and antiferromagnetism [1, 2, 3].

Diamagnetism is the property of an object which causes it to produce a magnetic field in opposition of an externally applied magnetic field, and hence causing a repulsive effect. Consequently, diamagnetism is a form of magnetism that is only exhibited by a substance in the presence of an externally applied magnetic field. It is, generally, a quite weak effect in most materials. So diamagnetic materials are those with a magnetic

permeability  $\mu$  less than  $\mu_0$ , where  $\mu_0$  is the permeability of vacuum (or equivalently, those with negative susceptibility) [4, 5].

Paramagnetic is a form of magnetism which occurs only in the presence of an externally applied magnetic field. Paramagnetic materials are attracted to magnetic fields, hence have a relative magnetic permeability ( $\mu/\mu_0$ ) greater than one (or, equivalently, have a positive magnetic susceptibility). The magnetic moment induced by the applied field is linear in the field strength and rather weak [4, 5, 6, 7].

Ferromagnetism is the basic mechanism by which certain materials (such as iron) form permanent magnets and/ or exhibit strong interactions with magnets. It is responsible for most phenomena of magnetism encountered in everyday life such as, refrigerator magnets[5, 6, 7]. All permanent magnets (materials that can be magnetized by an external magnetic field and which remain magnetized after the external field is removed) are either ferromagnetic or ferrimagnetic. If some of the magnetic ions subtract from the net magnetization (if they are partially anti-aligned), then the material is ferrimagnetic. If the ions anti-align completely so as to have zero net magnetization, despite the magnetic ordering, then it is an antiferromagnetic. All of these alignment effects only occur at temperatures below a certain critical temperature, called the Curie temperature for ferromagnets and ferrimagnets or the Néel temperature for antiferromagnets. Above the Néel temperature and Curie temperature the material is typically paramagnetic (or in disorder state) [8, 9].

The magnetic properties of a material are also affected by the composition and dimensions of a system. According to the dimensionality of system, magnetic materials can be divided into two kinds [10, 11], bulk

and low dimensional. In the case of bulk systems a lot of work have been done, while in reduced dimensional spin systems a few systematic work have been carried out [10, 11].

one important class of reduced dimensional magnetic materials is quasi two-dimensional systems. Quasi two-dimensional systems have received much greater attention because of their magnetic properties and their technological applications as magnetic sensors, recording and storage media [10, 11]. Quasi two-dimensional systems include three important magnetic systems: ultra thin Magnetic Films, layered magnetic compounds and micro (or nano) magnetic dot arrays .

The Ultra thin magnetic films consist of several mono-layers of magnetic atoms deposited on a non-magnetic substrate, such as Fe on Cu(111) substrate [12], Gd on W(110) substrate, or Ni on Cu(001) substrate [13, 14]. Although the technological importance of the antiferromagnetic thin films, few research have been done on these films due to the inability of conventional method to spatially determine the microscopic magnetic structure of antiferromagnetic thin films [15, 16]. Recently, by the use of X-ray magnetic linear dichroism spectroscopy this problem has been partially solved. However, antiferromagnetic thin films remain an experimental and theoretical challenge [ 17, 18, 19, 20].

At low temperatures it was found that the magnetic spins of such films are observed to be ordered. One important phenomenon found to

occur in the such films is a reorientation transition, in which the magnetization switches from perpendicular (out-of-plane) to parallel (in-plane) (or vice versa) [21, 22, 23, 24] as temperature (or the film thickness) is increased [23, 25, 26, 27, 28, 29, 30, 31].

The layered magnetic compounds is the second important class of quasi-two-dimensional systems. In these compounds there is one ion per unit cell, and the c-axis is approximately three time as long the a-axis and b-axis [32, 33]. The rare earth layered magnetic compounds, for example, are strong candidates for investigating the interplay between magnetism and superconducting. At low temperature ( $< 2^{\circ}\text{K}$ ), it was pointed out that nearly all rare earth ions in such compounds show antiferromagnetic ordering and this ordering phase coexists with the superconducting phase. In the case of Erbium magnetic compound, for example, neutron-scattering technique showed that below Néel temperature ( $T_N \approx 0.50^{\circ}\text{K}$ ) its magnetic spins are ordering within the ab-plane (i.e., in the b direction the magnetic spins are aligned ferromagnetically and in the a direction are aligned antiferromagnetically). This phase is called as the dipolar antiferromagnetic (or collinear) phase [34, 35, 36, 37, 38, 39, 40].

The magnetic micro (or nano) particles is the third important class of quasi-two-dimensional systems. It includes arrays of magnetic wires with diameters of only a few micro (or nano-metera), and magnetic micro (or nano) particles such as dots, rings and tubes [41, 42, 43, 44, 45, 46, 47, 48,

49]; that they might be used in the production of new magnetic devices, specially in recording media [50, 51, 52].

It was found the interaction among the magnetic micro (or nano) wires can be best described by two dimensional model. So it is possible to test micro (or nano) magnetic systems and verify the best conditions for optimizing the macroscopic magnetic behavior for specific applications. The magnetization of ferromagnetic nano wire arrays has already been studied using the magnetic force microscopy (MFM) [53, 54, 55]. MFM measurements have been carried out by applying magnetic fields on magnetized and demagnetized samples to study the switching behavior of individual nanowires and to obtain the hysteresis loops of the nano wire arrays. In the equilibrium state, it was found that the nano wires exhibit a homogeneous magnetization along the axial direction.

Most growth in the electromagnetic media is referred to new discoveries and a better understanding of magnetic and electronic properties of low dimensional systems. The stability of the magnetic ordering in the low-dimensional systems are affected by some factors such as their sensitively to an applied magnetic field and the type and nature of the interactions that have present in a certain order [56]. Therefore, theoretical studies have identified models that effectively divide such magnetic system into three main types based on the dimensionality of the spin. The first model is the Ising model, in which the spins are perpendicular to the plane of the system because of the strong magnetic

surface anisotropy. The second model is the plane rotator model, in which the spins are confined to rotate freely in the plane of the system due to the strong planar surface anisotropy. The third model is the Heisenberg model, in which the spins have three dimensional components. Any theoretical model for low-dimensional magnetic systems should include the exchange interaction, the dipolar interaction and the magnetic surface anisotropy [57]. The dipolar interaction plays critical role in determining the magnetic properties of low-dimensional magnetic systems because of its long-range and anisotropic nature. For example, in the two dimensional plane rotator system it was found that the only short-range exchange interaction is insufficient for establishing a spontaneous magnetization at any finite temperature [58, 59].

Heisenberg ferromagnetic systems include all the three interactions (exchange interaction, dipolar interaction, and uniaxial magnetic surface anisotropy) have been studied extensively using different methods such as renormalization group calculations [60, 61, 62, 63], mean-field calculations [64, 65, 66, 67], Monte Carlo simulations [68, 69, 70, 71, 72] and spin-wave analysis [73, 74, 75, 76]. In general, these studies predict the existence of a reorientation transition from an out-of-plane ferromagnetic state at low temperature to an in-plane ferromagnetic state as the temperature increases. This agrees well with the experimental findings from most of the research with ferromagnetic ultrathin films.

In contrast, a few systematic works have been carried out on the antiferromagnetic Heisenberg system. The classical two-dimensional dipolar antiferromagnetic spin systems on a square lattice have been investigated by Abu-Labdeh *et al* [77, 78, 79, 80, 81, 82, 83] using Monte Carlo simulations. These studies show a wide range of ordering effects where a reorientation transition has been found.

Abu-Labdeh *et al* [80] investigated the two dimensional dipolar antiferromagnetic Heisenberg system on a square lattice without magnetic surface anisotropy ( $\kappa = 0$ ) for both zero and finite temperatures. At low temperatures, their Monte Carlo results showed that the system exhibits a reorientation transition from the dipolar antiferromagnetic planer phase to the perpendicular antiferromagnetic phase as the antiferromagnetic exchange paramagnetic increases. Also, their results showed also that the phase boundary separating the two order phase is a first order transition with weakly dependent on temperature. In addition, their results concluded that the phase boundary separating the two order state from paramagnetic state appears to be a second order transition .

The magnetic properties for two dimensional dipolar antiferromagnetic Heisenberg model on a square lattice with a weak planar magnetic surface anisotropy ( $\kappa/g = -1.0$ ) and with a weak perpendicular magnetic surface anisotropy ( $\kappa/g = 1.0$ ) have also been determined for both zero and finite temperatures by Abu-Labdeh *et al* [81]. Their study showed three distinct magnetic phases: the dipolar planar antiferromagnetic, the

perpendicular antiferromagnetic and the paramagnetic phase. Their Monte Carlo results pointed out that the phase boundaries between the two ordered phase and the paramagnetic phase appears to be second order transition; while the phase boundary between the two ordered phases appears to be a first order transition. Their Monte Carlo results also demonstrated that the system with  $\kappa/g = -1$  can exhibit a reorientation transition from the dipolar planar antiferromagnetic phase to the perpendicular antiferromagnetic phase with increasing temperature, and with  $\kappa/g = 1$  the system can exhibit a reorientation transition from the perpendicular antiferromagnetic phase to dipolar planer antiferromagnetic phase with increasing temperature.

Abu-Labdeh *et al* [82] also investigated Heisenberg antiferromagnetic system on a square lattice in which the spins interact through the long-range dipolar interaction, a magnetic surface anisotropy and exchange interaction. The exchange interaction  $J$  was assumed to be antiferromagnetic and fixed at the value  $-10g$  (i.e.,  $J/g = -10$ ). Their Monte Carlo results showed the relevant states are antiferromagnetic in which every spin is aligned in the opposite direction to its neighbours. The orientation of the antiferromagnetic state is determined by the strength of the dipolar interaction, which favours the perpendicular antiferromagnetic phase, and the magnetic surface anisotropy, which for  $\kappa < 0$  favours the planar antiferromagnetic state. Simulations for small values of  $|\kappa|$  show a finite perpendicular antiferromagnetic order parameter which decreases with increasing temperature until the system undergoes a second order

phase transition to the paramagnetic phase at the Néel temperature, at which point the order parameter is effectively zero. A similar behaviour is observed for large values of  $|\kappa|$ , with the difference that the ordered phase is the planar phase. For intermediate values of  $\kappa$  there exists a narrow range around  $|\kappa| \approx \kappa_0$  for which the system undergoes a reorientation transition from the planar to the perpendicular phase with increasing temperature. The almost discontinuous change in the order parameters, and the hysteresis observed in the Monte Carlo data at the reorientation transition all indicate that it is a first order transition. As the temperature is further increased the system undergoes a second order transition to the paramagnetic phase.

Recently, Abu-Labdeh *et al* [83] studied the Heisenberg antiferromagnetic system on a square lattice having the long-range dipolar interaction, a short-range antiferromagnetic exchange interaction, a magnetic surface anisotropy and a uniform applied magnetic field along the  $z$ -axis at finite temperatures using Monte Carlo simulation. From their Monte Carlo simulations, the magnetic phase diagram was determined for the system as a function of the applied field and temperature. At low temperatures and for low values of the applied field, their Monte Carlo results show the phase boundary separating the dipolar planar antiferromagnetic phase and the perpendicular antiferromagnetic phase is a first order transition with a very small amount of hysteresis, where the amount of the hysteresis is decrease as  $h/g$  is increased. In addition, the

reorientation transition line between the two ordered states at very low temperature shifts down with decreasing in slope as  $h$  is increased. In contrast, the phase boundary separating the two ordered phase from the paramagnetic phase appears to be second order transition with clear continuous and lack of hysteresis. Moreover, the regions of the perpendicular and planar antiferromagnetic states are shrink as the applied field is increased.

As mentioned before, little is known about the effects that arise from the interplay of the dipolar, exchange, magnetic surface anisotropy and uniform external magnetic field in the low-dimensional antiferromagnetic systems. The development of the quasi-two-dimensional magnetic systems for particular applications needs a detailed understanding of their microscopic interactions. Therefore, this study focuses on the effects of a parallel uniform external magnetic field on the magnetic properties of the dipolar antiferromagnetic Heisenberg system with heating, cooling, increasing and decreasing the strength of the surface anisotropy.

The outline of this thesis is as follows. Chapter two presents the Heisenberg model in general terms including the dipole-dipole interaction, exchange interaction, magnetic surface anisotropy and uniform external magnetic field. Chapter three introduces the basic methods behind Monte Carlo simulation technique and the computational aspects. Chapter four presented and discussed the results for the system of interest. Finally, Chapter five gives the conclusion.

## **Chapter 2**

### **The Model in General Terms**

## Chapter 2

### The Model in General Terms

This study presents the results from series of Monte Carlo simulations on the Heisenberg model of antiferromagnetic spin system. The system is a two-dimensional square lattice of  $N = L \times L = 32 \times 32$  classical spins of fixed length. The suitable boundary conditions are imposed on the system by constructing an infinite plane from replicas of a finite system and using the Ewald summation techniques to sum over the replicas.

For the system of interest the two in-plane directions of the square lattice are denoted by  $\hat{x}$  and  $\hat{y}$ , and the direction perpendicular to the plane is denoted by  $\hat{z}$ . Each lattice site is associated with an ion which has a total magnetic moment  $\vec{m}$ , and a total spin  $\vec{S}$ ; where are confined to rotate freely in the plane of the system.

In this model, the magnetic ions are assumed to interact through the exchange interaction ( $E_{ex}$ ), the dipolar interaction ( $E_{dd}$ ), the magnetic surface anisotropy ( $E_k$ ) and a uniform applied magnetic field ( $E_h$ ), which represents the contribution of a uniform external magnetic field along the  $x$ -axis of the square lattice. So, the total energy of the considered model can be written as

$$E = E_{ex} + E_{dd} + E_k + E_h \quad (2.1)$$

The first term of Equation 2.1 is the nearest neighbor exchange interaction. The simplest case of the exchange interaction between two ions spins  $\vec{S}_1$  and  $\vec{S}_2$  is given by

$$E_{ex} = -\mathfrak{J} \vec{S}_1 \cdot \vec{S}_2 \quad (2.2)$$

where  $\mathfrak{J}$  is the strength exchange interaction which depends on the distance between the spins, and it is determined by the overlap integrals.

For negative exchange parameter, an antiparallel spin orientations is preferred, which leads to a simple antiferromagnetic state. While for positive parameter  $\mathfrak{J}$ , a parallel spin orientations is favored, which leads to ferromagnetic state.

The exchange interaction has features of short-range characters, and it has an isotropic nature. For a system of N spins, the exchange energy is then given by

$$E_{ex} = -\mathfrak{J} \sum_{\langle i, j \rangle} \vec{S}_i \cdot \vec{S}_j \quad (2.3)$$

where the sum is over all nearest neighbor pairs, and  $\vec{S}_i$  is the classical spin vector at site  $i$ .

The second term of Equation 2.1 is the dipole-dipole interaction. In contrast to the exchange interaction, the dipolar interaction between any

two moments on the lattice decays slowly with distance between any magnetic ions, and its anisotropic. The dipolar interaction is then given by

$$E_{dd} = \frac{1}{2} \sum_{i \neq j} \left( \frac{\vec{m}_i \cdot \vec{m}_j}{r_{ij}^3} - 3 \frac{(\vec{m}_i \cdot \vec{r}_{ij})(\vec{m}_j \cdot \vec{r}_{ij})}{r_{ij}^5} \right) \quad (2.4)$$

where  $\vec{m}_i$  is the classical magnetic moment at the lattice site  $i$ ,  $\vec{r}_{ij}$  is the vector connecting site  $i$  to site  $j$  and the sum is over all possible pairs of sites in the lattice except  $i = j$ .

The third term of Equation on 2.1 is the magnetic surface anisotropy which arises from the interaction of spins with the crystal environment. This coupling can result in a preferred axis (or axes) about which the system may be favorably ordered energetically. The existence of such an easy axis (or axes) can have any one of a number of causes. In the system of interest, it is sufficient to include the case where the anisotropy couples the component of the magnetic moment that is perpendicular to the surface due to the symmetry between the two in-plane directions. The magnetic surface anisotropy term with the z-axis perpendicular to the surface of the system is

$$E_k = -\lambda \sum_i [m_z(\vec{r}_i)]^2 \quad (2.5)$$

where the sum is over all sites in the lattice,  $m_z(\vec{r}_i)$  is the  $\hat{z}$  component of the moment vector at site  $i$ , and  $\lambda$  is the strength of the magnetic surface

anisotropy. When  $\lambda$  is positive an easy axis occurs along  $\hat{z}$ , and when  $\lambda$  is negative an easy plane occurs within the system.

Finally, the last term of Equation 2.1 refers to the Zeeman energy. This energy arises from the interaction between the magnetic moment of the ions and the applied magnetic field. As mentioned before, it has an important role in characterizing the development of materials for specific application. For example the time of manufacture the materials is very sensitive to the application of a magnetic field. Indeed, the wide use of technological applications such as data storage often requires manipulation of the magnetic structure by an external magnetic field [84].

The contribution of Zeeman term to the total energy of the system is given by

$$E_h = - \sum_i \vec{B} \cdot \vec{m}(r_i) \quad (2.6)$$

Where  $\vec{B}$  is the applied magnetic field and sum is over all sites in the lattice. Since the present study includes an applied field  $\vec{B}$  along the x-axis, Equation 2.6 can be written as

$$E_h = -B \sum_i m_x(r_i) \quad (2.7)$$

where  $B$  is the magnitude of the applied field and  $m_{x,i}$  is the x-component of the magnetic moment.

To use Equations 2.3, 2.4, 2.5 and 2.7 in the Monte Carlo simulations, it is needed to write them as dimensionless equations [79, 85, 86]. To do this, a set of two-dimensional classical unit vectors  $\{\vec{\mathcal{S}}\}$  is defined such that

$$\vec{\mathcal{S}}(\vec{r}_i) \equiv S_{eff} \vec{\mathcal{S}}(\vec{r}_i) \quad (2.8)$$

and

$$\vec{m}(\vec{r}_i) \equiv m_{eff} \vec{\mathcal{S}}(\vec{r}_i) \quad (2.9)$$

where

$$|\vec{\mathcal{S}}(\vec{r}_i)| = 1 \quad (2.10)$$

In addition, all distances are scaled by the lattice constant  $a$ , such that

$$\vec{R}_i \rightarrow \frac{\vec{r}_i}{a}$$

Substituting these new definitions into Equations 2.3, 2.4, 2.5 and 2.7 we get

$$E_{ex} = -\mathfrak{J} S_{eff}^2 \sum_{\langle i,j \rangle} \vec{\mathcal{S}}(\vec{R}_i) \cdot \vec{\mathcal{S}}(\vec{R}_j) \quad (2.11)$$

$$E_{dd} = \frac{m_{eff}^2}{2a^3} \sum_{i \neq j} \left( \frac{\vec{\mathcal{S}}(\vec{R}_i) \cdot \vec{\mathcal{S}}(\vec{R}_j)}{R_{ij}^3} - 3 \frac{[\vec{\mathcal{S}}(\vec{R}_i) \cdot \vec{R}_{ij}][\vec{\mathcal{S}}(\vec{R}_j) \cdot \vec{R}_{ij}]}{R_{ij}^5} \right) \quad (2.12)$$

$$E_k = -l (m_{z,eff})^2 \sum_i [S_z(\vec{R}_i)]^2 \quad (2.13)$$

and

$$E_h = -B m_{eff} \sum_i S_x(\vec{R}_i) \quad (2.14)$$

For simplicity, we define new coupling parameters

$$J = \mathfrak{S} S_{eff}^2 \quad (2.15)$$

$$g = \frac{m_{eff}^2}{2a^3} \quad (2.16)$$

$$k = l (m_{z,eff})^2 \quad (2.17)$$

and

$$h = B m_{eff} \quad (2.18)$$

where  $J$  is the strength parameter of the exchange interaction,  $g$  is the strength parameter of the dipolar interaction,  $\kappa$  is the strength parameter of the magnetic surface anisotropy and  $h$  is the strength parameter of the applied field. Substituting Equations 2.15, 2.16, 2.17 and 2.18 into Equations 2.11, 2.12, 2.13 and 2.14 yields

$$E_{ex} = -J \sum_{\langle i,j \rangle} \vec{S}(R_i) \cdot \vec{S}(R_j) \quad (2.19)$$

$$E_{dd} = g \sum_{i \neq j} \left( \frac{\vec{s}(\vec{R}_i) \cdot \vec{s}(\vec{R}_j)}{R_{ij}^3} - 3 \frac{[\vec{s}(\vec{R}_i) \cdot \vec{R}_{ij}] [\vec{s}(\vec{R}_j) \cdot \vec{R}_{ij}]}{R_{ij}^5} \right) \quad (2.20)$$

$$E_k = -k \sum_i [s_z(\vec{R}_i)]^2 \quad (2.21)$$

and

$$E_h = -h \sum_i s_x(\vec{R}_i) \quad (2.22)$$

Finally, substituting Equations 2.19, 2.20, 2.21 and 2.22 into Equation 2.1 gives

$$E = -J \sum_{\langle i,j \rangle} \vec{s}(\vec{R}_i) \cdot \vec{s}(\vec{R}_j) + g \sum_{i \neq j} \left( \frac{\vec{s}(\vec{R}_i) \cdot \vec{s}(\vec{R}_j)}{R_{ij}^3} - 3 \frac{[\vec{s}(\vec{R}_i) \cdot \vec{R}_{ij}] [\vec{s}(\vec{R}_j) \cdot \vec{R}_{ij}]}{R_{ij}^5} \right) - k \sum_i [s_z(\vec{R}_i)]^2 - h \sum_i s_x(\vec{R}_i) \quad (2.23)$$

In this study,  $J$ ,  $\kappa$  and  $h$  are given in units such that  $g = 1$ , and the exchange interaction  $J$  is assumed to be antiferromagnetic and fixed at the value  $-10g$  (i.e.,  $J/g = -10$ ). We choose the value of  $J/g$  to be  $-10$  in order to compare the present results with earlier work [82, 83].

The observable quantities of interest for the investigated system need to be determined. In this research, the most likely candidates for these observable quantities are the average energy  $\langle E \rangle$  and the heat capacity  $C_H$ .  $C_H$  is calculated from the energy fluctuation-dissipation formula

$$C_H = \frac{\partial E}{\partial T} = \frac{\langle E^2 \rangle - \langle E \rangle^2}{K_B T^2} \quad (2.24)$$

where  $K_B$  is the Boltzmann constant and  $T$  is the temperature measured in units of  $1/k_B$ . Given the total energy  $E$  every  $n^{\text{th}}$  MCS/site,  $C_H$  can be averaged over the whole time period of simulation.

The model given by Equation 2.23 will be investigated by using Monte Carlo simulation as present in chapters three and four.

## **Chapter 3**

### **Monte Carlo Simulations and Computational Details**

## Chapter 3

### Monte Carlo Simulations and Computational Details

#### 3.1 Introduction

For scientists, engineers, statisticians, managers, investors and others, computers have made it possible to make models that simulate reality and aid in making predictions. One of the methods for simulating real systems is the ability to take into account randomness by investigating hundreds of thousands of different systems. The results are then compiled and used to make decisions. This is what Monte Carlo (MC) simulation is about.

Monte Carlo (MC) methods are a class of computational algorithms based on repeated random sampling to compute the characteristics of a system of interest. MC methods are often used to simulate physical and mathematical systems. Because of their reliance on repeated computation and random numbers, MC methods are most suited calculation by a computer. MC methods tend to be used when it is infeasible (or impossible) to compute an exact result [87, 88]. MC methods are, especially, useful in studying systems with a large number of coupled degrees of freedom, such as fluids, disordered materials, strongly coupled solids, and cellular structures. A classic use of MC methods is for the evaluation of definite integrals, particularly, multidimensional integrals with complicated boundary conditions. The term Monte Carlo method was pointed out in the 1940s by physicists working on nuclear weapon projects in the Los Alamos National Laboratory [89].

MC methods are very important in computational physics, physical chemistry and related applied fields. In addition, MC methods are used in

the ensemble models that form the basis of modern weather forecasting operations[87, 88, 89].

Therefore, the aim of MC simulations is to evaluate thermal averages by statistically sampling the significant region of their phase space using a computer. For carrying out a MC simulation, we require a sequence of numbers which are random, independent, real and uniformly distributed in the range 0 to 1[77].

In this Chapter, we will present (in brief) the fundamentals of Monte Carlo simulations, including importance sampling, transition probability, detailed balance, and the Metropolis algorithm [77, 90, 91, 92, 93, 94, 95].

### 3.2 Importance Sampling and Detailed Balance

In statistics, importance sampling is a general technique for estimating the properties of a particular distribution. In the canonical ensemble this requires to average an observable quantity,  $Q$ , over all the states of the system weighting each by Boltzmann probability

$$P(u_g) \propto \exp\left[-\frac{E_{u_g}}{T}\right] \quad (3.1)$$

where  $E_{u_g}$  is the energy of the system in state  $u_g$ ,  $T$  is the temperature measured in units of  $1/k_B$ . Thus, the average value of the observable quantity  $Q$  is given by

$$\langle Q \rangle = \frac{\sum_g Q_{u_g} \exp\left[-\frac{E_{u_g}}{T}\right]}{\sum_g \exp\left[-\frac{E_{u_g}}{T}\right]} \quad (3.2)$$

where  $Q_{u_g}$  is the value of  $Q$  at some state  $u_g$ .

Without using the importance sampling method, billions of years are needed to sample (for example) the Ising spin system of 100 spins. Performing the importance sampling based on the Boltzmann probability distribution, enable us to find  $\langle Q \rangle$  by collection Equation 3.2 over a finite number of states, which are statistically significant.

When dealing with many states, Markov process is needed to sample the significant state. In this process, state  $\mathbf{u}_{g+1}$  is generated from previous state  $\mathbf{u}_g$  through a transition probability  $W(\mathbf{u}_g \rightarrow \mathbf{u}_{g+1})$ , such that the distribution function of the states generated by the Markov process is given by the Boltzmann distribution. Therefore, Markov process must have the following four conditions:

- 1- The state  $\mathbf{u}_{g+1}$  is generated every time it is determined by the state  $\mathbf{u}_g$ .
- 2- Reaching any state of the system from any other state is possible if the program is run for a long enough time.
- 3- The transition probability  $W(\mathbf{u}_g \rightarrow \mathbf{u}_{g+1})$  should satisfy the condition

$$\sum_g W(\mathbf{u}_g \rightarrow \mathbf{u}_{g+1}) = 1 \quad (3.3)$$

- 4- The rate at which the system makes transition into (or out) of any state  $n$  must be equal. This means that

$$P(\mathbf{u}_g) W(\mathbf{u}_g \rightarrow \mathbf{u}_{g+1}) = P(\mathbf{u}_{g+1}) W(\mathbf{u}_{g+1} \rightarrow \mathbf{u}_g) \quad (3.4)$$

or

$$\frac{W(\mathbf{u}_g \rightarrow \mathbf{u}_{g+1})}{W(\mathbf{u}_{g+1} \rightarrow \mathbf{u}_g)} = \frac{P(\mathbf{u}_{g+1})}{P(\mathbf{u}_g)} = \exp[-(E_{g+1} - E_g)] \quad (3.5)$$

Equation 3.5 indicates that the transition probability ratio for moving from state  $\mathbf{u}_g$  to state  $\mathbf{u}_{g+1}$  depends only on the energy change

$$\Delta E = E_{g+1} - E_g \quad (3.6)$$

### 3.3 The Metropolis Algorithm

The Metropolis algorithm was proposed by Metropolis and his co-workers in 1953 in the simulation of hard-sphere gases [96]. The Metropolis algorithm is based on the notation of detailed balance that describes equilibrium for systems whose configurations have probability proportional to the Boltzmann factor [96], and its one efficient method for the transition probability that satisfies Equation 3.5. In this algorithm the transition probability from state  $\mathbf{n}_1$  to state  $\mathbf{n}_{1+1}$  reads.

$$W(\mathbf{u}_g \rightarrow \mathbf{u}_{g+1}) = \begin{cases} \exp[-\Delta E], & \text{if } E_{\mathbf{u}_{g+1}} > E_{\mathbf{u}_g} \\ 1, & \text{if } E_{\mathbf{u}_{g+1}} \leq E_{\mathbf{u}_g} \end{cases} \quad (3.7)$$

From Equation 3.7, we note the following:

1-If the energy of state  $\mathbf{u}_{g+1}$  is lower than or equal to the present state  $\mathbf{u}_g$ , then the transition to the new state  $\mathbf{u}_{g+1}$  is accepted.

2-If the state  $\mathbf{u}_{g+1}$  has a higher energy than the state  $\mathbf{u}_g$  then there is, still, a possibility to accept it. To accept a new state which has a higher energy than the present state, we choose a random number  $Z$  between 0 and 1. If the transition probability is greater than  $Z$ , then the new state  $\mathbf{u}_{g+1}$  is accepted, otherwise the new state is rejected and then the system stays in the present state  $\mathbf{u}_g$ . In moving from  $\mathbf{u}_g$  to  $\mathbf{u}_{g+1}$ , there are many choices

which are only restricted by the condition of the detailed balance. In the present study the common and efficient choice is to change only the two degrees of freedom,  $\theta$  and  $f$ , of the selected spin (where  $0 \leq \theta \leq \pi$  and  $0 \leq f \leq 2\pi$ ).

The optimal Metropolis algorithm used in this study proceeds according to the following steps:

1. Randomly choose an initial state,  $\mathbf{u}_g$  for the system of interest,
2. Randomly select the target spin,  $\vec{s}_i$ , where  $i \in (1, 2, 3, \dots, N = L \times L)$ ,
3. Generate a new state,  $\mathbf{u}_{g+1}$ , randomly by changing the orientation of the selected  $\vec{s}_i$  to  $\vec{s}'_i$  such that

$$\vec{s}'_i = \vec{s}_i \pm \Delta \vec{s}_i \quad (3.8)$$

4. Compute the energy difference  $\Delta E$  between the new state  $\mathbf{u}_{g+1}$  and the old state  $\mathbf{u}_g$ .
5. Calculate the transition probability according to Equation 3.7.
6. Generate a uniform distribution number  $Z$  between 0 and 1.
7. Compare  $Z$  with the Calculated  $W(\mathbf{u}_g \rightarrow \mathbf{u}_{g+1})$ .
8. If  $W(\mathbf{u}_g \rightarrow \mathbf{u}_{g+1})$  is greater than  $Z$  accept the move, otherwise leave the spin as it is and retain the old spin configuration.
9. Repeat steps 2-8 as necessary.
10. Store the required observable quantities of the system every  $n^{\text{th}}$  Monte Carlo steps per lattice site ( $MCS/site$ ) to calculate the averages.
11. Calculate the required observable quantities of the system using the simple arithmetic average

$$\langle Q \rangle_M = \sum_{g=1}^M \frac{Q_{u_g}}{M} \quad (3.9)$$

where  $Q_{u_g}$  is the value of the observable quantity  $Q$  at the state  $u_g$  and  $M$  is the total number of the Monte Carlo steps per lattice site. Equation 3.9 indicates that  $\langle Q \rangle_M$  becomes a more and more accurate estimate as the number of *MCs/site* is increased.

### 3.4 Computational Aspects

In this thesis, the MC results for the Heisenberg system are carried out at finite temperatures using super-computing machine clusters through Western Canada Research Grid (WestGrid) at university of Calgary and Shared Hierarchical Academic Research Computing Network (SHARCNET) at university of Western Ontario.

The finite system considered in the present study has a lattice size  $N = 32 \times 32$ , and is treated as an infinite plane of replicas by imposing suitable periodic boundary conditions [77, 97, 98, 99]. In this system, the first site in a row in the square lattice is considered as the right of the nearest neighbor of another site in the same class and another site in a row is left as being the first row in the same location. The same holds for the top and bottom sites in each column. In addition, the Ewald summation technique is used to sum over the replicas [100]. Indeed, the simulations are based on the standard Metropolis algorithm [96]. The code used in this study was

originally written by MacIsaac and his co-workers [85, 86], and modified by Abu-Labdeh and his co-workers [77, 78, 79].

In the present study, the model is an  $N$  three-dimensional spins on a square lattice. The spin of each ion is treated classically, and it is represented by a vector of fixed magnitude ( $|\vec{s}_i| = 1, i = 1, 2, \dots, N$ ) and a changeable orientation in the space. In this thesis the system is investigated under, the nearest neighbors antiferromagnetic exchange interaction with relative strength  $J/g = -10$ , dipole-dipole interaction with relative strength  $g$ , magnetic surface anisotropy with relative strength  $\kappa/g$  and a uniform external magnetic field along x-axis with relative strength  $h/g$ .

Throughout this research, units of  $J$ ,  $\kappa$  and  $h$  are taken in terms of  $g$ . In addition, the temperature  $T$  is measured in a unit of  $1/k_B$ .

In the present study, Monte Carlo simulations data are collected by two ways

1- Fixing the temperature  $T/g$  at a particular value of  $h/g$  and then changing the relative magnetic surface anisotropy parameter  $\kappa/g$  by a 0.05 in each step.

2- Fixing the relative magnetic surface anisotropy parameter  $\kappa/g$  at a particular value of  $h/g$  and then changing the temperature  $T/g$  by a 0.05 in each step.

Through this study we aim to get a phase diagram as a function of both  $T/g$  and  $\kappa/g$  for each of the selected values of  $h/g$  (i.e.,  $h/g = 10, 20$  and  $27$ ).

## **Chapter 4**

### **Results and Discussion**

## Chapter 4

### Results and Discussion

#### 4.1 Introduction

In this chapter, we present and discuss the magnetic properties of the Heisenberg system on a square lattice with lattice size  $32 \times 32$ ; where the two in-plane directions are denoted by  $\hat{x}$  and  $\hat{y}$ , and the direction perpendicular to the plane is denoted by  $\hat{z}$ . As mentioned before, in the present system the long-range dipolar interaction, short-range exchange interaction, magnetic surface anisotropy and uniform applied magnetic field along the x- axis are considered. In addition, the strength of the exchange parameters is fixed at  $J = -10.0g$ . The phase behaviors for different values of  $\kappa$  with different values of the selected applied magnetic field ( $h/g = 10$ ,  $h = 20$  and  $h = 27$ ) are presented. The  $\kappa - T$  phase diagrams for  $h/g = 10$ ,  $h/g = 20$  and  $h/g = 27$ , therefore, have been constructed from the results of the Monte Carlo simulations.

#### 4.2 Finite Temperature Properties

At  $T/g = 2.5$ , the total average energy  $\langle E/g \rangle$  per spin with both increasing and decreasing  $\kappa$  for  $h/g = 10$ ,  $20$  and  $27$  are shown, respectively, in Figures 4.1a, 4.1b and 4.1c. To show the effect of the applied magnetic field on the total average energy, we plot Figures 4.1a, 4.1b and 4.1c in Figure 4.2. The data shown in Figure 4.1( or Figure 4.2) indicate that the system switches from the planar antiferromagnetic phase to the perpendicular antiferromagnetic phase (at  $\kappa_N/g = -4.057 \pm 0.025$ ,  $-4.195 \pm 0.025$  and  $-4.212 \pm 0.025$  for  $h/g = 10$ ,  $20$  and  $27$ , respectively) as the

strength of the magnetic surface anisotropy is increased. This transition consistent with the nature of magnetic surface anisotropy in which the easy axis occurs along  $\hat{z}$  for positive  $\kappa$  and it occurs within plan of the system for negative  $\kappa$ . In addition the data in Figure 4.1( or Figure 4.2) indicate that the total average energy of the planer phase is almost constant because in this phase the z-components of the spins are almost zero, and hence the magnetic anisotropy energy does not change with increasing  $\kappa$ . In contrast, the total average energy of the perpendicular phase is decreasing with increasing  $\kappa$  because the magnetic anisotropy energy is directly proportional to  $-\kappa$ .

Evidence for the existence of the planar antiferromagnetic phase at  $\kappa/g < \kappa_N/g$  and perpendicular antiferromagnetic phase at  $\kappa/g > \kappa_N/g$  is shown in Figures 4.3 and 4.4. Figures 4.3a, 4.3b and 4.3c show snapshots of spin configuration, at  $\kappa/g = -8 < \kappa_N/g$  with  $T/g = 2.5$  for  $h/g = 10, 20$  and  $27$ , respectively; while Figures 4.4a, 4.4b and 4.4c show snapshots of spin configuration at  $\kappa/g = 2 > \kappa_N/g$  with  $T/g = 2.5$  for  $h/g = 10, 20$  and  $27$ , respectively. In Figure 4.3 the spins are aligned antiferromagnetically parallel to the plane of the system (i.e., the system favors planar antiferromagnetic phase); where in Figure 4.4 the spins are aligned antiferromagnetically perpendicular to the plane of the system (i.e., the system favors perpendicular antiferromagnetic phase). Hence, at low temperature and for large negative values of  $\kappa$  the planar antiferromagnetic phase is energetically favored. As  $\kappa$  is increased the system switches from the planar antiferromagnetic phase to the perpendicular antiferromagnetic phase.

Moreover, the MC data presented in Figure 4.1 (or Figure 4.2) also indicate that the transition from the planar antiferromagnetic phase to the perpendicular antiferromagnetic phase is first order (or discontinues transition) with very small latent heat. This transition is characterized by a sharp change in the slope of the total energy with respect to  $\kappa$ . Table 4.1, therefore, summarizes the locations of the transition points between the two order phases at  $T/g = 2.5$  for  $h/g = 10, 20$  and  $27$ .

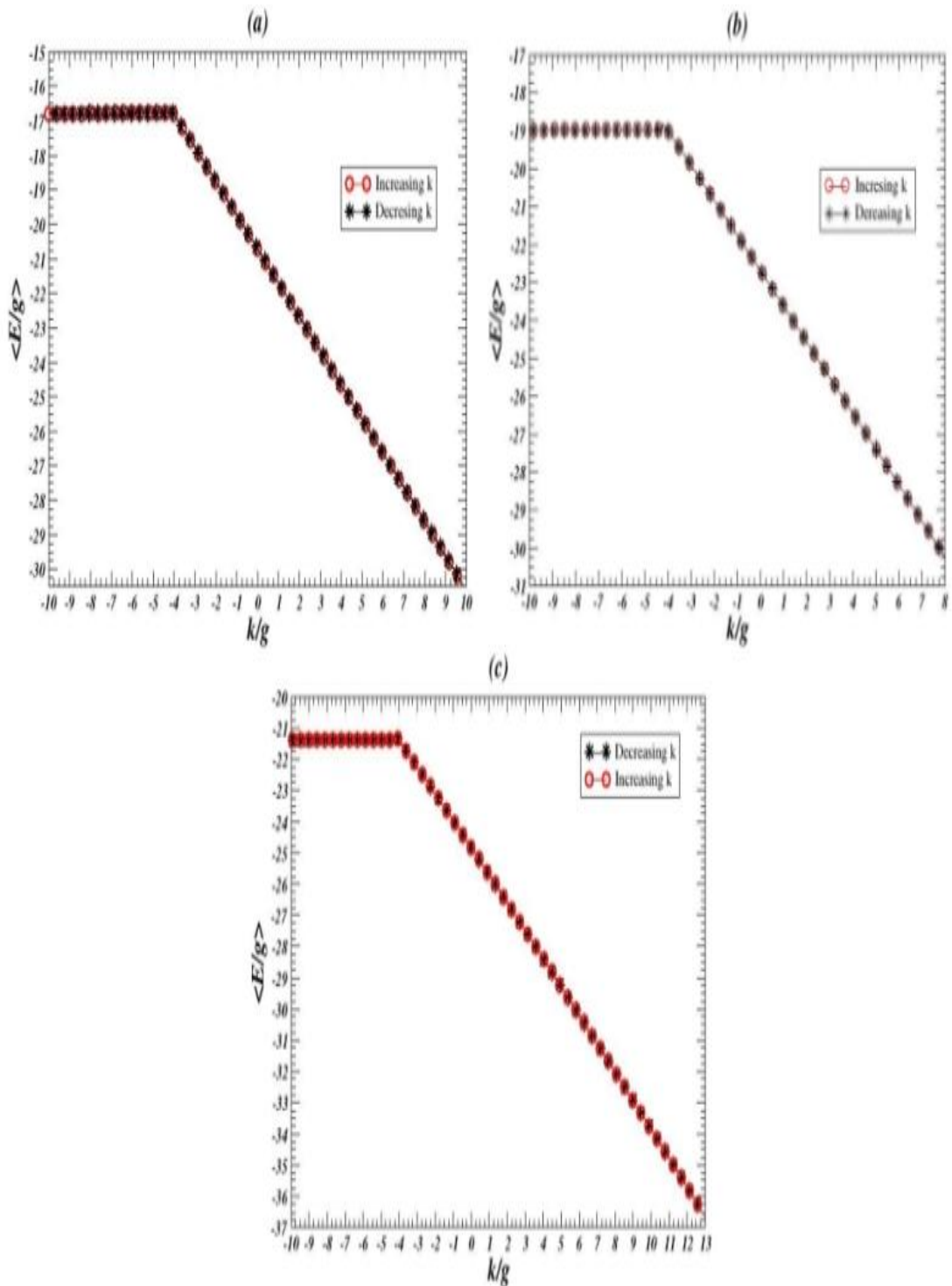


**Figure 4.1:** A plot of the total average energy  $\langle E/g \rangle$  per spin as a function of increasing and decreasing the relative magnetic surface anisotropy parameter  $\kappa/g$  at  $T/g = 2.5$  for (a)  $h/g = 10$ , (b)  $h/g = 20$  and (c)  $h/g = 27$ .

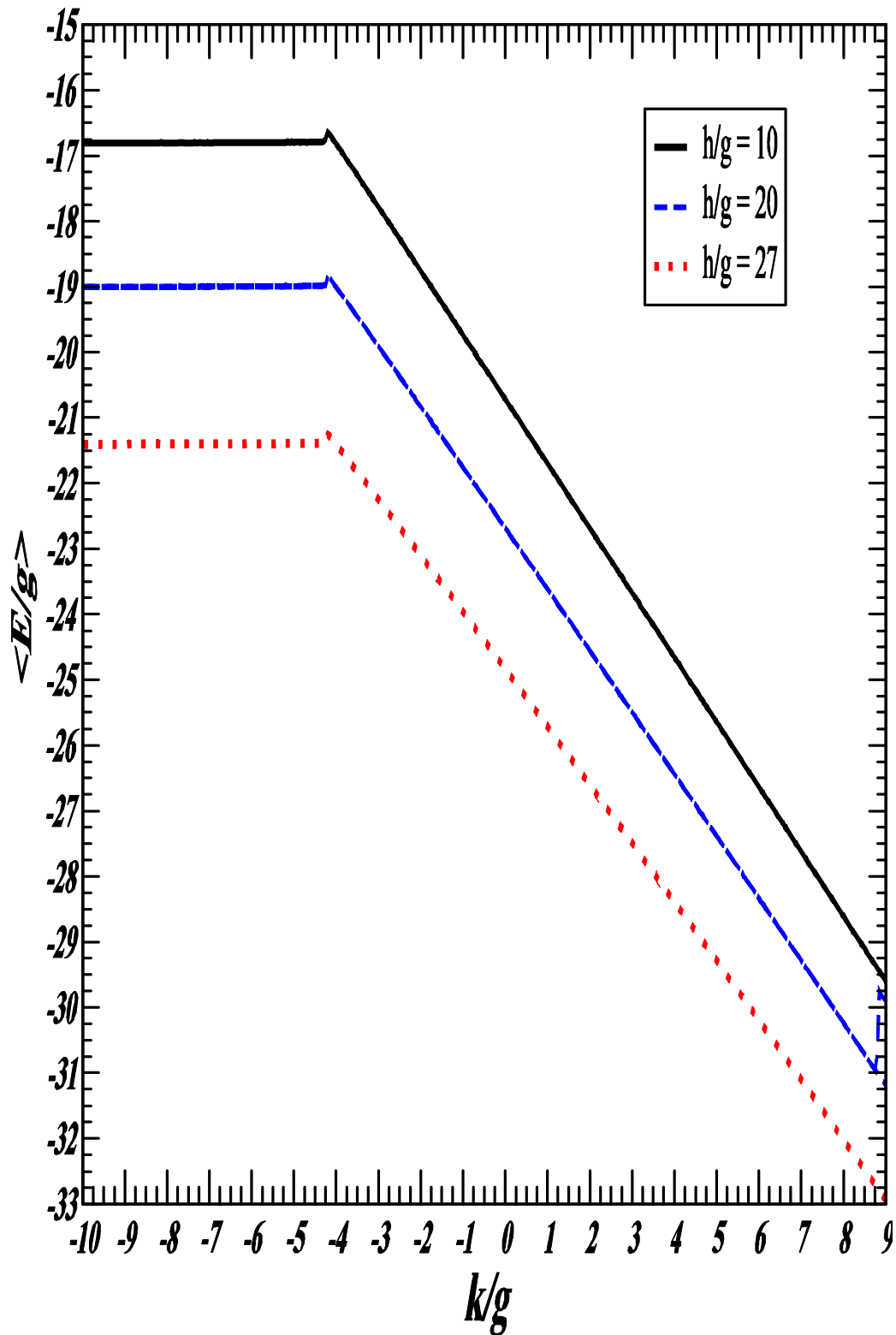
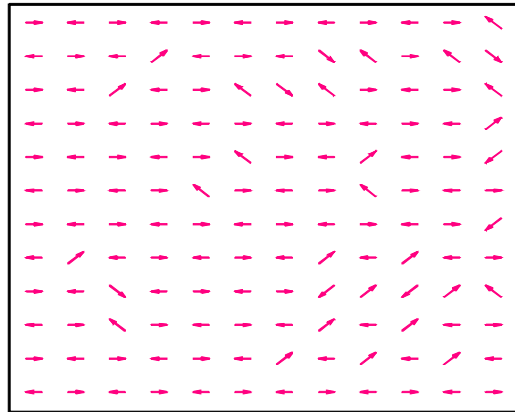
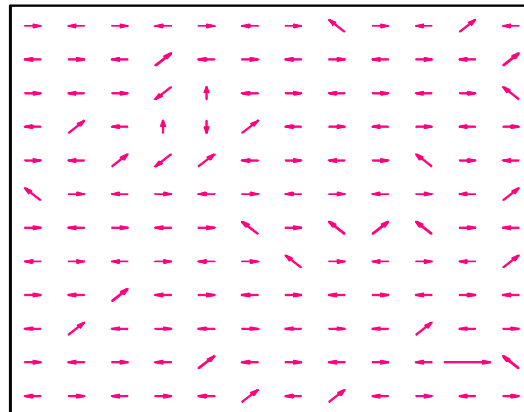


**Figure 4.2:** A plot of the total average energy  $\langle E/g \rangle$  per spin as a function of the relative magnetic surface anisotropy parameter  $\kappa/g$  at  $T/g = 2.5$  with  $h/g = 10, 20$  and  $27$ .

(a)



(b)



(c)

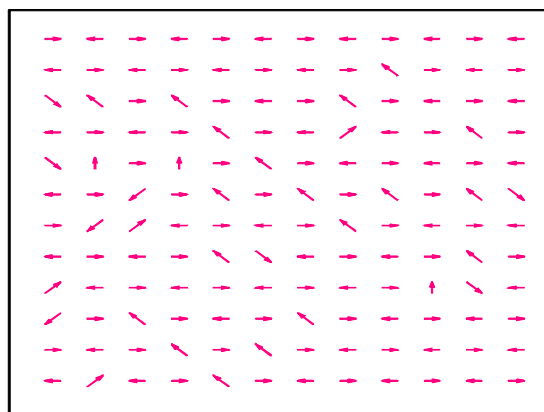


**Figure 4.3:** The snapshots of spin configurations at  $\kappa/g = -8 < \kappa_N/g$  with  $T/g = 2.5$  for (a)  $h/g = 10$  (b)  $h/g = 20$  and (c)  $h/g = 27$ .

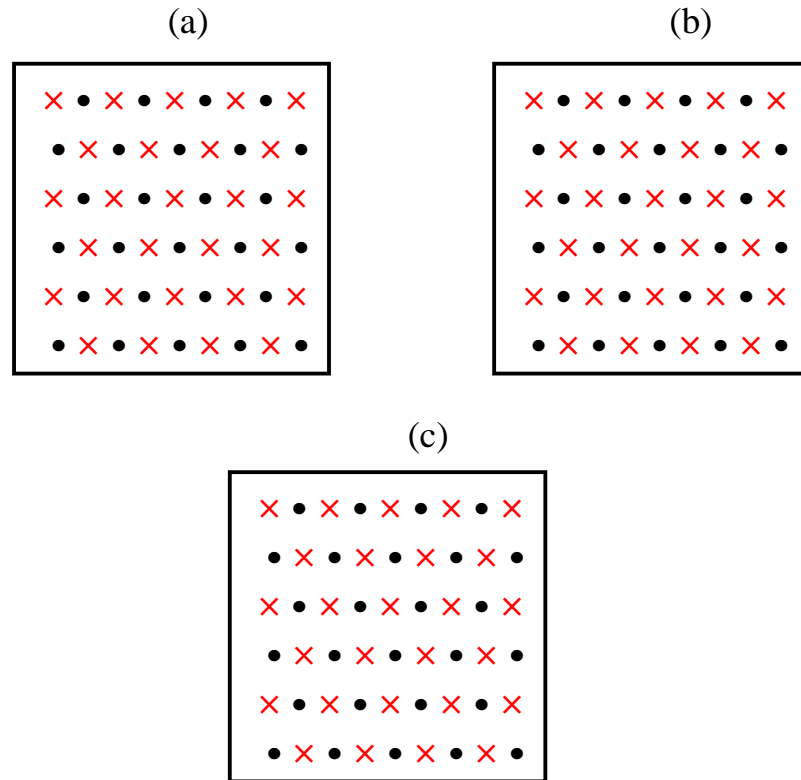


**Figure 4.4:** The snapshots of spin configurations at  $\kappa/g = 2 > \kappa_N/g$  with  $T/g = 2.5$  for a)  $h/g = 10$  (b)  $h/g = 20$  and (c)  $h/g = 27$ , where the symbol  $\times$  shows spin down while symbol  $\bullet$  shows spin up.

**Table 4.1:** The locations of the transition points between planar antiferromagnetic phase and the perpendicular antiferromagnetic phase at  $T/g = 2.5$  for  $h/g = 10, 20$  and  $27$ .

$h/g$	10	20	27
$\kappa_N/g$	$-4.057 \pm 0.025$	$-4.195 \pm 0.025$	$-4.212 \pm 0.025$

Further evidence for the discontinuous nature of the transition between the two ordered phases is clearly seen in the average dipolar energy  $\langle E_{dd}/g \rangle$  per spin ( Figures 4.5a, 4.5b and 4.5c), the average anisotropy energy  $\langle E_{\kappa}/g \rangle$  per spin (Figures 4.6a, 4.6b and 4.6c), the average exchange energy  $\langle E_{ex}/g \rangle$  per spin (Figures 4.7a, 4.7b and 4.7c) and the average Zeeman energy  $\langle E_h/g \rangle$  per spin (Figures 4.8a, 4.8b and 4.8c) with  $h/g = 10, 20$  and  $27$  at  $T/g = 2.5$  for both increasing and decreasing  $\kappa/g$ .

To show the effect of the applied magnetic field on the averages of the dipolar, anisotropy, exchange and Zeeman energies, Figures 4.9, 4.10, 4.11 and 4.12, respectively, show the  $\langle E_{dd}/g \rangle$  ,  $\langle E_{\kappa}/g \rangle$  ,  $\langle E_{ex}/g \rangle$  and  $\langle E_h/g \rangle$  as function of both increasing and decreasing  $\kappa/g$  at  $T/g = 2.5$  for  $h/g = 10, 20$  and  $27$ .

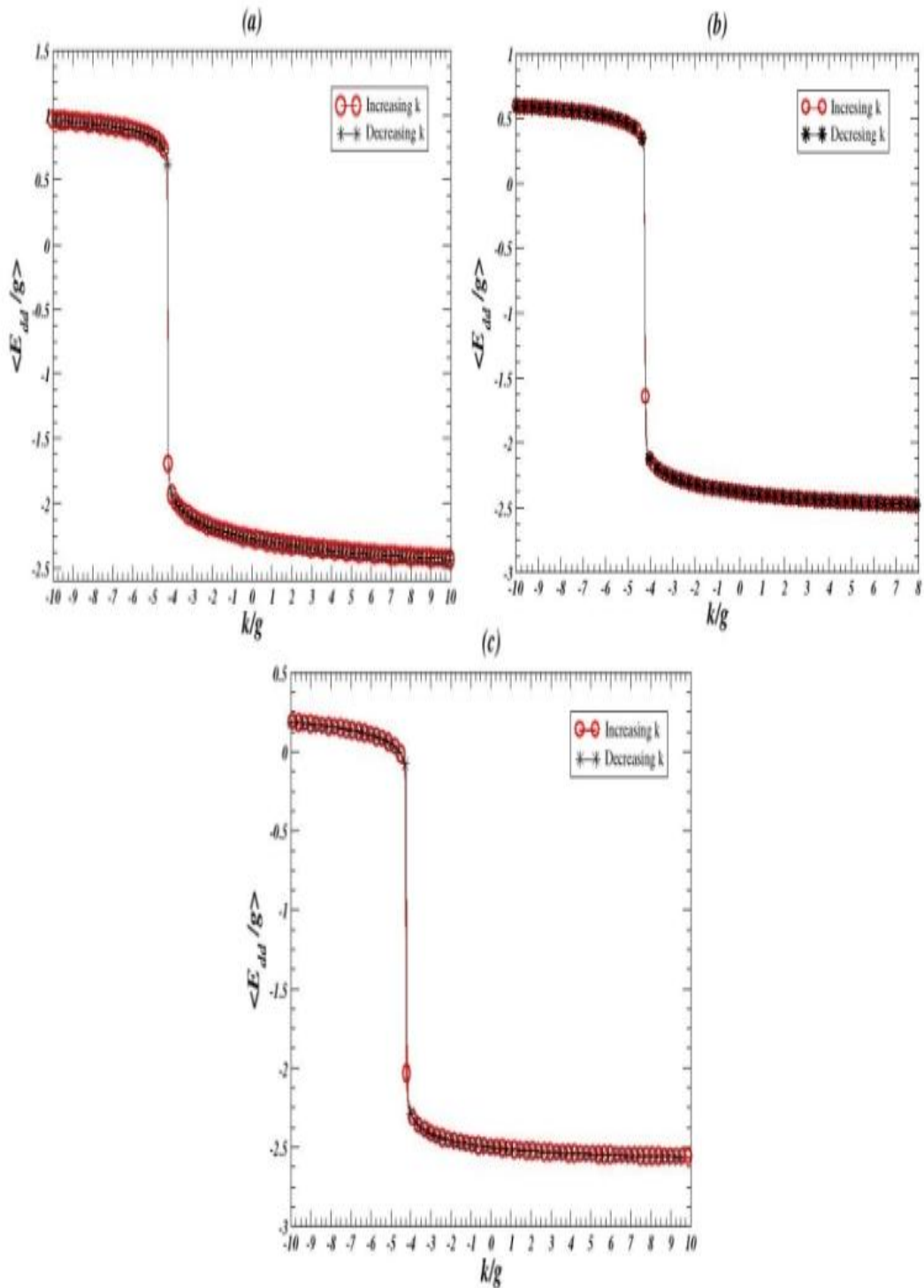


**Figure 4.5:** A plot of the average dipolar energy  $\langle E_{dd}/g \rangle$  per spin as a function of increasing and decreasing the relative magnetic surface anisotropy parameter  $\kappa/g$  at  $T/g = 2.5$  for (a)  $h/g = 10$ , (b)  $h/g = 20$  and (c)  $h/g = 27$ .

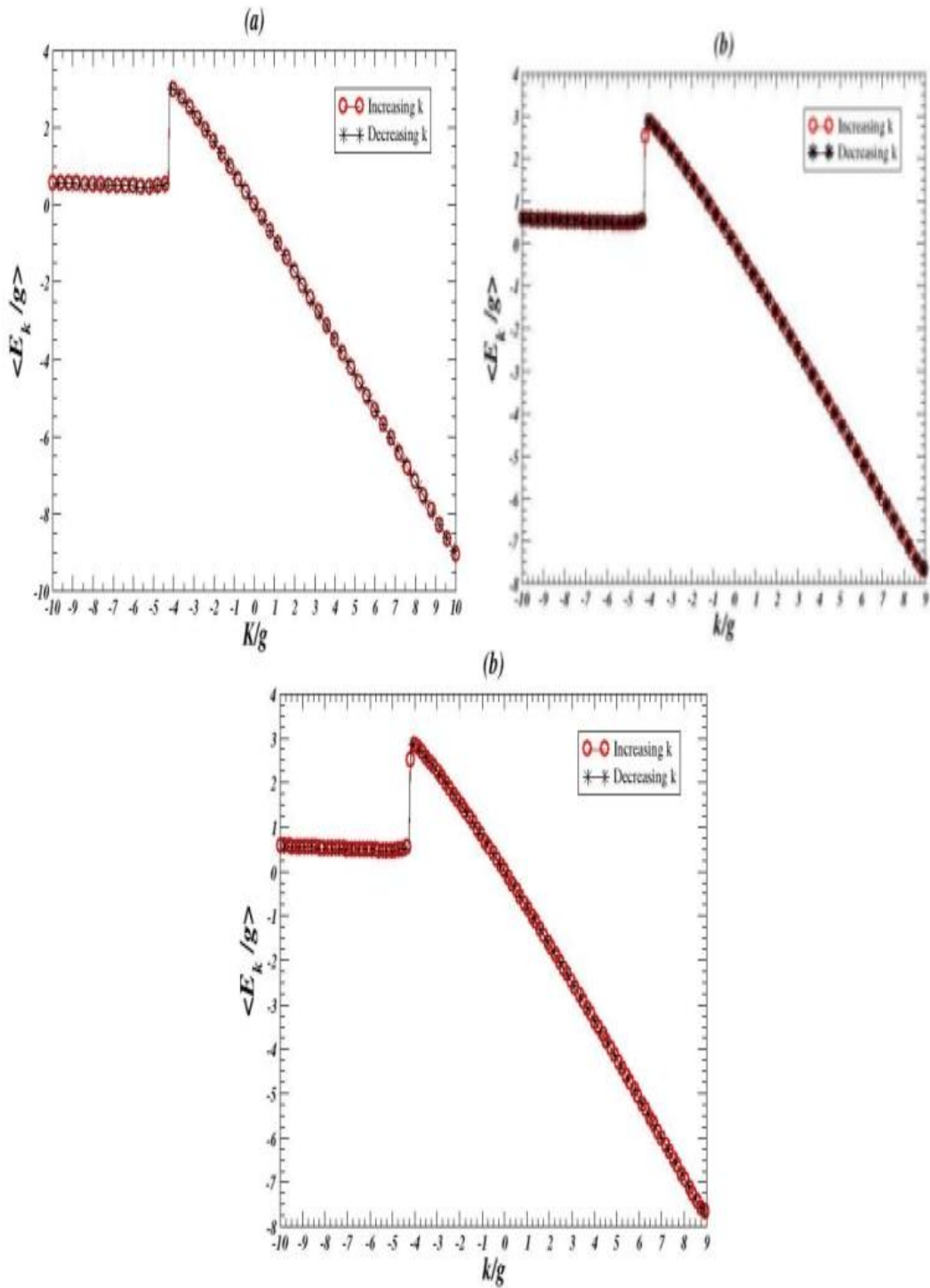


**Figure 4.6:** A plot of the average anisotropy energy  $\langle E_\kappa / g \rangle$  per spin as a function of increasing and decreasing the relative magnetic surface anisotropy parameter  $\kappa / g$  at  $T/g = 2.5$  for (a)  $h/g = 10$ , (b)  $h/g = 20$  and (c)  $h/g = 27$ .

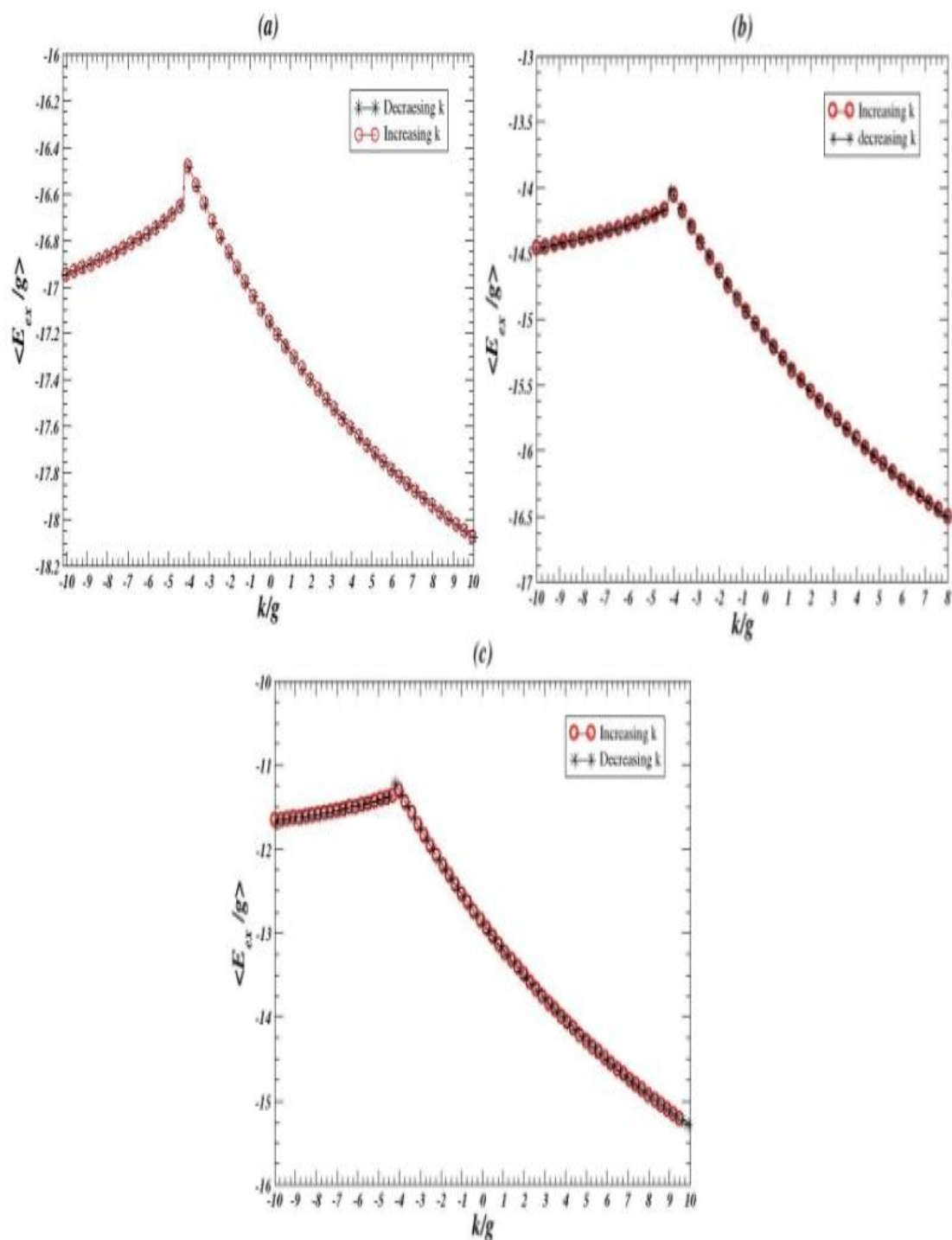


**Figure 4.7:** A plot of the average exchange energy  $\langle E_{ex}/g \rangle$  per spin as a function of increasing and decreasing the relative magnetic surface anisotropy parameter  $\kappa/g$  at  $T/g = 2.5$  for (a)  $h/g = 10$ , (b)  $h/g = 20$  and (c)  $h/g = 27$ .

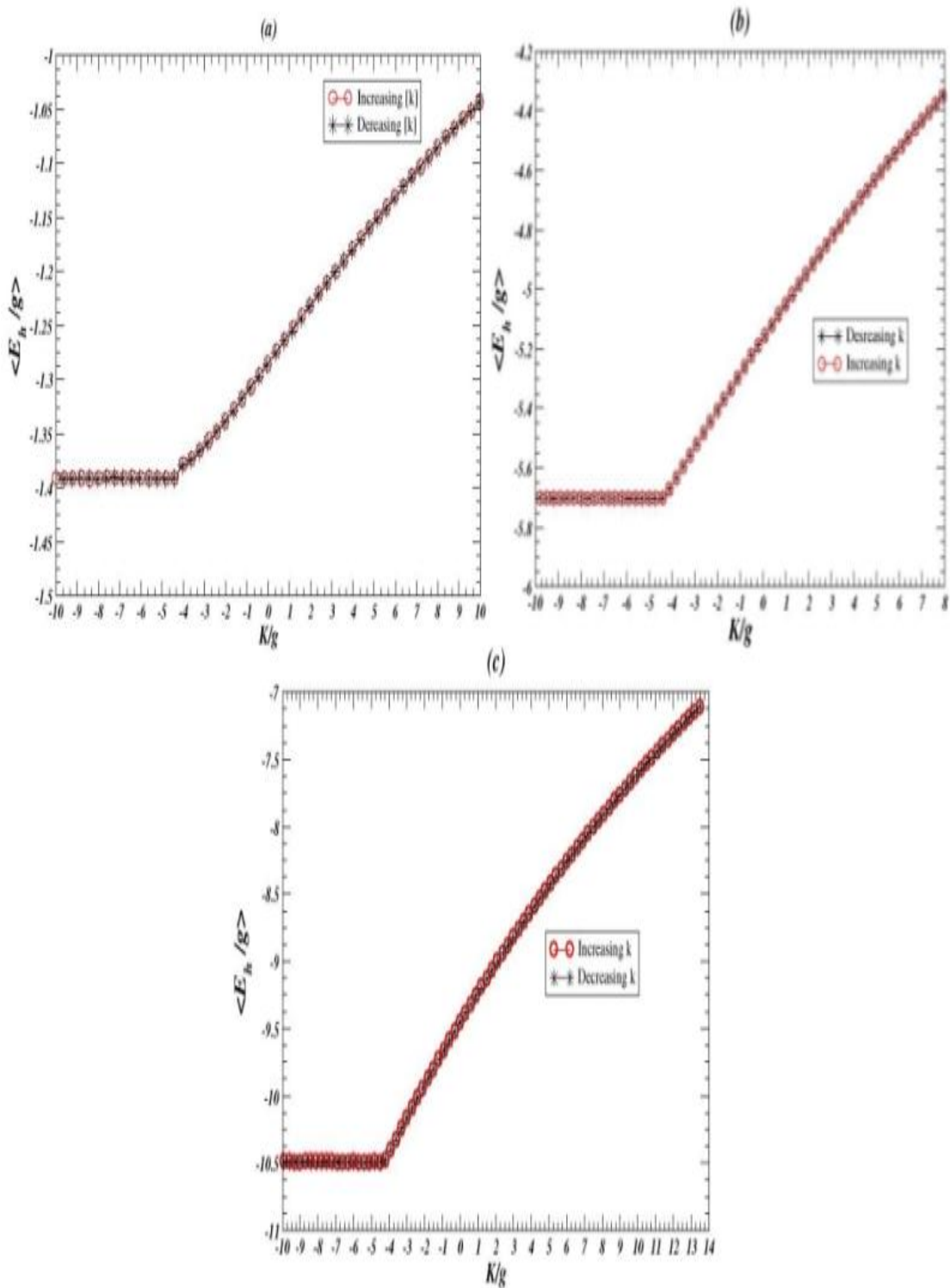


**Figure 4.8:** A plot of the average Zeeman energy  $\langle E_h/g \rangle$  per spin as a function of increasing and decreasing the relative magnetic surface anisotropy parameter  $\kappa/g$  at  $T/g = 2.5$  for (a)  $h/g = 10$ , (b)  $h/g = 20$  and (c)  $h/g = 27$ .

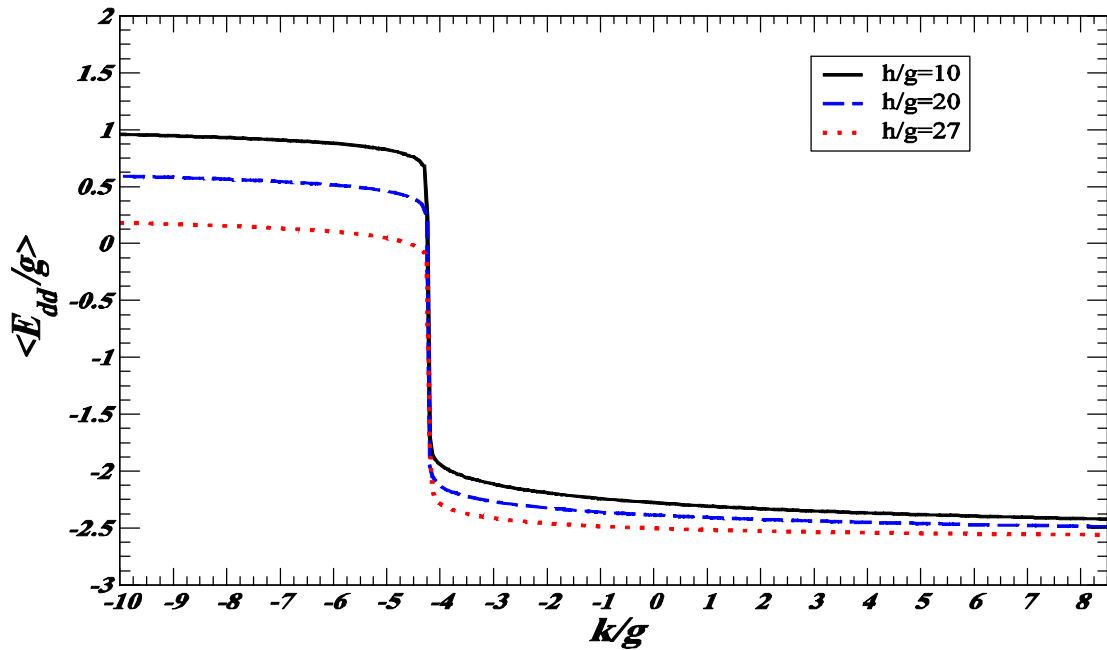


**Figure 4.9:** A plot of the average dipolar energy  $\langle E_{dd}/g \rangle$  per spin as a function of the relative magnetic surface anisotropy parameter  $\kappa/g$  at  $T/g = 2.5$  with  $h/g = 10, 20$  and  $27$ .

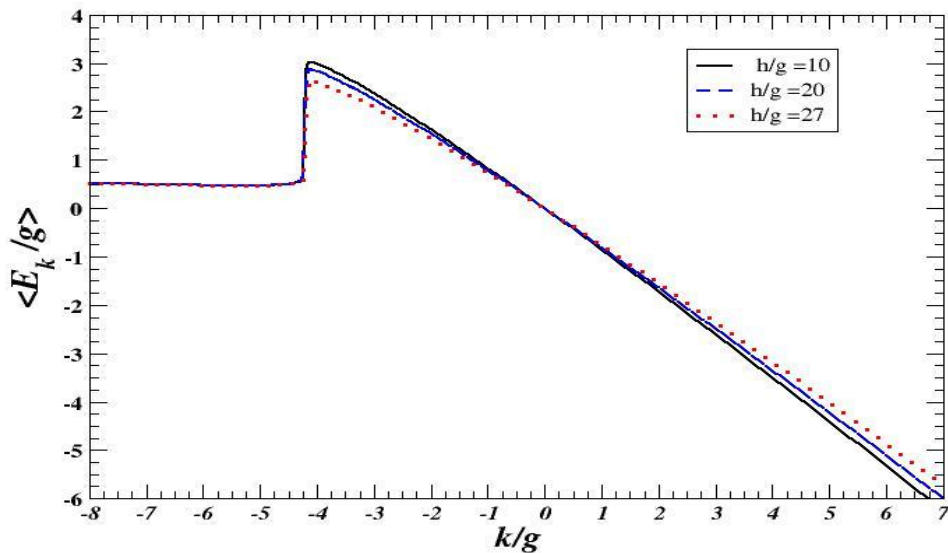


**Figure 4.10:** A plot of the average anisotropy energy  $\langle E_{\kappa}/g \rangle$  per spin as a function of the relative magnetic surface anisotropy parameter  $\kappa/g$  at  $T/g = 2.5$  with  $h/g = 10, 20$  and  $27$ .

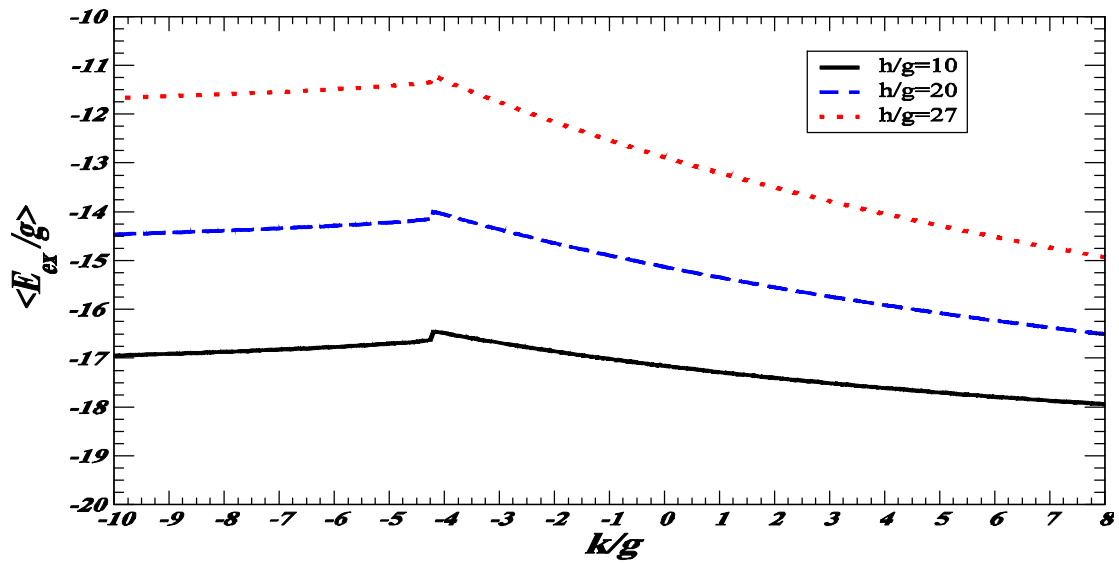


**Figure 4.11:** A plot of the average exchange energy  $\langle E_{ex}/g \rangle$  per spin as a function of the relative magnetic surface anisotropy parameter  $\kappa/g$  at  $T/g = 2.5$  with  $h/g = 10, 20$  and  $27$ .

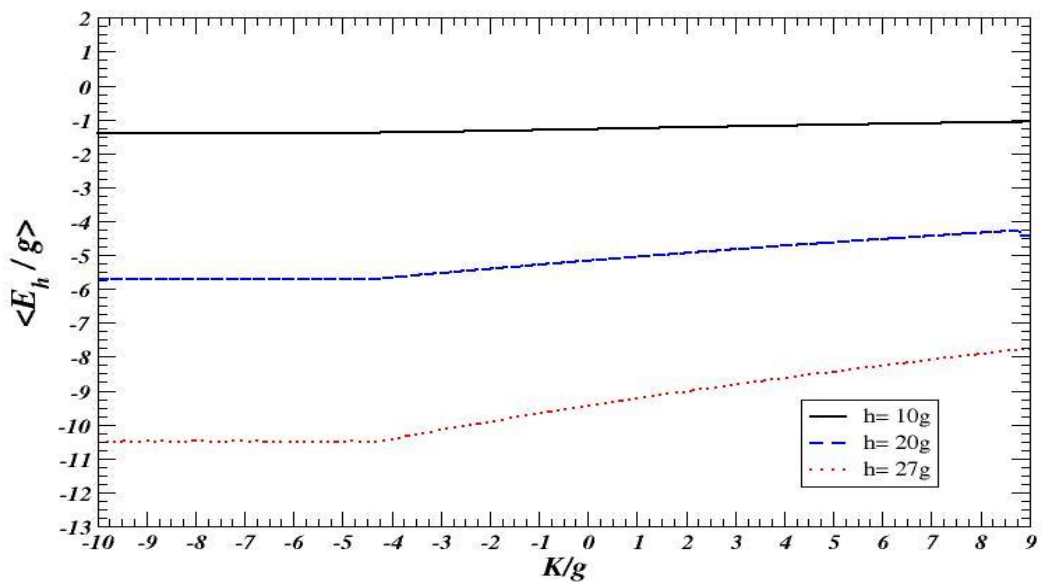


**Figure 4.12:** A plot of the average Zeeman energy  $\langle E_h/g \rangle$  per spin as a function of the relative magnetic surface anisotropy parameter  $\kappa/g$  at  $T/g = 2.5$  with  $h/g = 10, 20$  and  $27$ .

It is worth noting that Figures 4.9 and 4.12 show, respectively, a decreasing in the average dipolar and average Zeeman energies with increasing in the strength of the applied field. In contrast, Figure 4.11 show an increasing in the average exchange energy with increasing in the strength of the applied field. However, different scenario appears in the data of the average anisotropy energy shown in Figure 4.10. This Figure shows that the planar average anisotropy energy decreasing with increasing in the strength of the applied field, while the perpendicular average anisotropy energy is increasing with increasing in the strength of the applied field.

To study the effect of the applied magnetic field on the planer phase, Figures 4.13a, 4.13b and 4.13c show the total average energy  $\langle E/g \rangle$  per spin as a function of both increasing and decreasing temperature, respectively, for  $h/g = 10, 20$  and  $27$  at  $\kappa/g = -10$ . To show the effect of the applied magnetic field on the total average energy at  $\kappa/g = -10$ , Figure 4.14 shows the total average energy as a function of temperature, respectively, for  $h/g = 10, 20$  and  $27$ . The data shown in Figure 4.13 (or Figure 4.14) indicate that the curves of the system undergoes a continuous transition from the planar antiferromagnetic phase to the paramagnetic phase as the temperature increased (i.e., a planar antiferromagnetic ordered state at low temperature, a disordered state at higher temperature, and a continuous transition between them at  $T_N/g = 8.086 \pm 0.025, 7.968 \pm 0.025$  and  $7.498 \pm 0.025$  for  $h/g = 10, 20$  and  $27$ , respectively). Hence, Table 4.2 summarizes the locations of the transition points between the planer phase and disorder state at  $\kappa/g = -10$  for  $h/g = 10, 20$  and  $27$ .

The data shown in Figures 4.13 conclude that the transition from the planar antiferromagnetic phase to the paramagnetic phase is second order.

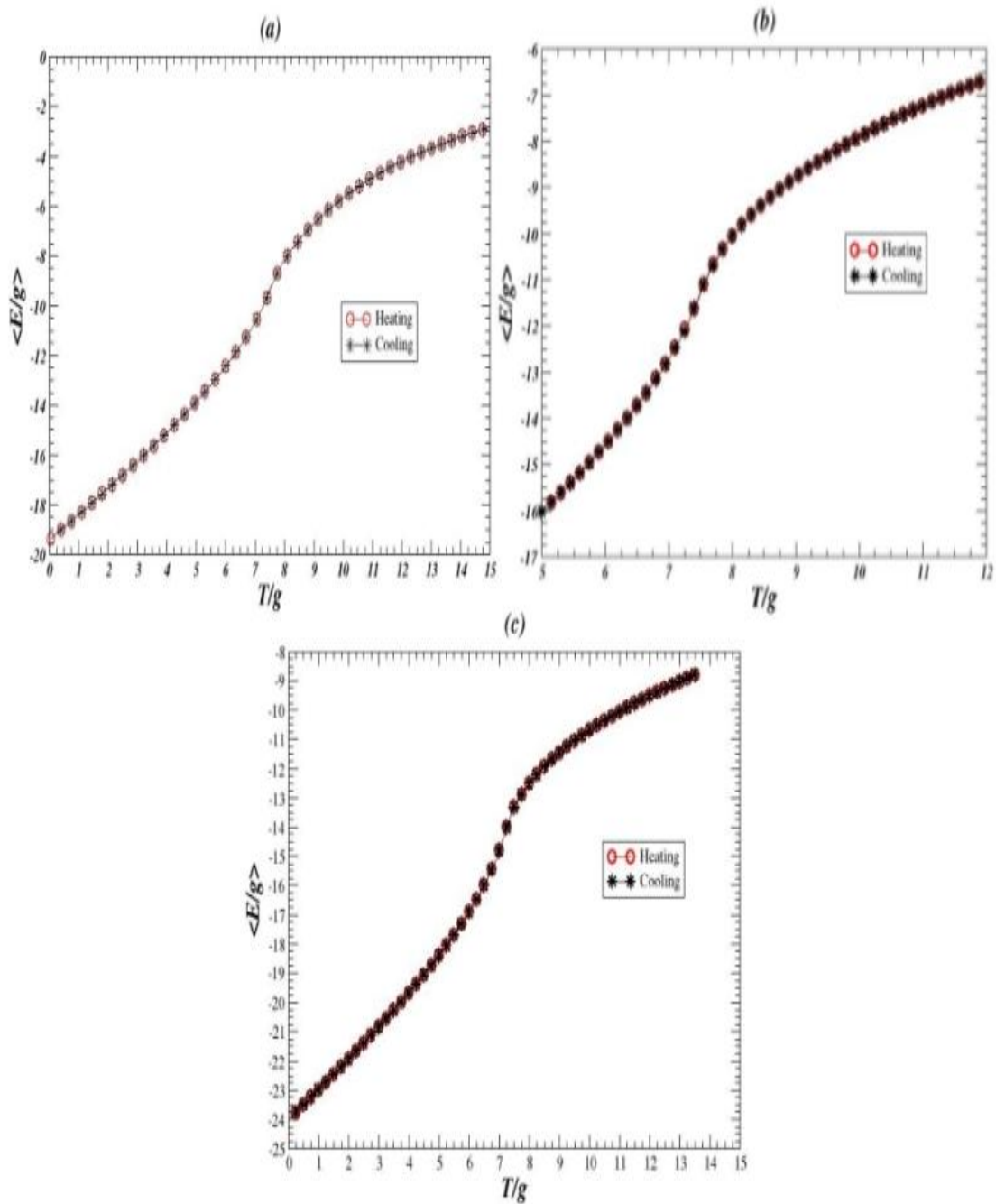


**Figure 4.13:** A plot of the total average energy  $\langle E/g \rangle$  per spin as a function of increasing and decreasing  $T/g$  at  $k/g = -10$  for (a)  $h/g = 10$ , (b)  $h/g = 20g$  and (c)  $h/g = 27$ .

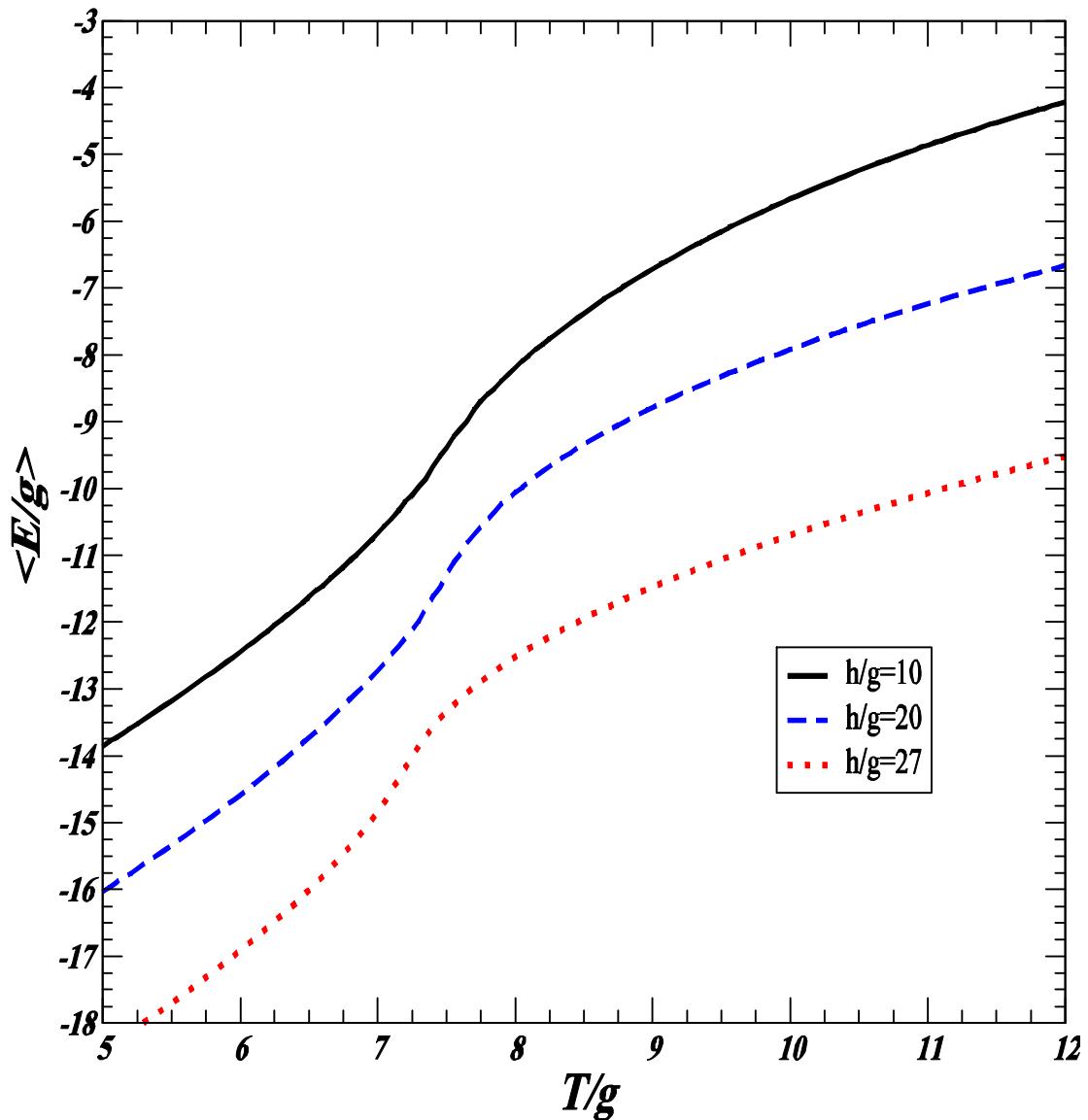


**Figure 4.14:** A plot of the total average energy  $\langle E/g \rangle$  per spin as a function of  $T/g$  at  $k/g = -10$  with  $h/g = 10, 20$  and  $27$ .

**Table 4.2:** The locations of the transition points between planar antiferromagnetic phase and the paramagnetic phase at  $\kappa/g = -10$  for  $h/g = 10, 20$  and  $27$ .

$h/g$	10	20	27
$T_N/g$	$8.086 \pm 0.025$	$7.968 \pm 0.025$	$7.498 \pm 0.025$

Further evidence for the continuous nature of the transition between planar antiferromagnetic phase and the paramagnetic phase is also seen in the average dipolar energy  $\langle E_{dd}/g \rangle$  per spin ( Figures 4.15a, 4.15b and 4.15c), the average anisotropy energy  $\langle E_{\kappa}/g \rangle$  per spin (Figures 4.16a, 4.16b and 4.16c), the average exchange energy  $\langle E_{ex}/g \rangle$  per spin (Figures 4.17a, 4.17b and 4.17c) and the average Zeeman energy  $\langle E_h/g \rangle$  per spin (Figures 4.18a, 4.18b and 4.18c) as a function of increasing and decreasing temperature  $T/g$  for  $h/g = 10, 20$  and  $27$  at  $k/g = -10$ .

To study the effect of the applied magnetic field on the average energies of the system, Figures 4.19, 4.20, 4.21 and 4.22, respectively, present the average dipolar energy  $\langle E_{dd}/g \rangle$ , the average anisotropy energy  $\langle E_{\kappa}/g \rangle$ , the average exchange energy  $\langle E_{ex}/g \rangle$  and the average Zeeman energy  $\langle E_h/g \rangle$  per spin as a function of  $T/g$  at  $\kappa/g = -10$  for  $h/g = 10, 20$  and  $27$ .

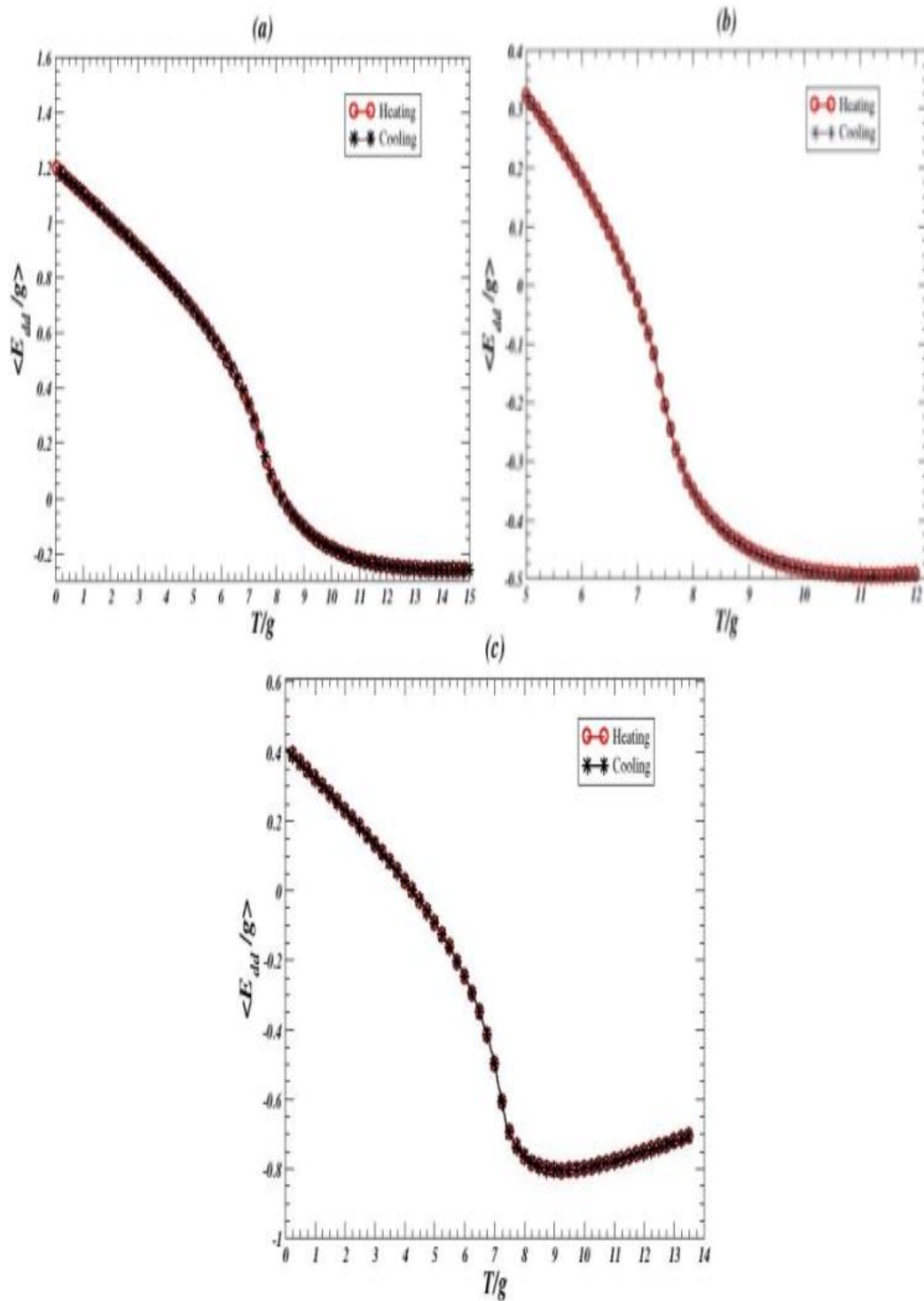


**Figure 4.15:** A plot of the average dipolar energy  $\langle E_{dd}/g \rangle$  per spin as a function of heating and cooling the system at  $k/g = -10$  for (a)  $h/g = 10$ , (b)  $h/g = 20$  and (c)  $h/g = 27$ .

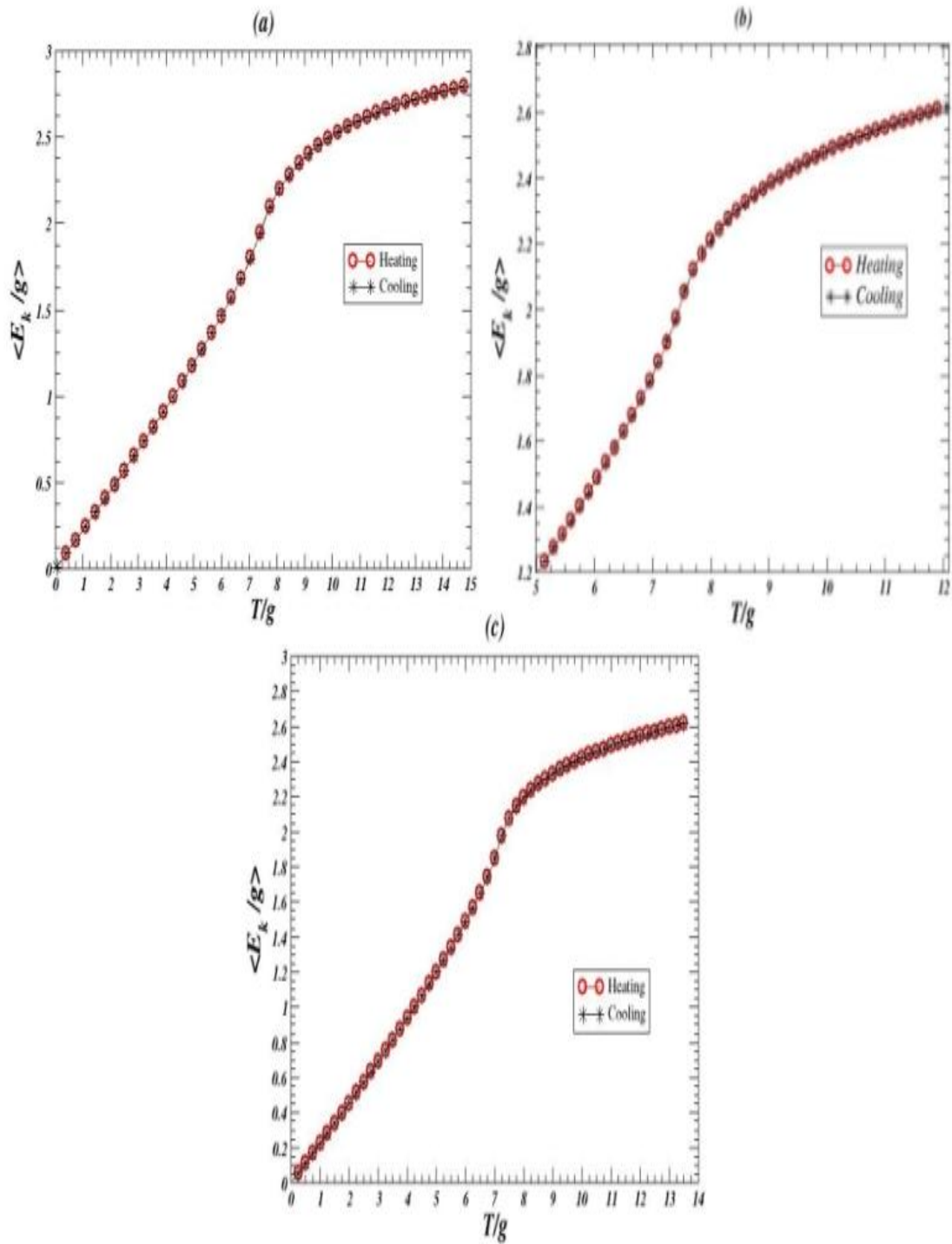


**Figure 4.16:** A plot of the average anisotropy energy  $\langle E_A/g \rangle$  per spin as a function of heating and cooling the system at  $k/g = -10$  for (a)  $h/g = 10$ , (b)  $h/g = 20$  and (c)  $h/g = 27$ .

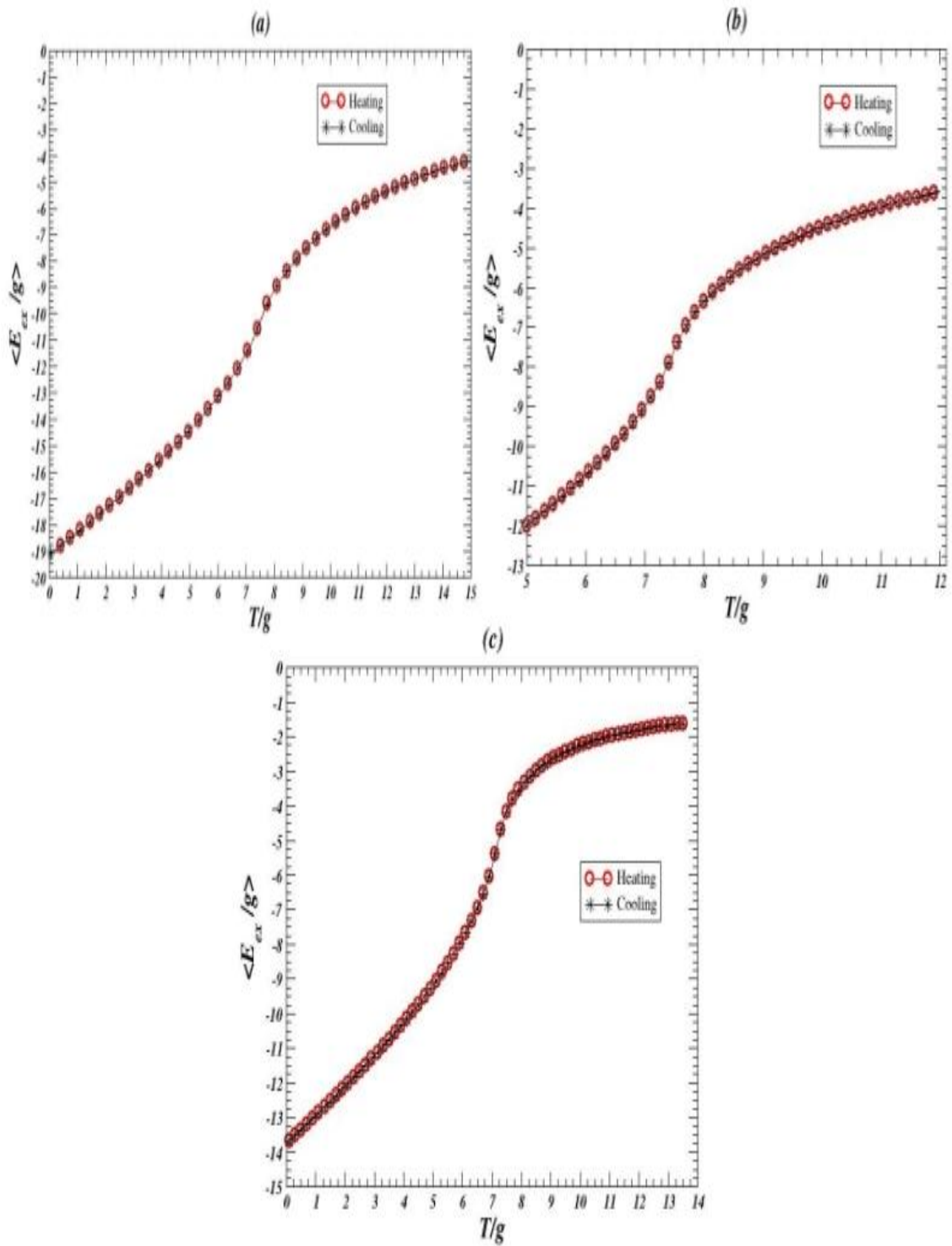


**Figure 4.17:** A plot of the average exchange energy  $\langle E_{ex}/g \rangle$  per spin as a function of heating and cooling the system at  $k/g = -10$  for (a)  $h/g = 10$ , (b)  $h/g = 20$  and (c)  $h/g = 27$ .

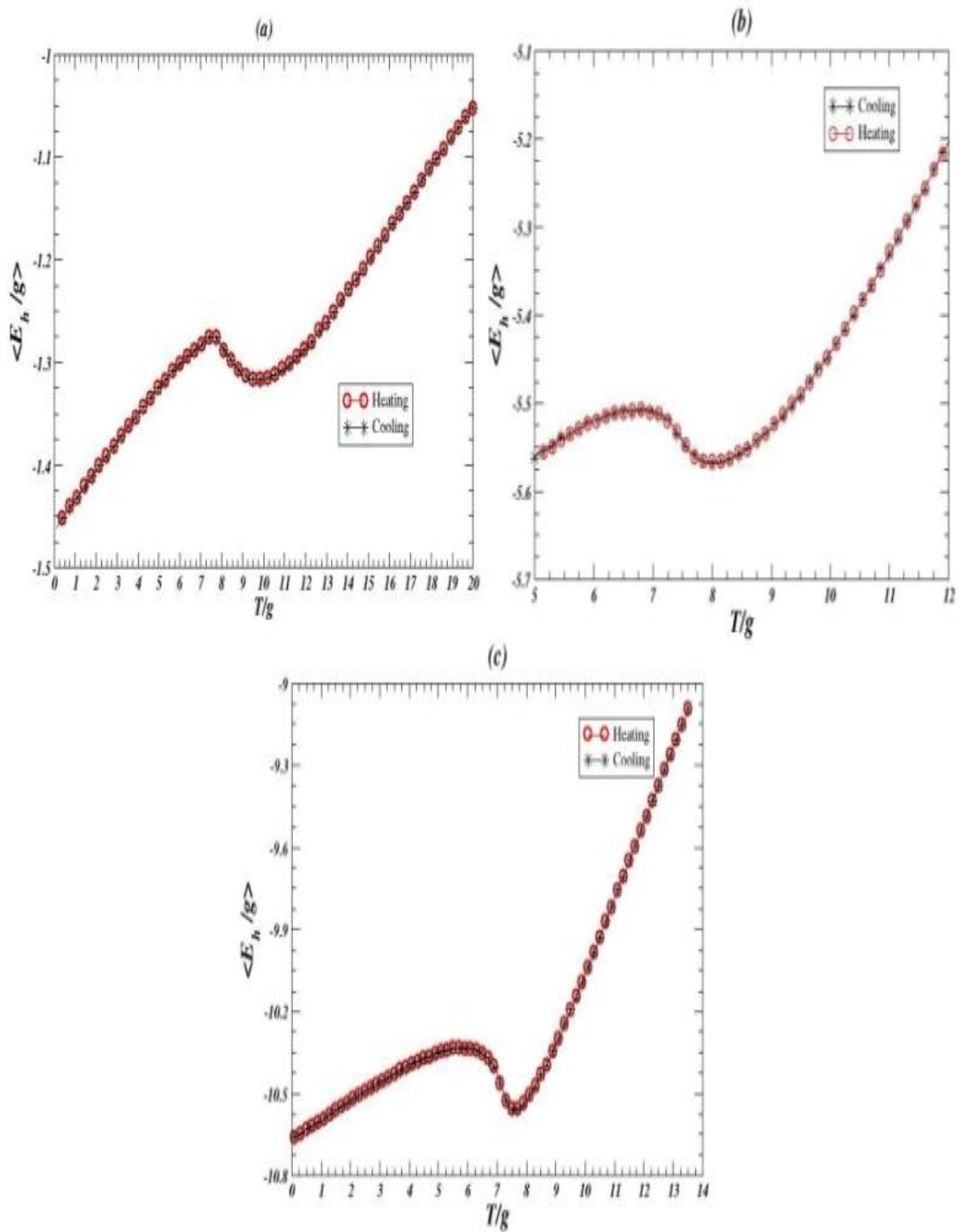


**Figure 4.18:** A plot of the average Zeeman energy  $\langle E_n/g \rangle$  per spin as a function of heating and cooling the system at  $k/g = -10$  for (a)  $h/g = 10$ , (b)  $h/g = 20$  and (c)  $h/g = 27$ .

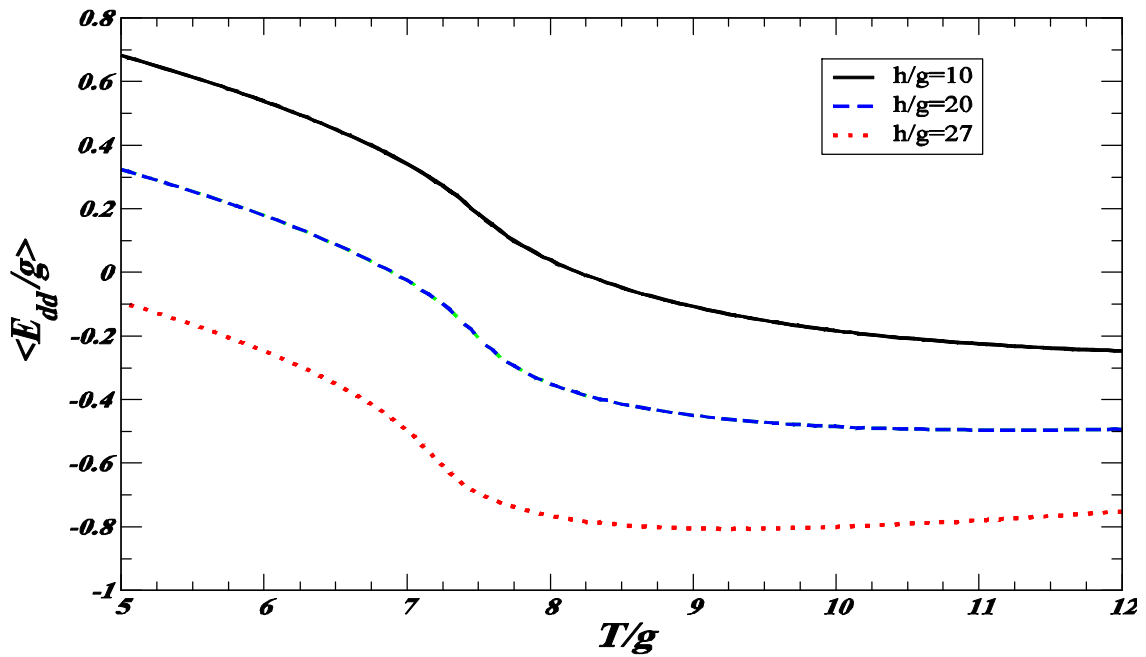


**Figure 4.19:** A plot of the average dipolar energy  $\langle E_{dd}/g \rangle$  per spin as a function of  $T/g$  at  $k/g = -10$  for  $h/g = 10, 20$  and  $27$ .

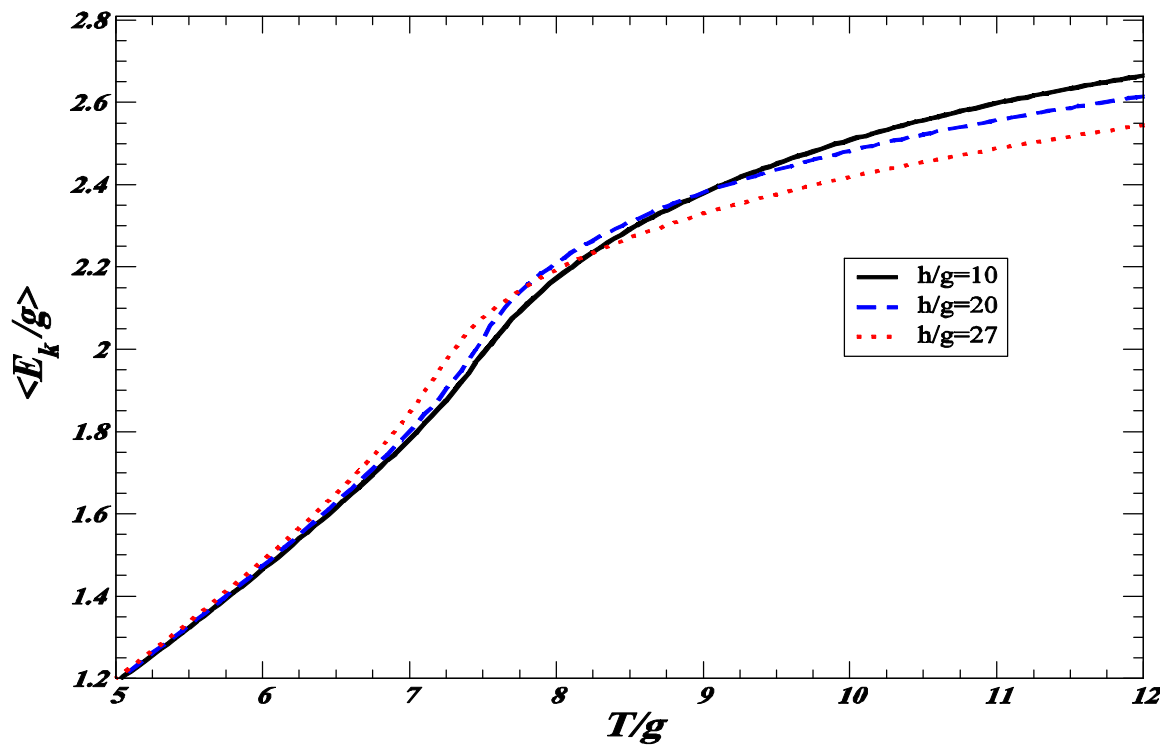


**Figure 4.20:** A plot of the average anisotropy energy  $\langle E_k/g \rangle$  per spin as a function of  $T/g$  at  $k/g = -10$  for  $h/g = 10, 20$  and  $27$ .

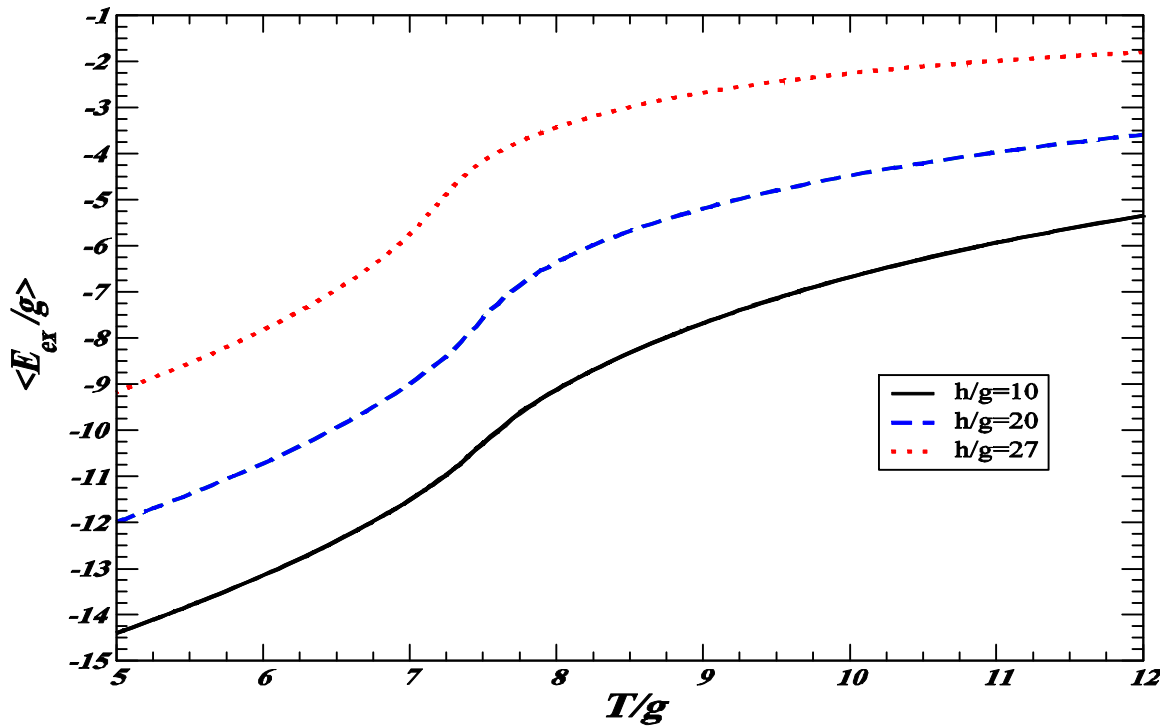


**Figure 4.21:** A plot of the average exchange energy  $\langle E_{ex}/g \rangle$  per spin as a function of  $T/g$  at  $k/g = -10$  for  $h/g = 10, 20$  and  $27$ .

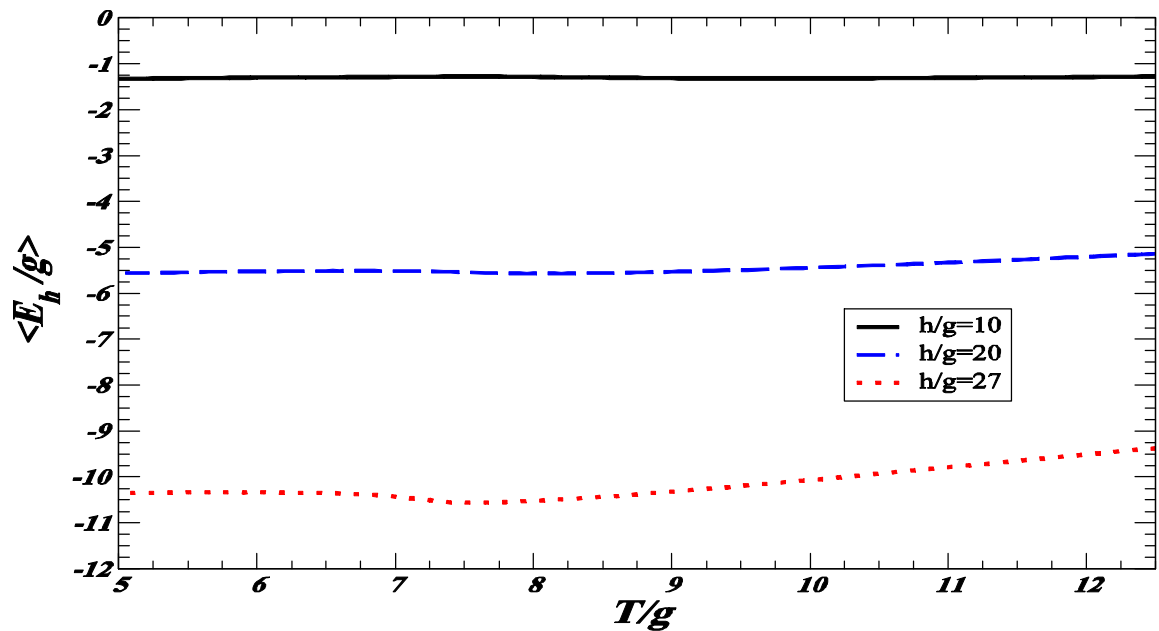


**Figure 4.22:** A plot of the average Zeeman energy  $\langle E_h/g \rangle$  per spin as a function of  $T/g$  at  $k/g = -10$  for  $h/g = 10, 20$  and  $27$ .

In the planer antiferromagnetic phase, the MC data plotted in Figures 4.19, 4.20, 4.21 and 4.22 conclude that the average dipolar and the average Zemmann energies are decreasing as the strength of the applied field is increasing; while the average exchange energy is increasing as the strength of the applied field is increasing. This behavior occurs because the angle between adjacent spins is decreasing as the applied field is increasing, this leads to increase the exchange energy and to decrease both the dipolar and zemann energies as the applied field is increasing. In addition the zemann energy is proportional to  $-\hbar$ . Hence, it is decreasing as  $h$  is increasing .

Another evidence for a second-order transition between the planar antiferromagnetic state and the disordered state is shown in Figures 4.23a, 4.23b and 4.23c, where the heat capacity  $C_H$  per spin is plotted as a function of temperature  $T/g$ , respectively, for  $h/g = 10, 20$  and  $27$  at  $k/g = 10$ . To investigate the effect of the applied magnetic field on the heat capacity, Figures 4.23a, 4.23b and 4.23c are plotted in Figure 4.24. The data plotted in Figure 4.24 shows the location of the transition point between the planer antiferromagnetic phase and paramagnetic phase shifts towards the lower temperature as the strength of the applied field is increased. In addition, Figure 4.23 (or Figure 4.24) indicates that the system undergoes a continuous transition from the planar antiferromagnetic to the paramagnetic phase as the temperature is increased.

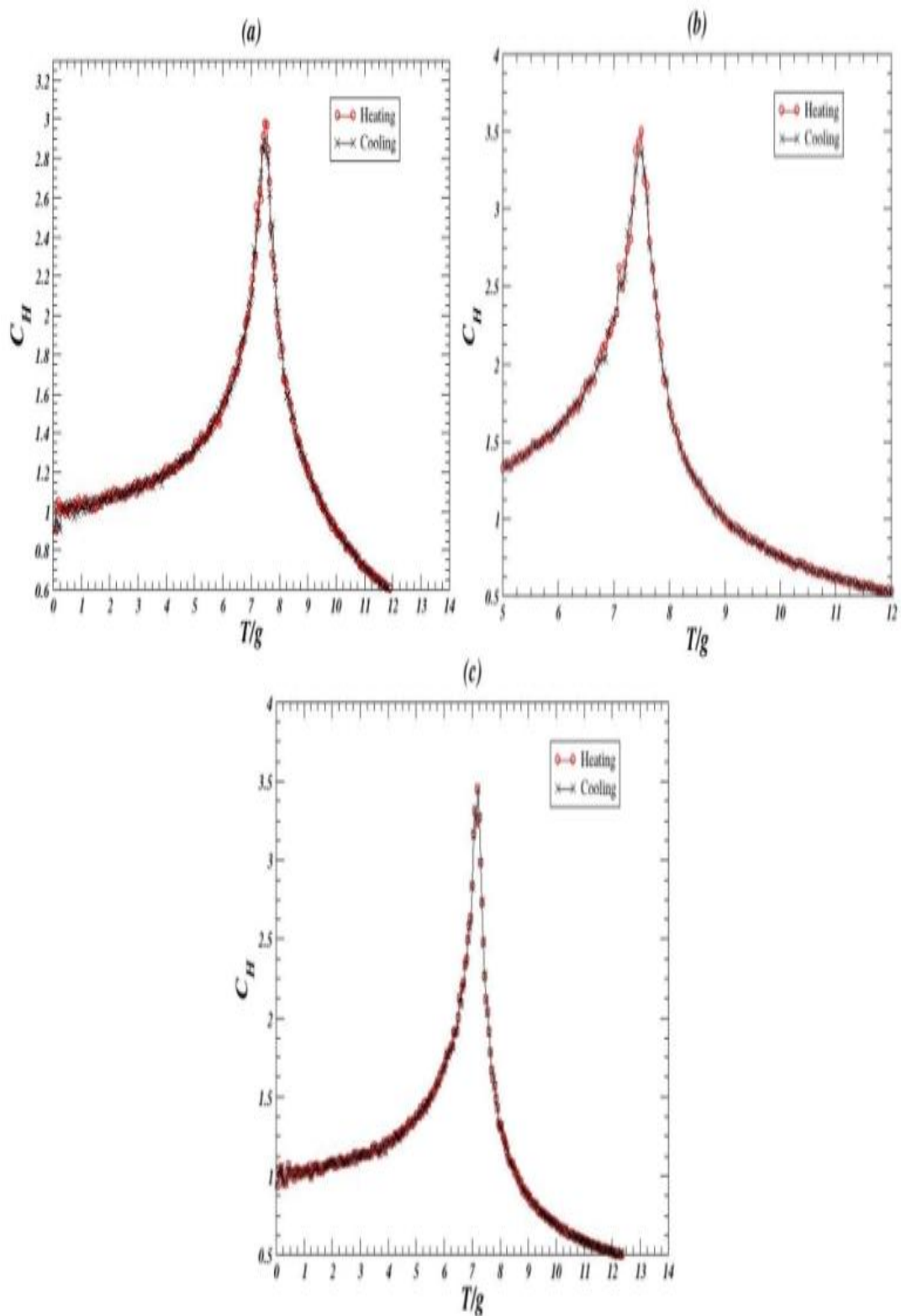


**Figure 4.23:** The specific heat  $C_H$  per spin as a function of temperature  $T/g$  at  $k/g = -10$  for (a)  $h/g = 10$ , (b)  $h/g = 20$  and (c)  $h/g = 27$ .

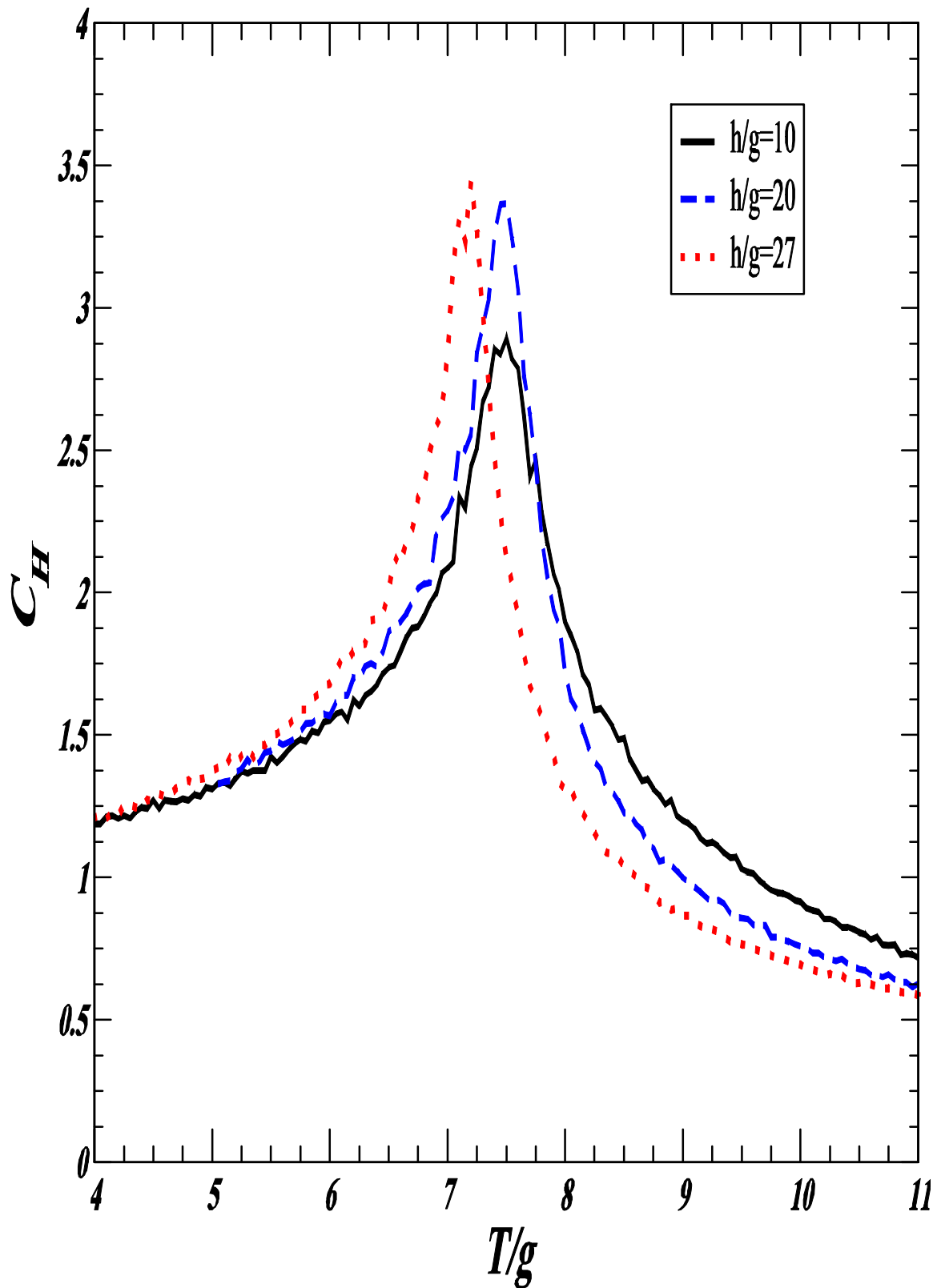


**Figure 4.24:** The specific heat  $C_H$  per spin as a function of temperature  $T/g$  at  $k/g=-10$  with  $h/g = 10, 20$  and  $27$ .

To study the effect of the applied magnetic field on the perpendicular phase, Figures 4.25a, 4.25b and 4.25c show the total average energy  $\langle E/g \rangle$  per spin as a function of both increasing and decreasing temperature, respectively, for  $h/g = 10, 20$  and  $27$  at  $\kappa/g = 2$ . To see the effect of the applied magnetic field on  $\langle E/g \rangle$  in more clear way, Figures 4.25a, 4.25b and 4.25c are plotted in Figure 4.26. In the perpendicular antiferromagnetic phase, the data shown in Figure 4.26 conclude that the  $\langle E/g \rangle$  is decreasing as the applied field is increasing. Moreover, the MC data plotted in Figure 4.25 (or Figure 4.26) include that the system undergoes a continuous transition from the perpendicular antiferromagnetic phase to the paramagnetic phase as the temperature is increased (i.e., a perpendicular antiferromagnetic ordered state at low temperature, a disordered state at higher temperature, and a continuous transition between them at  $T_N/g = 8.00 \pm 0.025, 9.99 \pm 0.025$  and  $9.26 \pm 0.025$  for  $h/g = 10, 20$  and  $27$ , respectively). Table 4.2, therefore, summarizes the locations of the transition points between the perpendicular phase and the disorder state at  $\kappa/g = 2$  for  $h/g = 10, 20$  and  $27$ .

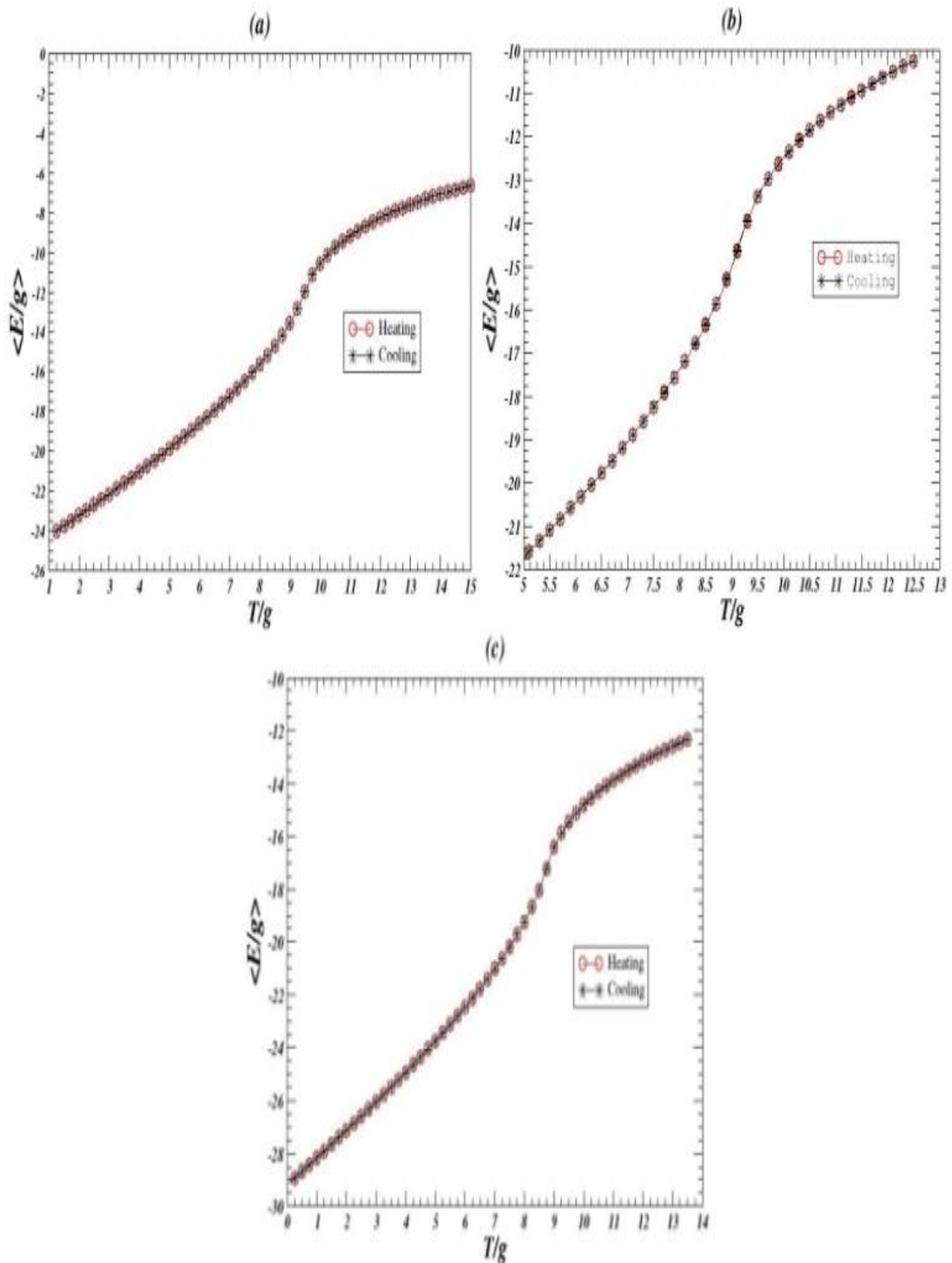


**Figure 4.25:** A plot of the total average energy  $\langle E/g \rangle$  per spin as a function of heating and cooling the system at  $k/g = 2$  for (a)  $h/g = 10$ , (b)  $h/g = 20$  and (c)  $h/g = 27$ .

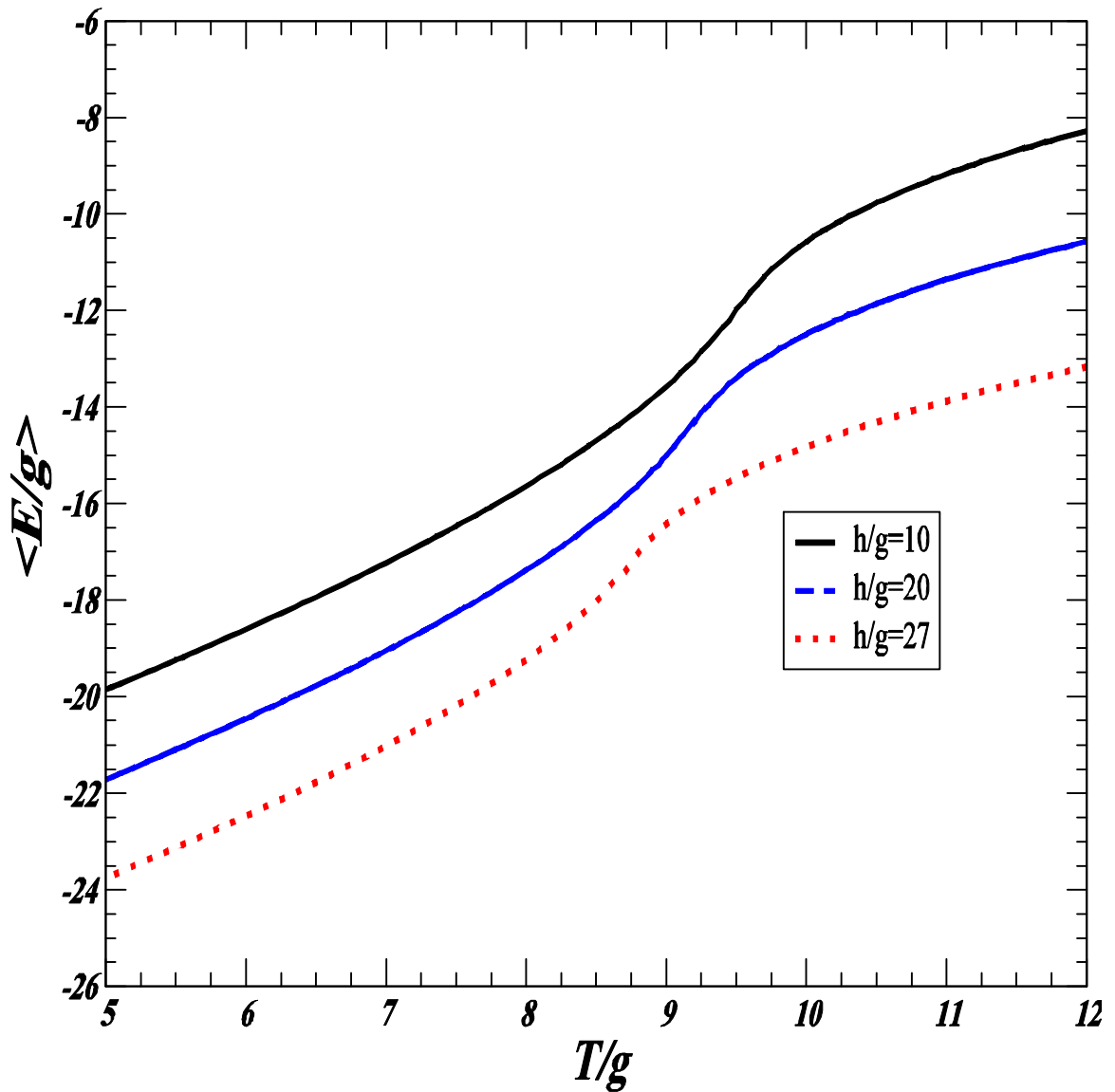


**Figure 4.26:** A plot of the total average energy  $\langle E/g \rangle$  per spin as a function of  $T/g$  at  $k/g = 2$  with  $h/g = 10, 20$  and  $27$ .

**Table 4.3:** The locations of the transition points between perpendicular antiferromagnetic phase and the paramagnetic phase at  $\kappa/g = 2$  for  $h/g = 10, 20$  and  $27$ .

$h/g$	10	20	27
$T_N/g$	$8.00 \pm 0.025$	$9.99 \pm 0.025$	$9.26 \pm 0.025$

Further evidence for the second order transition between perpendicular antiferromagnetic phase and the paramagnetic phase is clearly seen in the average dipolar energy  $\langle E_{dd}/g \rangle$  per spin (Figures 4.27a, 4.27b and 4.27c), the average anisotropy energy  $\langle E_{\kappa}/g \rangle$  per spin (Figures 4.28a, 4.28b and 4.28c), the average exchange energy  $\langle E_{ex}/g \rangle$  per spin (Figures 4.29a, 4.29b and 4.29c) and the average Zeeman energy  $\langle E_h/g \rangle$  per spin (Figures 4.30a, 4.30b and 4.30c) as a function of temperature  $T/g$  for  $h/g = 10, 20$  and  $27$  at  $k/g = 2$ .

To study the effect of the applied magnetic field on the average energies of the system, Figures 4.31, 4.32, 4.33 and 4.34, respectively, present  $\langle E_{dd}/g \rangle$ ,  $\langle E_{\kappa}/g \rangle$ ,  $\langle E_{ex}/g \rangle$  and  $\langle E_h/g \rangle$  per spin for  $h/g = 10, 20$  and  $27$  as a function of temperature  $T/g$  at  $\kappa/g = 2$ .

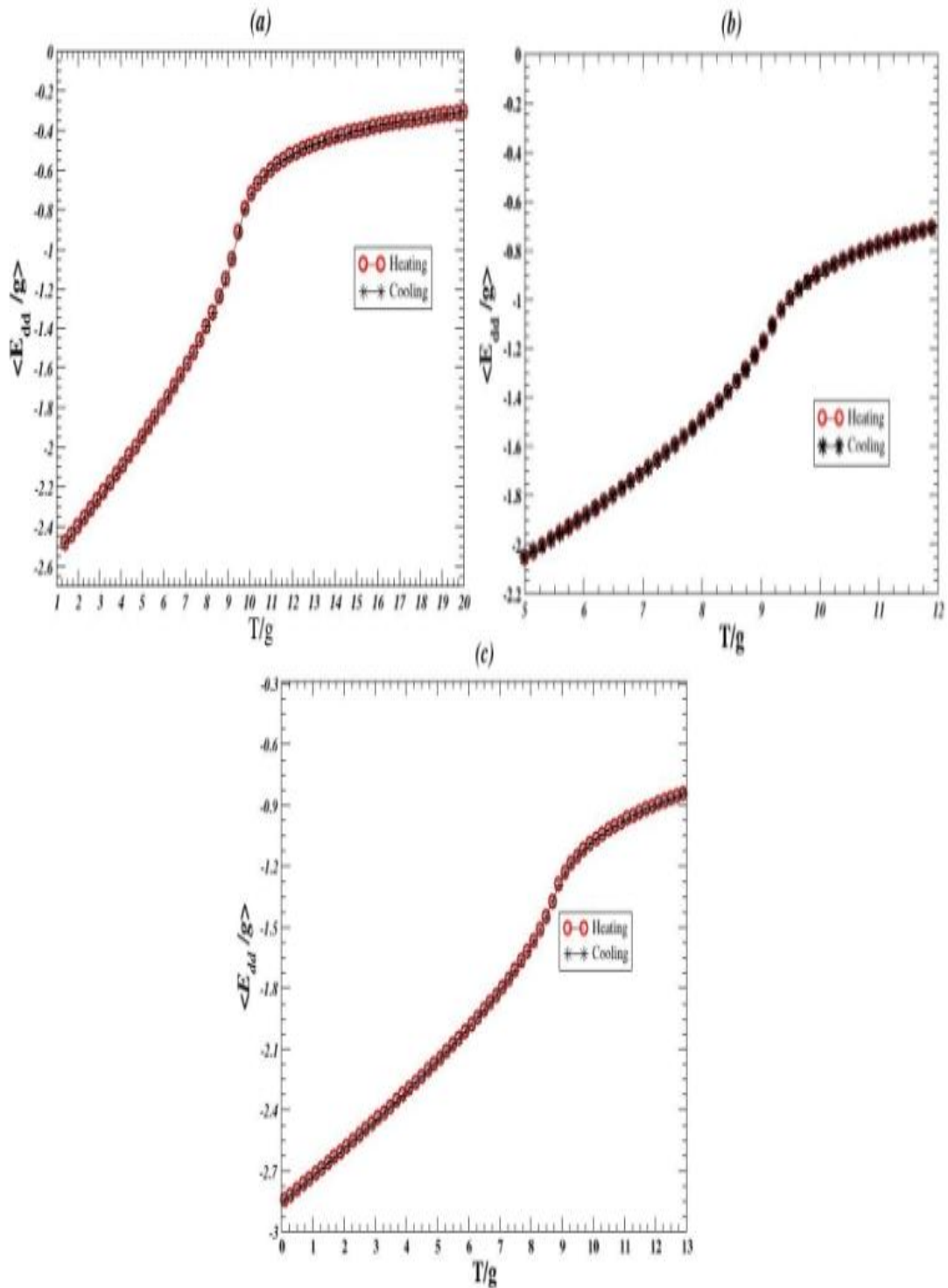


**Figure 4.27:** A plot of the average dipolar energy  $\langle E_{dd}/g \rangle$  per spin as a function of heating and cooling the system at  $k/g = 2$  for (a)  $h/g = 10$ , (b)  $h/g = 20$  and (c)  $h/g = 27$ .

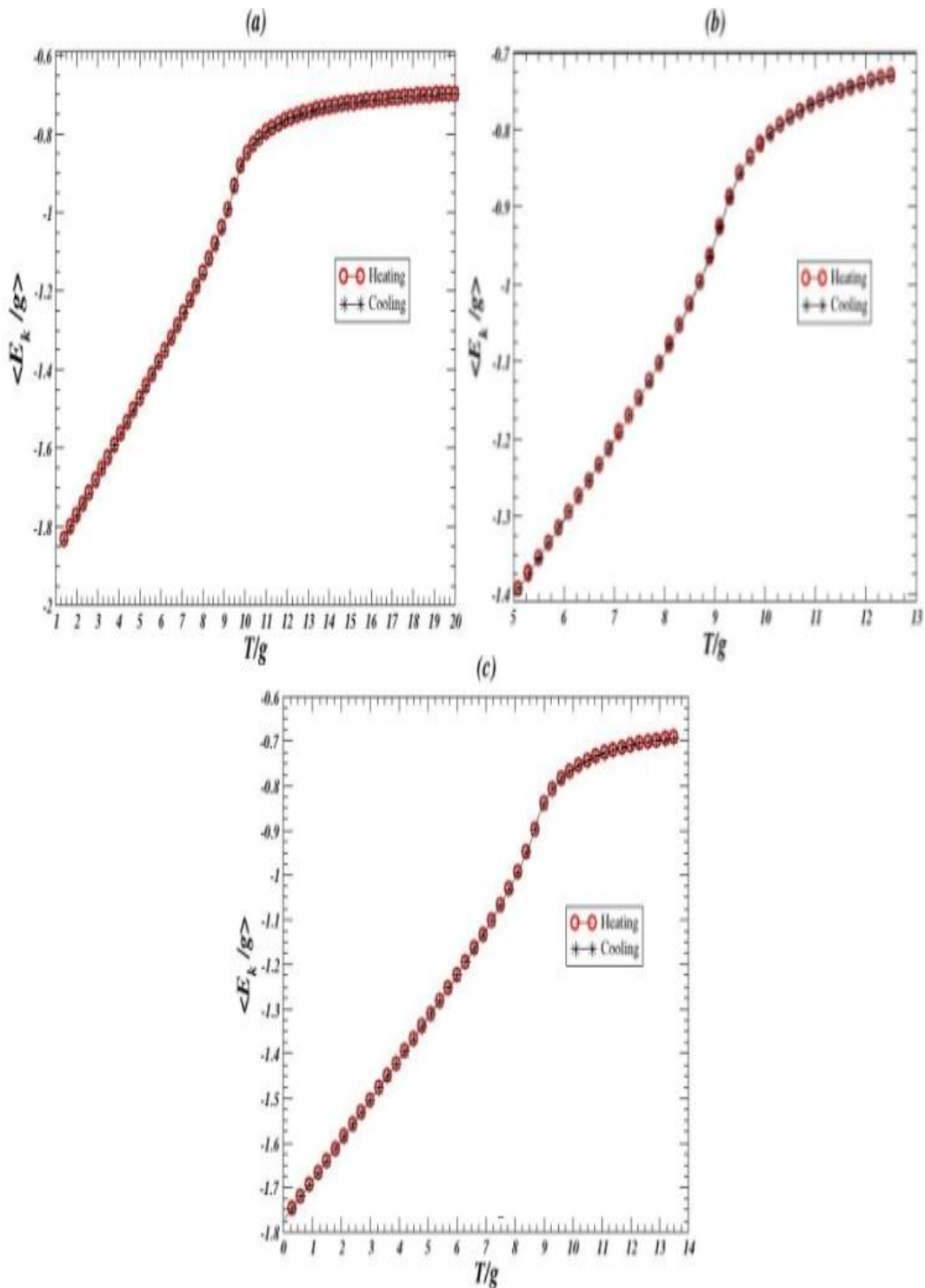


**Figure 4.28:** A plot of the average anisotropy energy  $\langle E_k/g \rangle$  per spin as a function of heating and cooling the system at  $k/g = 2$  for (a)  $h/g = 10$ , (b)  $h/g = 20$  and (c)  $h/g = 27$ .

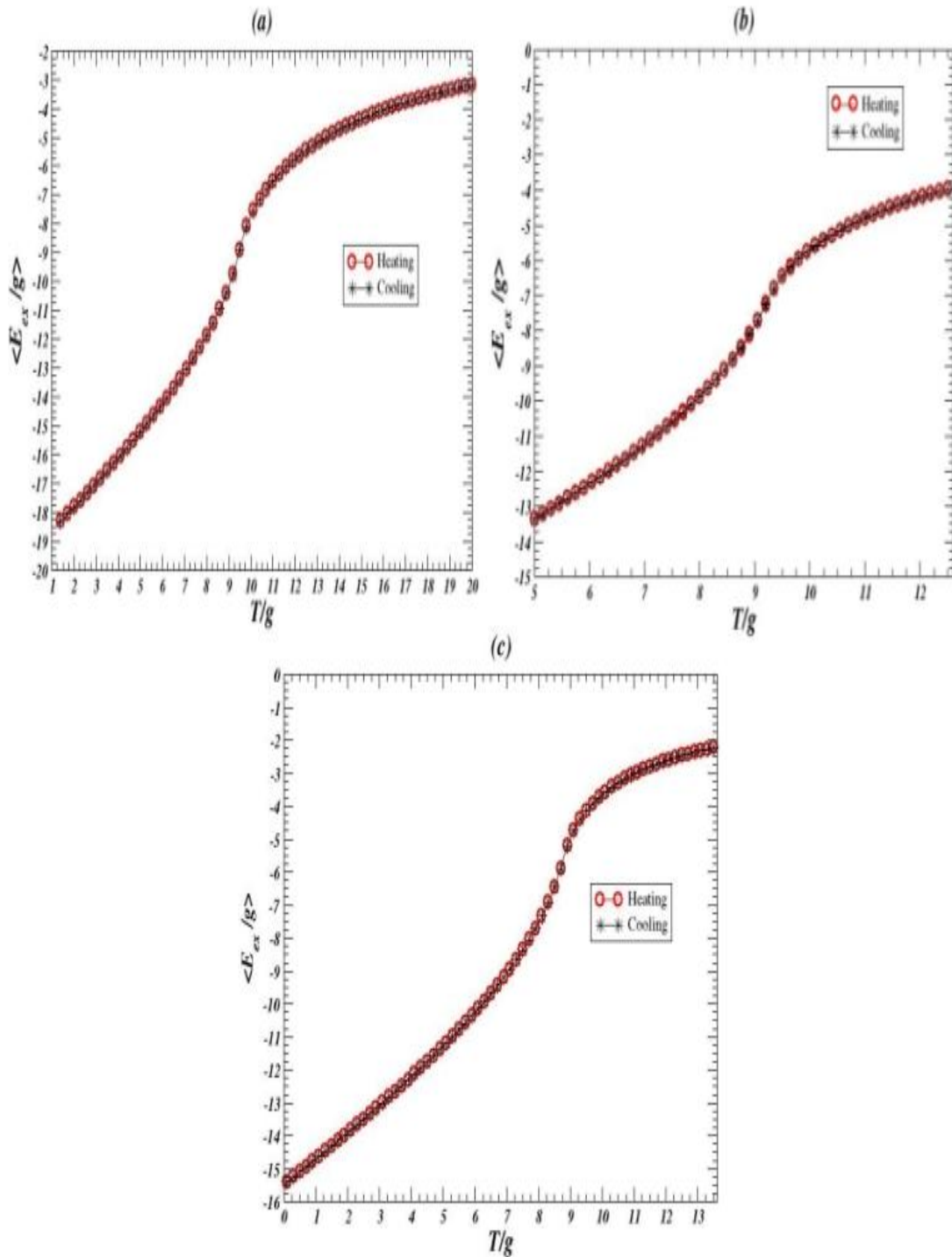


**Figure 4.29:** A plot of the average exchange energy  $\langle E_{ex}/g \rangle$  as a function of heating and cooling the system at  $k/g = 2$  for (a)  $h/g = 10$ , (b)  $h/g = 20$  and (c)  $h/g = 27$ .

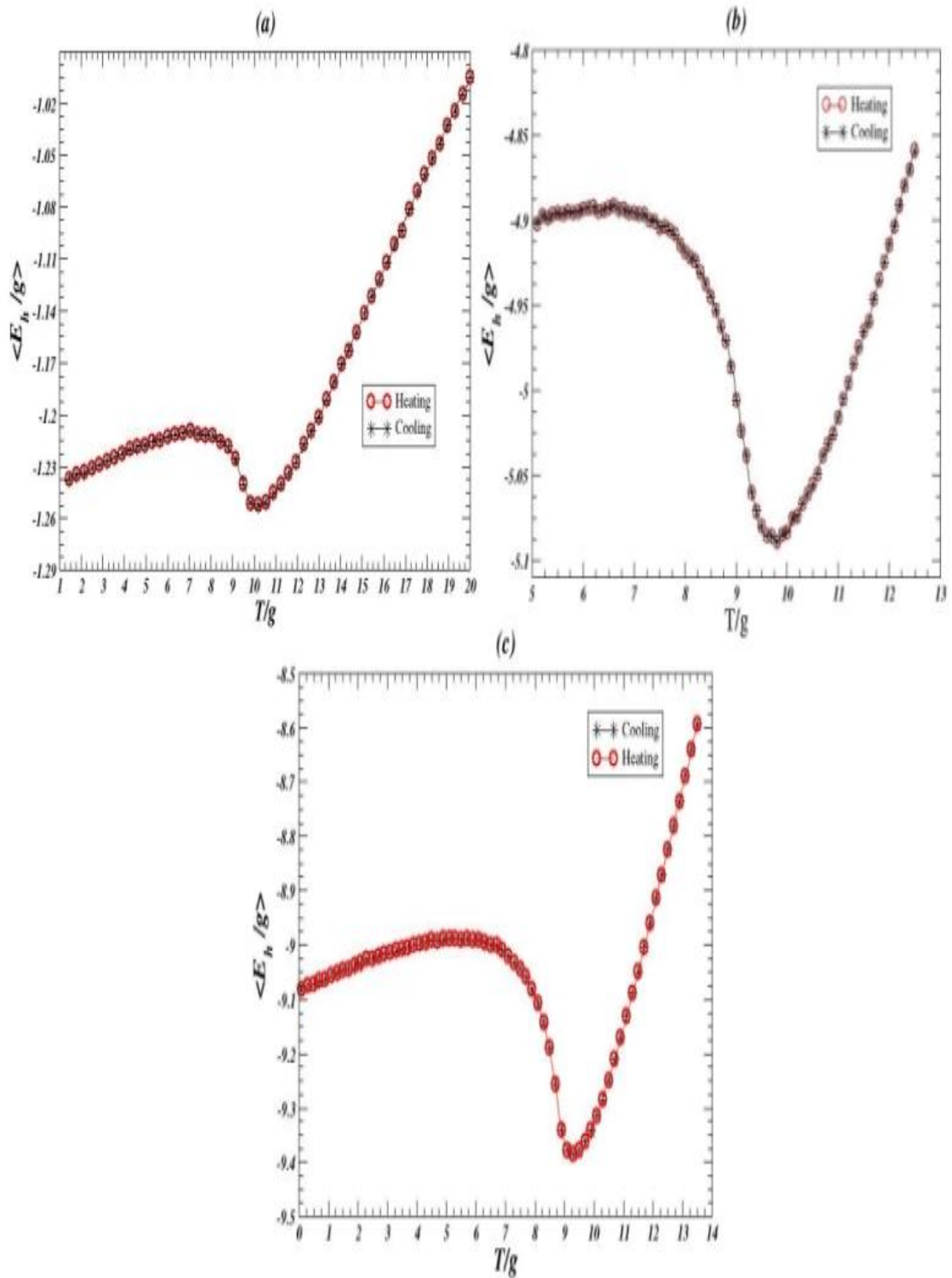


**Figure 4.30:** A plot of the average Zemann energy  $\langle E_h/g \rangle$  as a function of heating and cooling the system at  $k/g = 2$  for (a)  $h/g = 10$ , (b)  $h/g = 20$  and (c)  $h/g = 27$ .

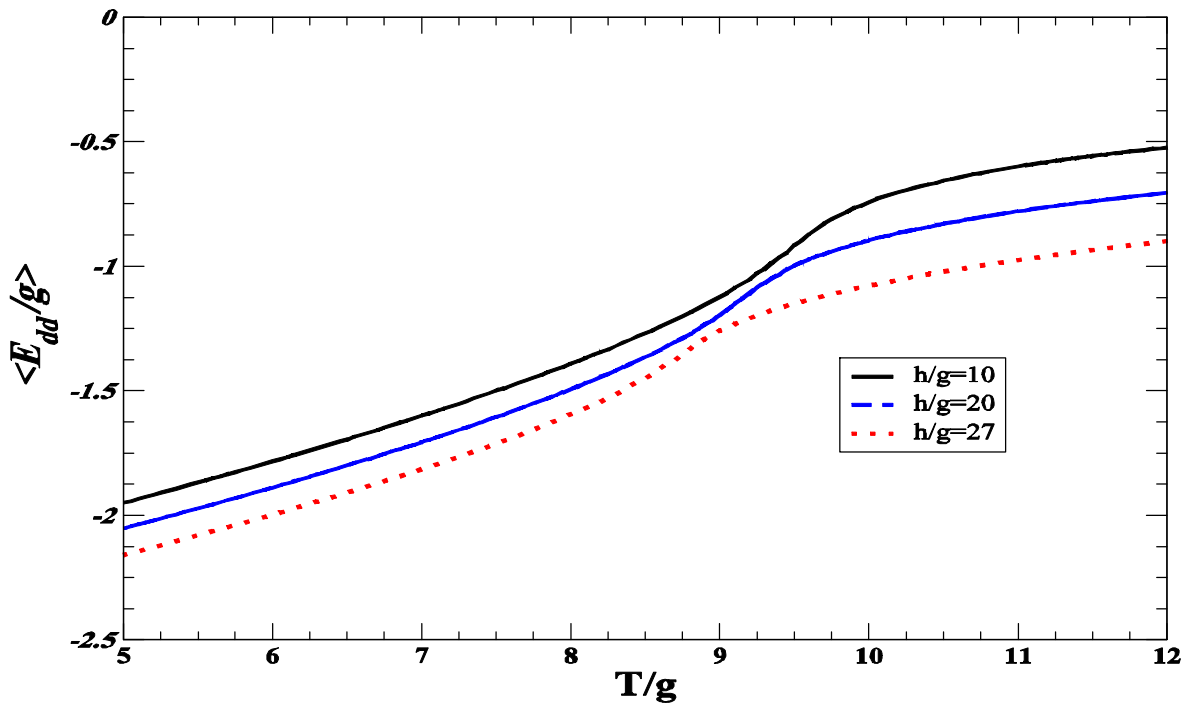


**Figure 4.31:** A plot of the average dipolar energy  $\langle E_{dd}/g \rangle$  per spin as a function of  $T/g$  at  $k/g = 2$  for  $h/g = 10, 20$  and  $27$ .

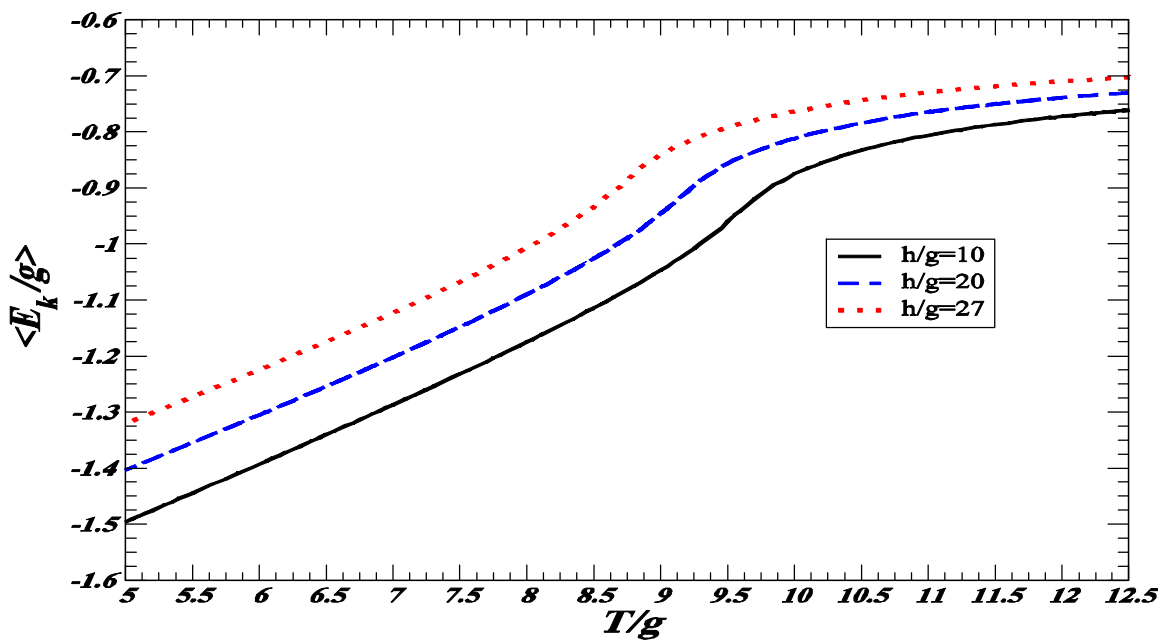


**Figure 4.32:** A plot of the average anisotropy energy  $\langle E_k/g \rangle$  per spin as a function of  $T/g$  at  $k/g = 2$  for  $h/g = 10, 20$  and  $27$ .

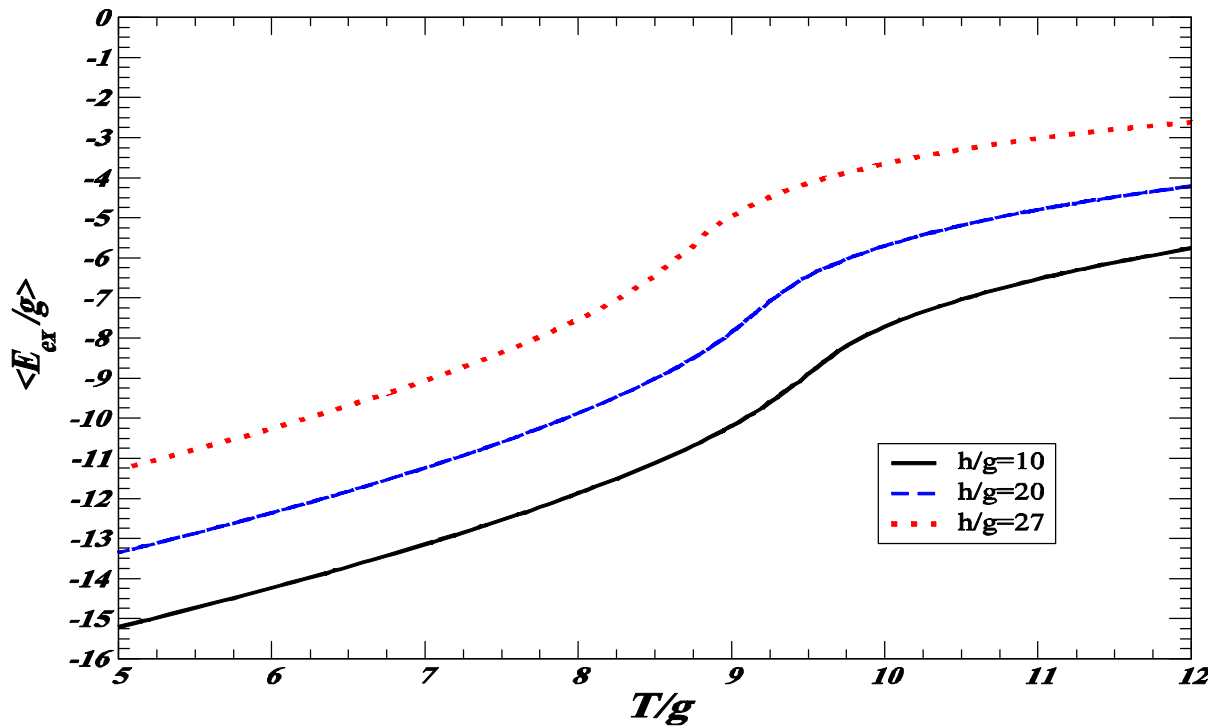


**Figure 4.33:** A plot of the average exchange energy  $\langle E_{\text{ex}}/g \rangle$  per spin as a function of  $T/g$  at  $k/g = 2$  for  $h/g = 10, 20$  and  $27$ .

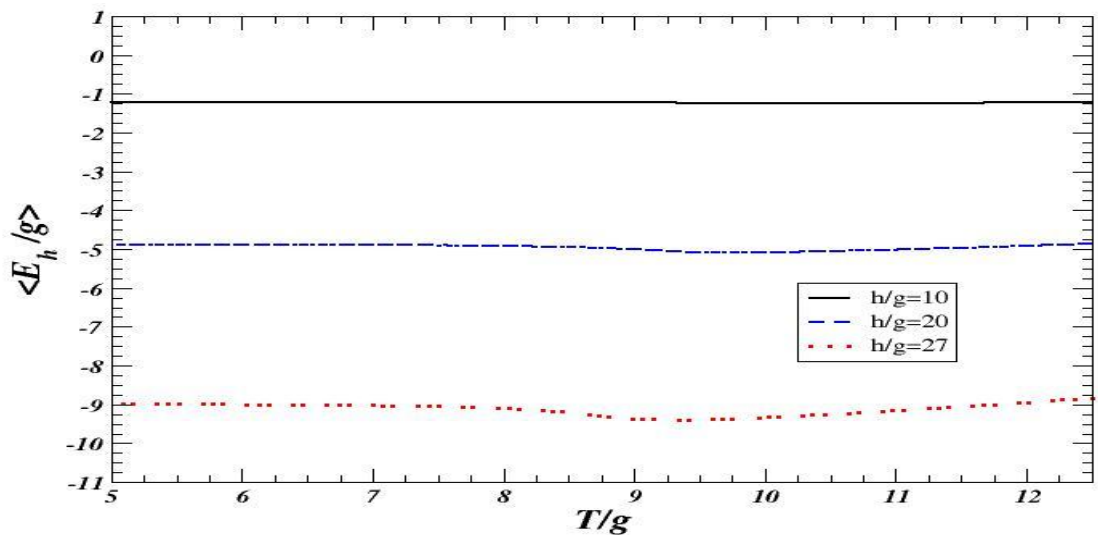


**Figure 4.34:** A plot of the average Zeeman energy  $\langle E_{\text{h}}/g \rangle$  per spin as a function of  $T/g$  at  $k/g = 2$  for  $h/g = 10, 20$  and  $27$ .

In the perpendicular phase, the MC data plotted in Figures 4.31, 4.32, 4.33 and 4.34 conclude that the average dipolar energy and the average Zeeman energy are decreasing as strength of the applied field is increasing; while the average exchange energy and the average anisotropy energy are increasing as strength of the applied field is increasing.

Another evidence for a second order transition between the perpendicular antiferromagnetic order and disordered states is shown in Figures 4.35a, 4.35b and 4.35c, where the heat capacity  $C_H$  per spin is plotted as a function of temperature  $T/g$ , respectively, for  $h/g = 10, 20$  and  $27$  at  $k/g = -10$ . To investigate the effect of applied magnetic field on the heat capacity, Figures 4.35a, 4.35b and 4.35c are plotted in Figure 4.36. The data shown in Figure 4.36 conclude that the location of the transition between the perpendicular antiferromagnetic phase and paramagnetic phase shifts towards the lower temperature as the strength of the applied field is increased. In addition, Figure 4.35 (or Figure 4.36) shows that the system undergoes a second order transition from the perpendicular antiferromagnetic to the paramagnetic phase as the temperature is increased.

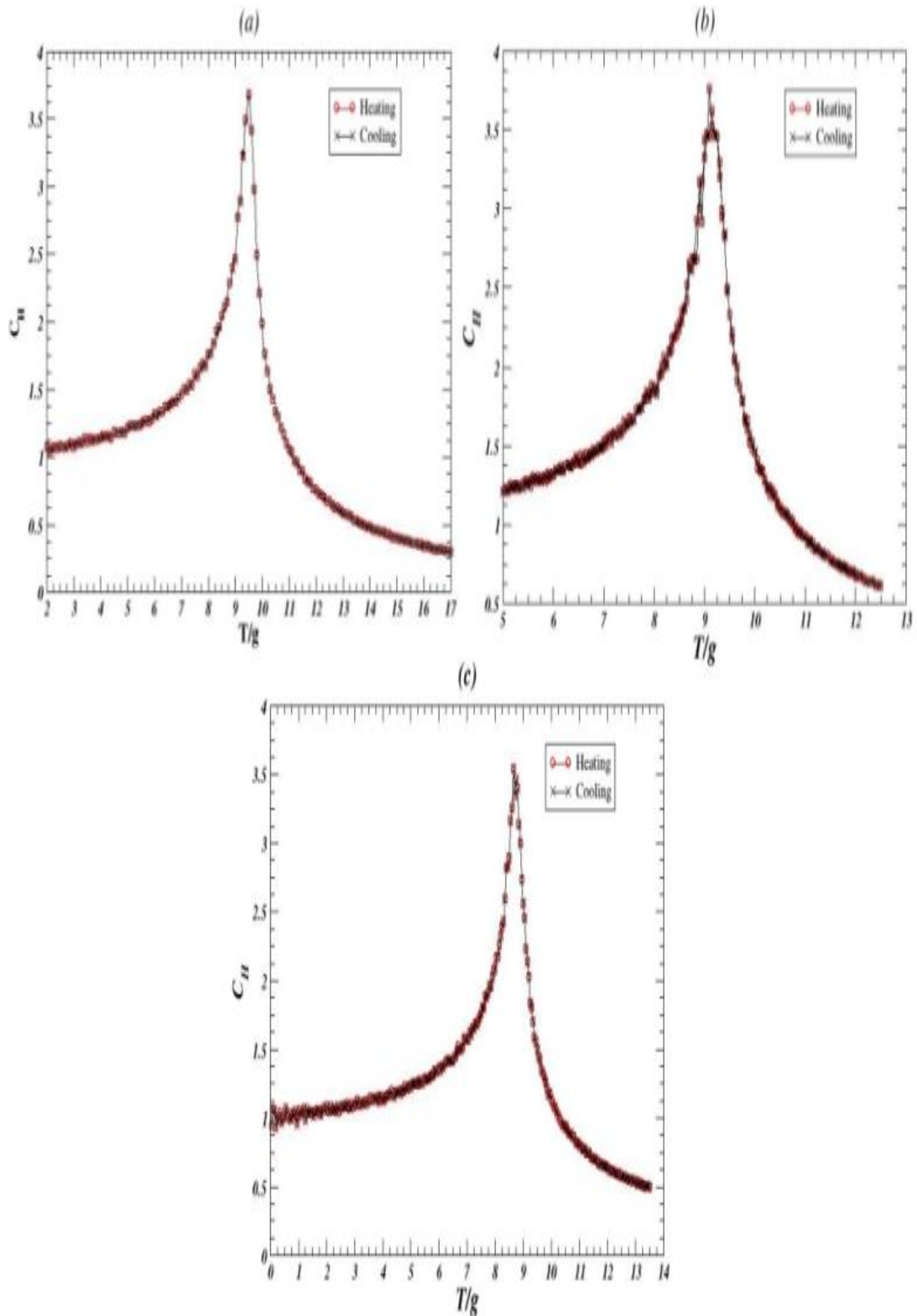


**Figure 4.35:** The specific heat  $C_H$  per spin as a function of heating and cooling the system at  $k/g=2$  for (a)  $h/g= 10$ , (b)  $h/g= 20$  and (c)  $h/g= 27$ .

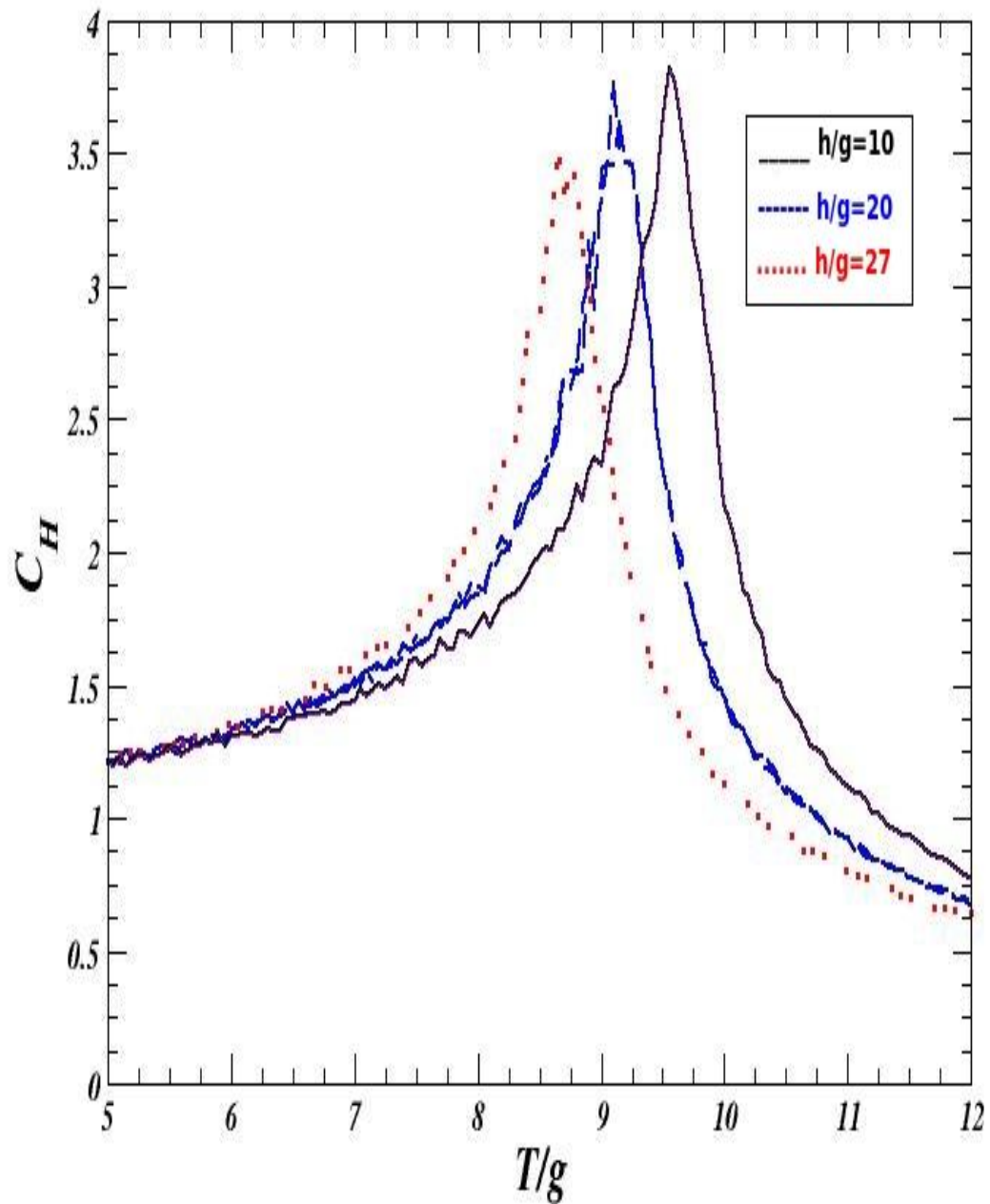


**Figure 4.36:** The specific heat  $C_H$  per spin as a function of  $T/g$  at  $k/g=2$  with  $h/g = 10, 20$  and  $27$ .

### 4.3 The Magnetic Phase Diagram

At finite temperature, the equilibrium phases of the system obtained from Monte Carlo simulations have been presented in the phase diagrams shown in Figures 4.37, 4.38 and 4.39, respectively, for  $h/g = 10, 20$  and  $27$ . The phase diagrams show the planar antiferromagnetic phase (Region I), the perpendicular antiferromagnetic phase (Region II) and a paramagnetic phase (Region III). The simulation points separating the two ordered phases (Region I) and (Region II), and the planar phase (Region I) from the paramagnetic phase (Region III) are obtained from the corresponding peak in the magnetic heat capacity. The transition line (dashed line) between the two ordered phases (Region I and II) appears to be first order as shown in Figures 4.37, 4.38 and 4.39; while the transition line (solid line) between two order phases (Region I and Region II) and the paramagnetic phase (Region III) appears to be second order as shown in Figures 4.37, 4.38 and 4.39. The phase diagrams show that the orientation of the antiferromagnetic state is determined by the relative strength of the magnetic surface anisotropy  $\kappa/g$ , which for ( $k/g \leq -4$ ) the system favours the planar antiferromagnetic state and for ( $k/g \geq -4$ ) it favours the perpendicular antiferromagnetic state with a first order transition between them. For  $\kappa/g < -4$  the MC results show a perpendicular antiferromagnetic order which continuously decreases with increasing temperature until the system undergoes a second order phase transition to the paramagnetic phase at the Néel temperature  $T_N/g$ . A similar behaviour is observed for  $k/g < -4$ , with the difference that the ordered phase is the planar phase.

For an easy comparison between the results of the model with and without a uniform external magnetic fields, the phase diagrams are plotted Figure 4.40.

While Figure 4.40 shows that the sequence of phases observed in the reorientation transition for  $h/g = 10, 20$  and  $27$  cases is similar, two important features are arising because of the effect of the uniform external magnetic field. First is that the reorientation transition line between the two ordered states at very low temperature shifts down with decreasing in slope as  $h$  is increased. The second is that the regions of the perpendicular and planer antiferromagnetic phases are shrink as the applied field is increased.

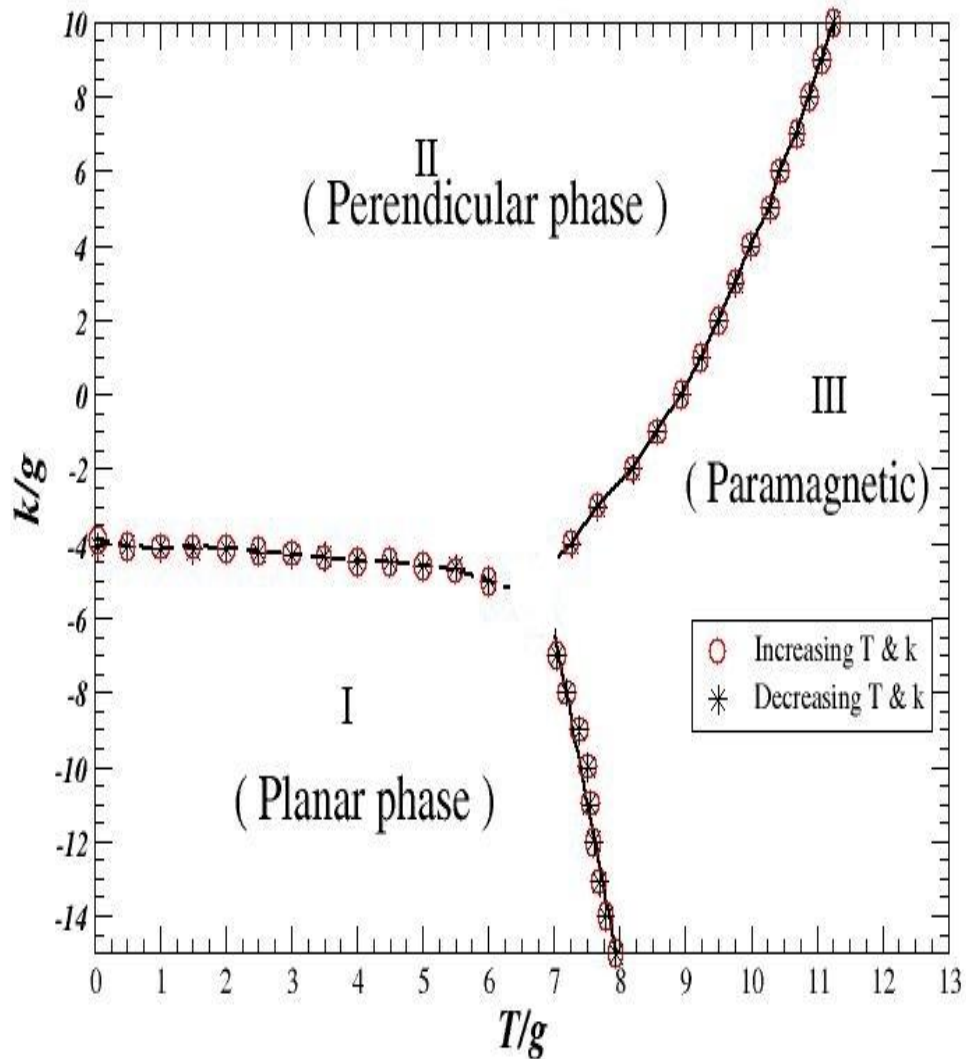


**Figure 4.37:** The magnetic phase diagram as a function of both  $k/g$  and  $T/g$  for  $h/g=10$ . Region I is the planar antiferromagnetic phase, Region II is the perpendicular antiferromagnetic phase, and Region III is the paramagnetic (or disordered) phase. The two solid lines highlight the two lines of second order transition from the two antiferromagnetic order states to the paramagnetic phase. The dashed line highlights the line of first ordered transition between the planar and the perpendicular phases.

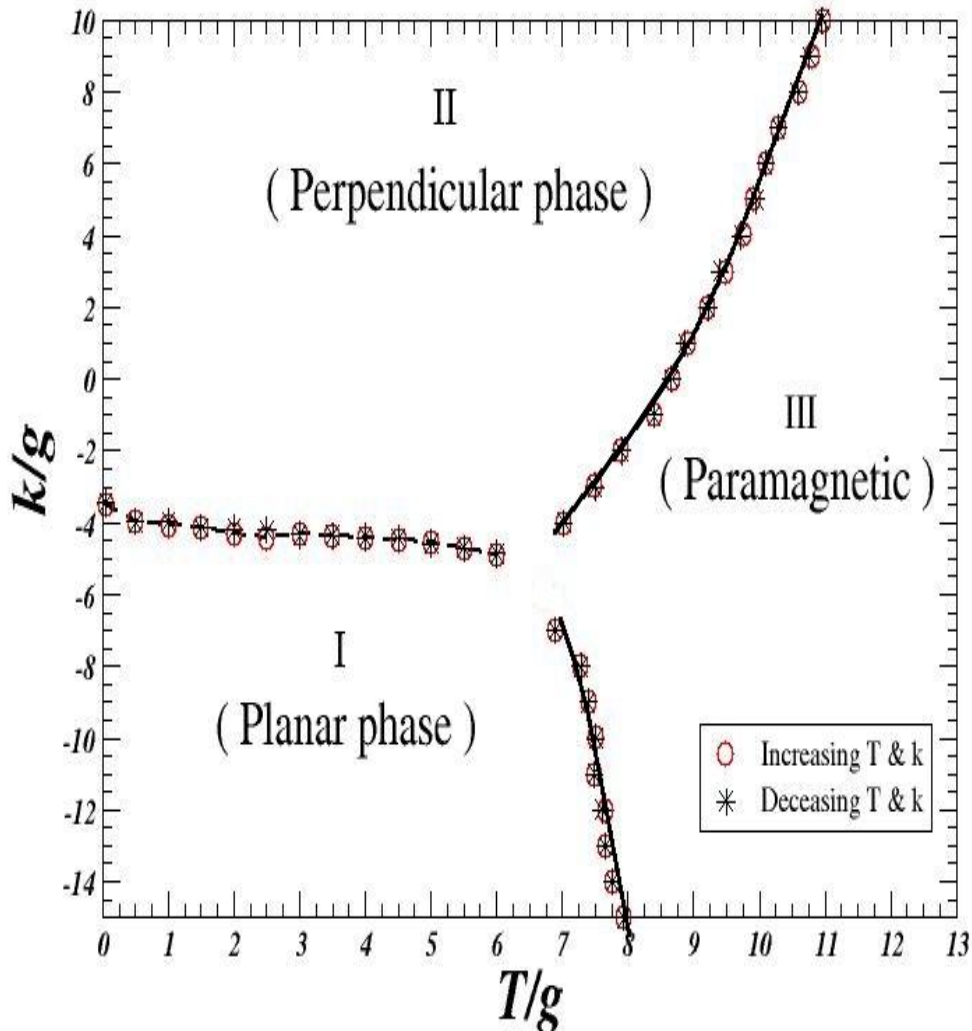


**Figure 4.38:** The magnetic phase diagram as a function of both  $k/g$  and  $T/g$  for  $h/g=20$ . Region I is the planar antiferromagnetic phase, Region II is the perpendicular antiferromagnetic phase, and Region III is the paramagnetic (or disordered) phase. The two solid lines highlight the two lines of second order transition from the two antiferromagnetic order states to the paramagnetic phase. The dashed line highlights the line of first ordered transition between the planar and the perpendicular phases.

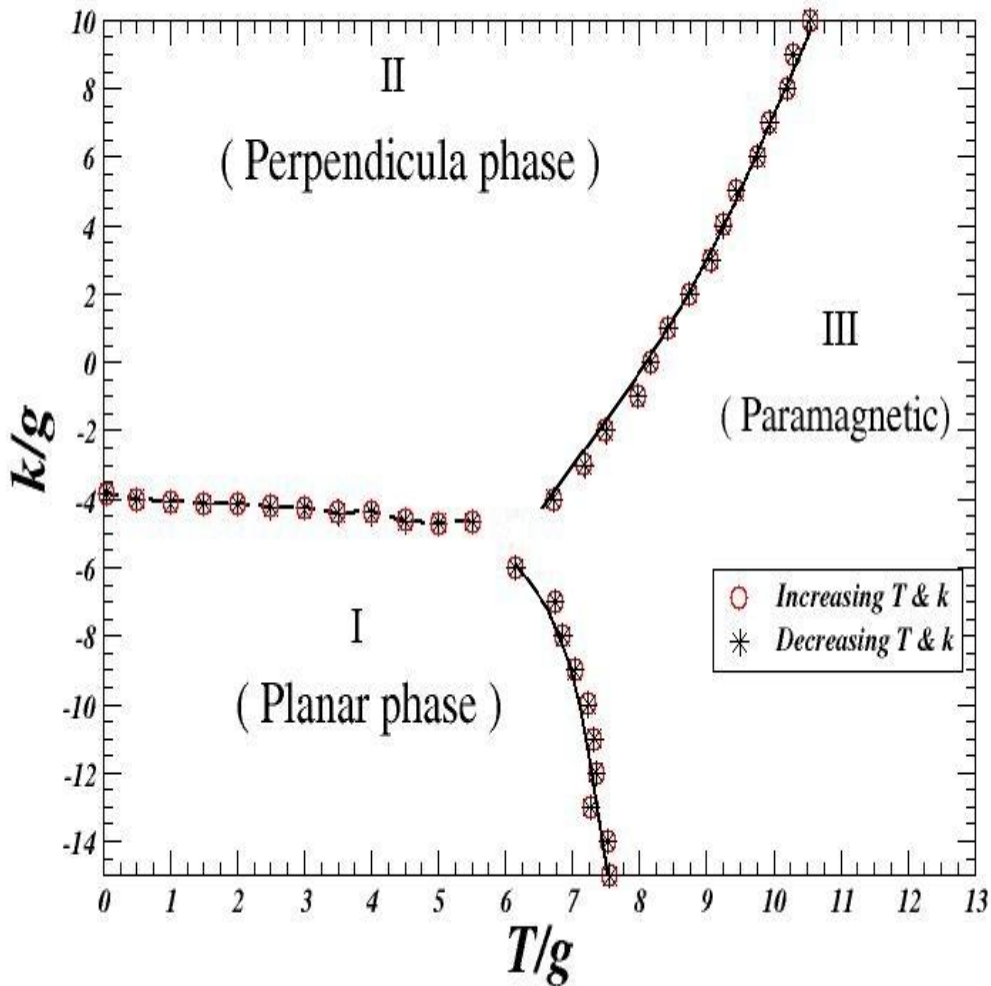


**Figure 4.39:** The magnetic phase diagram as a function of both  $k/g$  and  $T/g$  for  $h/g=27$ . Region I is the planar antiferromagnetic phase, Region II is the perpendicular antiferromagnetic phase, and Region III is the paramagnetic (or disordered) phase. The two solid lines highlight the two lines of second order transition from the two antiferromagnetic order states to the paramagnetic phase. The dashed line highlights the line of first ordered transition between the planar and the perpendicular phases.

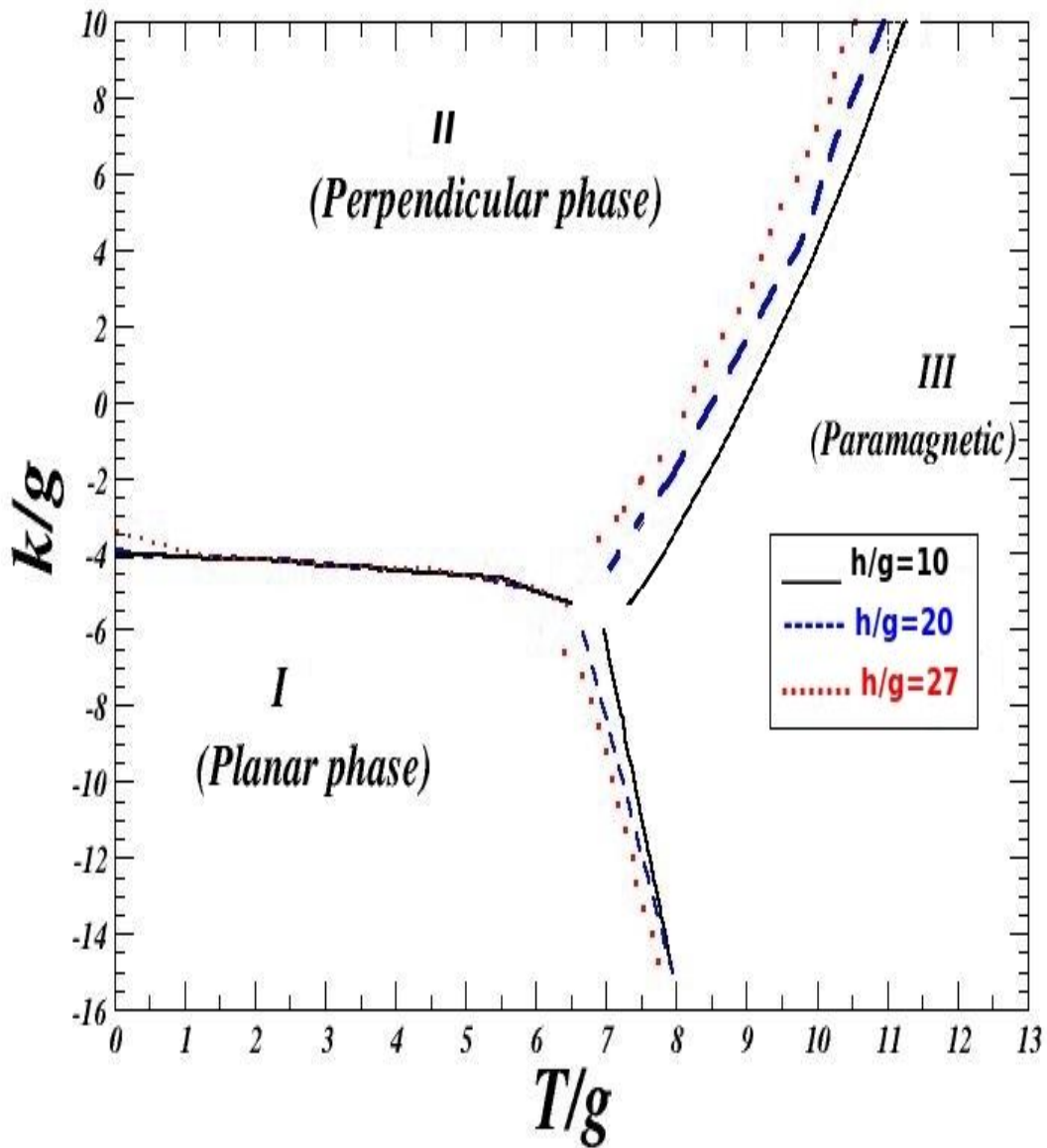


**Figure 4.40:** The magnetic phase diagram as a function of both  $k/g$  and  $T/g$  for  $h/g = 10$ ,  $h/g = 20$  and  $h/g = 27$ . Region I is the planar antiferromagnetic phase, Region II is the perpendicular antiferromagnetic phase, and Region III is the paramagnetic phase.

**Chapter 5**  
**Conclusions**

## Chapter 5

### Conclusions

In this study, effects of a parallel uniform external magnetic field on the magnetic properties of a square dipolar antiferromagnetic Heisenberg system ( $N = 32 \times 32$ ) with heating, cooling, increasing and decreasing of the strength of the relative surface anisotropy  $\kappa/g$  have been studied. In particular, the magnetic phase diagram for this system has been determined as a function of both temperature and magnetic surface anisotropy parameter for different values of the strength of the applied magnetic field ( $h/g = 10, 20$  and  $27$ ) using Monte Carlo simulations. As mentioned in Chapter 1, there are many technological and industrial applications for quasi two-dimensional systems, specially, their applications in data storage devices. Since such systems are very sensitive to the action of an external magnetic field, it is a better to understand the effects of a uniform applied magnetic field on the nature and stability of these systems.

In the current work, the simulations focus on the exchange - dominated regime in which the strength of the antiferromagnetic exchange interaction is greater than the dipolar interaction (i.e.,  $J/g = -10$ ). In addition the uniform external magnetic field is applied parallel to the x-axis of the square lattice, where the in plan directions of the square lattice are denoted by  $\hat{x}$  and  $\hat{y}$ , and the direction perpendicular to the plane is denoted by  $\hat{z}$ .

At low temperature and for large negative values of  $k/g$  (i.e.,  $k/g \leq -4$ ), Monte Carlo simulations show a planar phase, in which the spins are oriented antiferromagnetically parallel to the plane of the system. At low temperature and for large positive values of  $k/g$  (i.e.,  $k/g \geq 4$ ), Monte Carlo results show a perpendicular phase in which the spins are aligned antiferromagnetically perpendicular of the plane of the system. Moreover, the Monte Carlo simulations indicate that the line of the transition between the two ordered phases is a line of first order with very small latent heat.

At large negative values of  $k/g$ , the simulation results show that the system undergoes a second order transition from the planar antiferromagnetic phase to paramagnetic phase as the temperature is increased. At large positive value of  $k/g$ , the results also show that the system undergoes a second order transition but from the perpendicular antiferromagnetic phase to paramagnetic phase as the temperature is increased.

While the sequence of phases observed in the reorientation transition for  $h/g = 10, 20$  and  $27$  cases shows similar behavior, two important features are arising because of the effect of the uniform external magnetic field. First is that the reorientation transition line between the two ordered states at very low temperature shifts towards the negative values of  $k$  with decreasing in slope as  $h$  is increased. The second is that the regions of the perpendicular and planar antiferromagnetic states are shrink as the applied field is increased. These results are summarized in the phase diagrams shown in Figures 4.37, 4.38, 4.39 and 4.40.

## References

## References

- [1] Fowler, M. **Historical Beginnings of Theories of Electricity and Magnetism**. The Great Scientists, Jack Meadows, Oxford, 1994
- [2] David, J. C. **Introduction to magnetism and magnetic materials**, 2nd Edition. 2nd Edition, 1998
- [3] Fleming, J. **Ambrose Magnets and Electric Currents**, 2nd Edition. London: E.& F. N. Spon. pp. 173–174.
- [4] Crangle, J. **The Magnetic Properties of Solids (The Structures and Properties of Solids**, 6nd Edition , 1977
- [5] Kittel, C. **Introduction to Solid State Physics**, Wiley: New York, 1996.
- [6] Neil, W. Ashcroft. and David Mermin, N. **Solid State Physics** Harcourt: Orlando, 1976.
- [7] Jackson, J. D. **Classical Electrodynamics** Wiley: New York, 1999.
- [8] Stanciu, C. D. Kimel, A. V. Hansteen, F. Tsukamoto, A. Itoh, A. Kirilyuk, A. and Rasing, Th. **Ultrafast spin dynamics across compensation points in ferrimagnetic GdFeCo: The role of angular momentum compensation**, Phys. Rev. B 73, 220402(R), (2006).
- [9] Néel, L. **Propriétés magd nétiques des ferrites; Férrimagnétisme antiferromagnétisme**, Annales de Physique (Paris) 3, 137-198, (1948).
- [10] Wolf, S. A., Awschalom, D. D. Buhrman, R. A. Daughton, J. M. Vonolnar, S. Roukes, M. L. Chtchelkanova, A. Y. and Treger, D. M. **Spintronics: A spin-based electronics vision for the future**, Science,294:1488-1495,2001.
- [11] Freeman, M. R. and Choi, B. C. **Advances in magnetic microscopy**, Science, 294: 1484 – 1488, 2001.
- [12] Shen, J. Skomski, R. Klaua, M. Jenniches, H. Manoharan, S. and Kirschner, J. **Magnetism in one dimension: Fe on Cu(111)**, *Physical Review. B* 56, 2340 – 2343, (1997).
- [13] Prutton, M. **Introduction to surface physics**, Clarendon Press, Oxford,1994 .
- [14] Jones, T. L. and Venus, D. **Structural and magnetic characterization of thin iron films on a tungsten (001) substrate**, Surface Science, 302:126 – 140, 1994.

- [15] Borchers, J. A. Erwin, R. W. Berry, S. D. Lind, D. M. Ankner, J. F. Lochner, E. Shaw, K. A. and Hilton, D. **Long-range magnetic order in  $\text{Fe}_3\text{O}_4/\text{NiO}$  super lattices**, Physical Review B, 51(13):8276-8286,1995.
- [16] Tsang, C. Tsann, Lin, R. E. F. Heim, D. E. Speriosu, V. S. Gurney, B. A. and Williams, M. L. **Design, fabrication, and testing of spin-valve read heads for high density recording**, IEEE Transactions on Magnetics, 30(6):3801-3806,1994.
- [17] Spanke, D. Solinus, V. Knabben, D. Hillebrecht, F. U. Ciccacci, F. Gregoratti, L. and Marsi, M. **Evidence for in-plane antiferromagnetic domains in ultrathin NiO films**, Physical Review B, 58(9):5201-5204,1998.
- [18] Baruchel, J. **X-ray and neutron topographical of magnetic materials**, Physica B, 192:79-93,1993.
- [19] Stohr, J. Sholl, A. Luning, J. Scheinfein, M. R. Padmore, H. A. and White, R. L. **Images of the antiferromagnetic structure of a NiO surface by means of X-ray magnetic linear dichroism spectromicroscopy**, Physical Review Letters, 83(9):1862-1865,1999.
- [20] Sholl, A. Stohr, J. Luning, J. Seo, J. W. Fempeyryne, J. Siegwart, H. Locquet, J. P. Nolting, F. Anders, S. Fullerton, E. E. Scheinfein, M. R. and Padmore, H. A. **Observations of antiferromagnetic domains of epitaxial thin films**, Science, 287:1014-1016,2000.
- [21] Schulz, B. and Baberschke, K. **Crossover from in-plane to perpendicular magnetization in ultrathin Ni/Cu(001) films**, Physical Review B, 50 (18):13467-13471,1994.
- [22] Baberschke, K. **The magnetism of nickel monlayers**, Applied Physics A, 62:417-427,1996.
- [23] Farle, M. Platow, W. Anisimov, A. N. Schulz, B. and Baberschke, K. **The temperature dependence of magnetic anisotropy in ultrathin films**, Journal of Magnetizm and Magnetic Materials, 165:74-77, 1997.
- [24] Allenspatch, R. Stampanoni, M. and Bischof, A. **Magnetic domains in thin epitaxial Co/Au(111) films**, Physical Review Letters, 65(26):3344-3347,1990.
- [25] Pappas, D. P. Kamper, K. P. and Hopster, H. **Reversible transition between perpendicular and in-plane magnetization in ultrathin films**, Physical Review Letters, 64 (26): 3179-3182,1990.

- [26] Allenspatch, R. and Bischof, A. **Magnetization direction switching in Fe/Cu(100) epitaxial films: Temperature and thickness dependence**, Physical Review Letters, 69 (23):3385-3388,1992 .
- [27] Qiu, Z. Q. Pearson, J. and Bader, S. D. **Asymmetry of the spin reorientation transition in ultrathin Fe films and wedges grown on Ag(100)**, Physical Review Letters, 70(7):1006-1009,1993.
- [28] Berger, A. and Hopster, H. **Magnetization reversal properties near the reorientation phase transition of ultrathin Fe/Ag(100) films**, Journal of Applied Physics, 79(8):5619-5621,1996 .
- [29] Allenspatch, R. Stampanoni, M. and Bischof, A. **Magnetic domains in thin epitaxial Co/Au(111) films**, Physical Review Letters, 65(26):3344-3347,1990 .
- [30] Speckmann, M. Oepen, H. P. and Ibach, H. **Magnetic domain structure in ultrathin Co/Au(111): On the influence of film morphology**, Physical Review Letters, 75(10):2035-2038,1995.
- [31] Liu, C. and Bader, S. D. **Perpendicular surface magnetic anisotropy in ultrathin epitaxial Fe films**, Journal of Vacuum Science and Technology A, 8 (3):2727-2731, 1990.
- [32] De'Bell, K. and Whitehead, J. P. **The dipole-dipole contribution to the magnetic propagator in the REBa<sub>2</sub>Cu<sub>3</sub>O<sub>7-δ</sub> compounds**, Journal of Physics : Condensed Matter, 3: 2431 - 2439, 1991.
- [33] De'Bell, K. MacIsaac, A. B. and Whitehead, J. P. **Dipolar effects in magnetic thin films and quasi-two dimensional systems**, Review of Modern Physics, 72 : 225, 2000
- [34] Lynn, J. W. **Two-dimensional behavior of the rare earth ordering in oxide superconductors**, Journal of Alloys and Compounds, 181, 1992.
- [35] Lynn, J. W. Li, W. H. Li, Q. Ku, H. C. Yang, H. D. and Shelton, R. N. **Magnetic fluctuations and two-dimensional ordering in ErBa<sub>2</sub>Cu<sub>3</sub>O<sub>7</sub>**, Physical Review B, 36(4):2374-2377,1987.
- [36] Lynn J. W. **High Temperature superconductivity**, Springer-Verlag, NewYork,1990.
- [37] Clinton T. W, and Lynn J. W. **Magnetic ordering of Er in powder and single crystals of ErBa<sub>2</sub>Cu<sub>3</sub>O<sub>7</sub>**, Physica C, 174:487-490,1991.

- [38] Clinton T. W, Lynn J. W, Liu J. Z, Jia Y. X, Goodwin T. J, Shelton R. N, Lee B. W, Buchgeister M, Maple M. B, and Peng J. L. **Effects of oxygen on the magnetic order of the rare-earth ions in  $\text{RBa}_2\text{Cu}_3\text{O}_{6+x}$  ( $\text{R}=\text{Dy},\text{Er},\text{Nd}$ )**, *Physical Review B*, **51**(21):15429-15447,1995.
- [39] Skanthakumar S, and Lynn J. W. **Spin dynamics of  $\text{Er}^{3+}$  ions in  $\text{RBa}_2\text{Cu}_3\text{O}_{7-\delta}$** , *Journal of Applied Physics*, **81**(8):4934-4936,1997.
- [40] Tarascon J. M, McKinnon W. R, Greene L. H, Hull G. W, and Vogel E. M. **Oxygen and rare earth doping of the 90-K superconducting perovskite  $\text{YBa}_2\text{Cu}_3\text{O}_{7-x}$** , *Physical Review B*, **36**(1):226-234,1987.
- [41] Knobel M, Sampaio L. C, Sinnecker E. H. C. P, Vargas P, and Altbir D. **Dipolar magnetic interactions among magnetic microwires**, *Journal of Magnetism and Magnetic Materials*, **249**:60-72, 2002.
- [42] Sampaio L. C, Hyndman R, de Menezes F. S, Jamet J. P, Meyer P, Gierak J, Chappert C, Mathet V, and Ferre J. **Power-law relaxation decay in two dimensional arrays of magnetic dots interacting by long-range dipole-dipole interactions**, *Physical Review B*, **64**(18):4440(1)-4440(7), 2001.
- [43] Cowburn R. P, Adeyeye A. O, and Welland M. E. **Controlling magnetic ordering in coupled nanomagnet arrays**, *New Journal of Physics*, **1**(6):19, 1999.
- [44] Cowburn R. P. **Property variation with shape in magnetic nanoelements**, *Journal of Physics D: Applied Physics*, **33**:R11-R16, 2000.
- [45] Giersig .M, and Hilgendorf M. **The preparation of ordered colloidal magnetic particles by magnetophoretic deposition**, *Journal of Physics D: Applied Physics*, **32**: L111-L113, 1999.
- [46] Hyndman R, Mougén A, Sampaio L. C, Ferre J, Jamet J. P, Meyer P, Mathet V, Chappert C, Mailly D, and Gierak J. **Magnetization reversal in weakly coupled magnetic patterns**, *Journal of Magnetism and Magnetic Materials*, **240**:34-36:1467-1469, 2002.
- [47] Sinnecker E. H. C. P, de Menezes F. S, Sampaio L.C, Knobel M, and Vazquez M. **Tailoring coercivity in an array of glass-coated microwires**, *Journal of Physics D*, **29**: 226-236, 2001.
- [48] Vazquez M, and Hernando A. **A soft magnetic wire for sensor applications**, *Journal of Physics D*, **29**: 939-949, 1996.

- [49] Chiriac H. and Ovari T. A. **Amorphous glass-covered magnetic wires: preparation, properties, applications**, *Physical Review B*, **40**: 333-407, 1996.
- [50] Prinz G. **Magnetoelectronics**, *Science* **282**, 1660, 1998.
- [51] Cowburn R. P. **Property variation with shape in magnetic nanoelements**, *Journal of Physics D: Applied Physics*, **33**:R11-R16, 2000.
- [52] Rapini M, Dias R. A, and Costa B. V. **Phase transition in ultrathin magnetic films with long-range interactions: Monte Carlo simulation of the anisotropic Heisenberg model**, *Physical Review B*, **75**, 014425, 2007.
- [53] Nielsch K, Wehrspohn R. B, Barthel J, Kirschner J, Fischer S. F, Kronmüller H, Schweinböck T, Weiss D, and Gosele U. **Switching behavior of single nanowires inside dense nickel nanowire array**. *Journal of Magnetism and Magnetic Materials*, **291**, 234-240, 2002.
- [54] Sorop T. G, Untiedt C, Luis F, Kroll M, Rasa M, and de Jongh L. J. **Magnetization reversal of ferromagnetic nanowires studied by magnetic force microscopy**. *Physical Review B* **67**, 014402, 2003.
- [55] Asenjo A, Jafaar M, Navas D, and Vázquez M. **Quantitative magnetic force microscopy analysis of the magnetization process in nanowire arrays**. *Journal of Applied Physics*, **100**, 023909, 2006.
- [56] Sampaio L. C, Sinnecker E. H. C. P, Cernicchiaro G. R. C, Knobel M, Vázquez M, and Velázquez J. **Magnetic microwires as macrospins in a long range dipole-dipole interaction**, *Physical Review B*, **61**(13),8976-8983, 2000.
- [57] Jensen P. J and Bennemann K. H. **Magnetic structure of films: Dependence on anisotropy and atomic morphology**, *Surface Science Reports*, **61**:129, 2007.
- [58] Merzln N D and Wagner H. **Absence of ferromagnetism or antiferro-magnetism in one- or two-dimensional isotropic Heisenberg models**, *Physical Review Letters*, **17**:1133-6, 1966.
- [59] Bloch F. **Zur theorie des ferromagnetismus**, *Zeitschrift für Physik*, **49**: 206-219, 1928.
- [60] Pescia D and Pokrovsky V. L. **Perpendicular versus in-plane magnetization in a 2D Heisenberg monolayer at finite temperatures**. *Physical Review Letters*, **65**(20):2599-2601, 1990.

- [61] Politi P, Rettori A, and Pini M. G. Comment on "**perpendicular versus in-plane magnetization in a 2D Heisenberg monolayer at finite temperatures**". *Physical Review Letters*, 70(8) :1184-1184, 1993.
- [62] Levanyuk A.P and Garcia N. **Comment on "perpendicular versus in-plane magnetization in a 2D Heisenberg monolayer at finite temperatures"**. *Physical Review Letters* 70(8):1184- 1184, 1993.
- [63] Ried K, Millev F, Fahnle Y, and Kronmüller. **Phase transitions in ferromagnets with dipolar interactions and uniaxial anisotropy**. *Physical Review B*, 51(21):15229-15849, 1995.
- [64] Moschel A and Usadel K. D. **Influence of the dipolar interaction on the direction of the magnetization in thin ferromagnetic films**. *Physical Review B*, 49(18):12868-12871, 1994.
- [65] Moschel A and Usadel K. D. **Reorientation transitions of first and second order in thin ferromagnetic films**. *Physical Review B*, 51(22):16111-16114, 1995.
- [66] Moschel A and Usadel K. D. **Influence of the film thickness on the direction of the magnetization in thin ferromagnetic films**. *Journal of Magnetism and magnetic Materials*, 140-144:649-650, 1995.
- [67] Usadel K. D. and Hucht A. **Anisotropy of ultrathin ferromagnetic films and the spin reorientation transitions**. *Physical Review B*, 66(2):024419(1)-024419(6), 2002.
- [68] Chui S. T. **Phase boundaries in ultrathin magnetic film**, *Physical Review B*, 50(17):12559-12567, 1994.
- [69] Hucht A. Moschel A. and Usadel K. D. **Monte-Carlo study of the reorientation transitions in Heisenberg models with dipole interactions**. *Journal of Magnetism and Magnetic Materials*, 148:32:1995.
- [70] Ying L. Nanxian C. Hongmin Z. and Chengwen W. **Carlo simulation of the reorientation transitions in Heisenberg models with dipolar interactions**. *Solid state Communications*, 126:223-227, 2003.
- [71] Hucht A. and Usadel K. D. **Characterization of the**

- reorientation transitions in classical Heisenberg models with dipole interactions.** *Journal of Magnetism and Magnetic Materials*, 156:423-424,1996.
- [72] Vedmedenko E. Y, Oepen H. P and Kirschner J. **Microstructure of the spin reorientation transitions in second-order approximation of magnetic anisotropy**, *Physical Review B*, 66(21):214401(1)-214401(5),2002.
- [73] Bruno P. **Spin-wave theory of two-dimensional ferromagnets in the presence of dipolar interactions and magnetocrystalline anisotropy.** *Physical Review*, 43(7) :6015-6031, 1991.
- [74] Bland J. A. C, Daboo C, Gehring G. A, Kaplan B, Ives A. J. R, Hicken R. J, and Johuson A. D. **Magnetization of ultrathin ferromagnetic films at finite temperatures.** *Journal of Physics: Condensed Matter*, 7:6367-6476,1995.
- [75] Yafet Y. Kwo J. and Gyorgy E. M. **Dipole-dipole interactions and two-dimensional magnetism.** *Physical Review B*, 33(9):6519-6522, 1986.
- [76] Stamps R. L. and Hillebrands B. **Dipolar interactions and magnetic behavior of two-dimensional ferromagnetic systems.** *Physical Review B*, 44(22):12417-12423 , 1991.
- [77] Abu-Labdeh A. M. **Monte Carlo Simulations for Classical Two-dimensional Dipolar Antiferromagnetic Systems on a Square Lattice.** *PhD thesis*, Memorial University, 2004.
- [78] Abu-Labdeh A. M. Chafe N. P. Whitehead J. P. De'Bell K. and MacIsaac A. B. **Phase behaviour of the antiferromagnetic plane rotator model**, *Journal of Physics: Condensed Matter*, 14:7155-7163, 2002.
- [79] Abu-Labdeh A. M. and MacIsaac A. B. **Effects of a uniform external magnetic field on the magnetic properties of a pure dipolar planar system**, *Physical Review B*, 73, 094412-094420, 2006.
- [80] Abu-Labdeh A. M. Whitehead J. P. De'Bell K. and MacIsaac A. B. **Phase behavior of antiferromagnetic ultrathin magnetic films.** *Physical Review B* , 65, 024434, (2001).
- [81] Abu-Labdeh A. M. Whitehead J. P. De'Bell K. and MacIsaac A. B. **Effects of a weak magnetic surface anisotropy on the magnetic**

**phase diagram of the dipolar antiferromagnetic Heisenberg system**

Physical Review B, 70, 144416, 2004.

- [82] Abu-Labdeh A. M. MacIsaac A. B. Whitehead J. P. and De'Bell K. **Evidence for a reorientation transition in the phase behaviour of a two-dimensional dipolar antiferromagnet**, *Journal of Physics: Condensed Matter* 16:941–954, 2004.
- [83] Abu-Labdeh A. M. MacIsaac A. B. Whitehead J. P. and De'Bell K. **Effect of a Uniform Perpendicular External Magnetic Field on the Dipolar Heisenberg Model with Dominant Exchange Interaction.** (Unpublished )
- [84] Weber W. Back C. h. Bischof A. Pescia D. and Allenspach R. **Magnetic switching in cobalt films by adsorption of copper**, *Nature* (London), 374,788-790, 1995.
- [85] MacIsaac A. B. **Monte Carlo study of the two-dimensional dipolar Ising model.** *Master's thesis*, Memorial University, 1992.
- [86] MacIsaac A. B. **The magnetic properties of a model two-dimensional dipolar thin film.** *PhD thesis*, Memorial University, 1997.
- [87] Bernd A. Berg. **Markov Chain Monte Carlo Simulations and Their Statistical**, *World Scientific 2004*, ISBN 981-238-935-0
- [88] R J. and Ulam S. **The Monte Carlo method**, *Journal of the American Statistical Association*, **44** 335, 1949
- [89] Metropolis N. **The beginning of the Monte Carlo method**, *Los Alamos Science (1987 Special Issue dedicated to Stanislaw Ulam)*: 125–130.
- [90] Landau D. P. and Binder K. A. **Guide to Monte Carlo Simulations in Statistical Physics**, *Cambridge University Press*, 2000.
- [91] Metropolis N. and Ulam S. **The Monte Carlo method**, *Journal of the American Statistical Association*, **44** 335, 1949.
- [92] Novotny M. A. **Monte Carlo with absorbing Markov chains: fast local algorithm for slow dynamics**, *Physical Review Letters*. **74** 1 (1995);Erratum, 75 1424 (1995);eprint: arXiv: cond-mat/9411081,1994.
- [93] Bortz A. B. Kalos M. H. and Lebowitz J. L. **A new algorithm for Monte Carlo simulation of Ising spin systems**, *Journal of*

*Computational Physics*, 1710, 1975.

- [94] Berg B. A. and Neuhaus T. **Multicanonical ensemble: a new approach to simulation of first order phase transition**, *Physical Review Letters*, 68 9, 1992.
- [95] Mac Gillivray H. T. Dodd R. J. **Monte Carlo simulations of galaxy systems**, *Astrophysics and Space Science*, Volume 86, Number 2 / September, 1982, Springer Netherlands.
- [96] Metropolis N. Rosenbluth A. W. Rosenbluth M. N. Teller A. H. and Teller E. **Equation of state calculation by fast computing machine**, *Journal of Chemical Physics*. 21 1087, 1953
- [97] De'Bell K, MacIsaac A. B, and Whitehead J. P. **Dipolar effects in magnetic thin films and quasi-two dimensional systems**, *Review of Modern Physics*, **72** : 225, 2000.
- [98] Metropolis N. Rosenbluth A. W. Rosenbluth M. N. Teller A. H. and Teller E. **Equation of state calculation by fast computing machine**, *Journal of Chemical Physics*. 21 1087, 1953.
- [99] Abu-Labdeh A. M. Chafe N. P. Whitehead J. P. De'Bell K. and MacIsaac A B. **Phase behaviour of the antiferromagnetic plane rotator Model** , *Journal of Physics: Condensed Matter*, 147155-7163, 2002.
- [100] De'Bell K. MacIsaac A. B. and Whitehead J. P. **Dipolar effects in magnetic thin films and quasi-two dimensional systems**, *Review of Modern Physics*, 72 : 225, 2000

جامعة النجاح الوطنية

كلية الدراسات العليا

تأثيرات المجال المغناطيسي الخارجي المنتظم على الخواص المغناطيسية  
لنظام هايزنبرغ ثنائي قطبي فيرومغناطيسي مضاد

إعداد

ثائر "محمد سعيد" مصطفى أبو لبده

إشراف

د. عبد الرحمن مصطفى أبو لبده

قدمت هذه الأطروحة استكمالاً لمتطلبات درجة الماجستير في الفيزياء بكلية الدراسات العليا في  
جامعة النجاح الوطنية في نابلس - فلسطين.

2009

## تأثيرات المجال المغناطيسي الخارجي المنتظم على الخواص المغناطيسية لنظام هايزنبرغ ثنا قطبي فيرومغناطيسي مضاد

إعداد

ثائر "محمد سعيد" مصطفى أبو لبده

إشراف

د. عبد الرحمن مصطفى ابو لبدة

### الملخص

في هذا البحث تمت دراسة التأثيرات الناشئة عن مجال مغناطيسي خارجي منتظم على الخواص المغناطيسية لشبكية مربعة لنظام هايزنبرغ ثنا قطبي فيرومغناطيسي مضاد ببعده  $(32 \times 32)$ ، على درجات حرارة مختلفة باستخدام طريقة مونت كارلو. افترضت هذه الدراسة ان العزوم المغناطيسية عبارة عن عزوم كلاسيكية وتتفاعل فيما بينها من خلال تأثيرات التبادلية من نوع الفيرومغناطيسية المضادة مع الايونات المجاورة القريبة وكذلك التأثيرات الثنا قطبية ذات المدى الطويل إضافة إلى المجال المغناطيسي الخارجي المنتظم الذي يؤثر باتجاه المحور السيني للشبكية. أثناء الدراسة تم تثبيت مقدار عامل التأثيرات التبادلية  $J/g$  (نوع الفيرومغناطيسية المضادة) بين الايونات المتفاعلة على القيمة  $-10.0$  (حيث تمثل  $g$  مقدار عامل التأثيرات الثنا قطبية).

من خلال عمليات محاكاة النظام باستخدام طريقة مونت كارلو تم تحديد "شكل الطور" كعلاقة بين تباين الخواص المغناطيسية السطح  $k/g$  ودرجة الحرارة  $T/g$ ، بيّنت نتائج المحاكاة على درجة حرارة منخفضة و عند قيم  $k/g \geq -4$  أن النظام يفضل أن يكون من طور الفيرومغناطيسية المضاد المستوي حيث تترتب العزوم المغناطيسية الكلاسيكية بشكل موازي لشبكية النظام. و  $k/g \leq -4$  أظهرت نتائج المحاكاة أن النظام يفضل أن يكون من طور الفيرومغناطيسية المضاد العمودي. كذلك أظهرت نتائج المحاكاة ان النظام يظهر انتقالاً من الدرجة الاولى من طور الفيرومغناطيسية المضاد المستوي الى طور الفيرومغناطيسية المضادة العمودي كلما زادت قيمة  $k/g$ ، و عند درجات حرارة منخفضة جدا و مع ازدياد قيمة المجال المغناطيسي الخارجي المؤثر على النظام أظهرت الدراسة نقصان في قيمة ميل خط الانتقال

ت

الفاصل بين طور الفيرومغناطيسية المضادة المستوي وطور الفيرومغناطيسية المضادة العمودي، بينما عند قيم مختلفة ل  $K/g$  ، أظهرت نتائج مونت كارلو ان النظام يظهر انتقالاً من الدرجة الثانية ) من طور الفيرومغناطيسية المضادة إلى طور البارامغناطيسية عند ازدياد درجات الحرارة .بالإضافة إلى ذلك بينت نتائج الدراسة حدوث انكماش في طور الفيرومغناطيسية المضاد (المستوي و العمودي) مع زيادة قيمة المجال المغناطيسي الخارجي المؤثر على النظام.